Modeling biodegradable stents and their effect on the arterial wall

Johanne Mensah-Gourmel

NNT : 2016SACLX034

THESE DE DOCTORAT

DE

L'UNIVERSITE PARIS-SACLAY

PREPAREE A

L'ECOLE POLYTECHNIQUE

ECOLE DOCTORALE N°573

Interfaces - Approches interdisciplinaires : Fondements, Application et innovation

Spécialité de doctorat : Physique

Par

Mme Johanne Mensah-Gourmel

Modeling Biodegradable Stents and their Effect on the Arterial Wall

Thèse présentée et soutenue à Palaiseau, le 29 septembre 2016

Composition du Jury :

M. Giuseppe Pontrelli	Senior Researcher au National Center for Research (Rome)	Rapporteur
M. Gérard Finet	Chef de service en cardiologie à l'hôpital Louis Pradel (Lyon)	Rapporteur
M. Bertrand David	Chargé de recherche au MSSMat à l'Ecole Centrale de Paris	Président du jury
M. Machiel van der Leest	CEO d'Arterial Remodeling Technologies	Examinateur
M. Abdul I. Barakat	Professeur à l'Ecole Polytechnique	Co-directeur de thèse
M. Antoine Lafont	Cardiologue interventionnel à l'Hôpital Européen Georges Pompidou	Co-directeur de thèse

Johanne Mensah-Gourmel

Advisors:
Abdul I. Barakat
Antoine Lafont

Modeling Biodegradable Stents and their Effect on the Arterial Wall

Laboratoire d'Hydrodynamique (LadHyX)
École Polytechnique, France

Contents

Acknowledgments

I feel very lucky and happy to have the opportunity to bring a little contribution to the field of research – a little drop in the ocean, but the ocean itself needs all the drops to exist, isn't it? This would not have been possible without the help, the support and the discussions with several persons, and I am pleased to have here the opportunity to thank them.

First of all, I would like to thank my co-advisor, Abdul Barakat. Thank you for giving me this opportunity, to dare involve yourself in such a project, and to trust me to work as hard as I could to make it happens in parallel with medical school. One could not have dreamt of a better advisor: always available to discuss a scientific point but also to support me during rough periods with my dearest friend Comsol and never forgetting to tease me. Thank you for your precious help to build this work and for your smiling presence during the past years.

Many thanks also to my co-advisor Antoine Lafont; it was a great opportunity for me to work at the interface between fundamental research and medicine. This collaboration added an invaluable contribution to this work. Thank you very much for this great work at the Hôpital Européen Georges Pompidou and for always finding a moment to discuss and help me – even between two emergency surgeries.

It was also very rewarding to work in collaboration with a startup; many thanks to Machiel van der Leest for giving me this opportunity.

Thank you Pauline for your patience and your tenacity to build the automated method presented here.

Research is a demanding job, but working with amazing people and sharing everyday moments with them is a great help. I feel very thankful to have been part of such a nice team. Thank you! A very special thanks to Lionel and François for your precious help, your friendship and shared chocolate – I owe you a lot (and so does my computational model! Thank you very much François!).

Many thanks to Mohammed for its help for the experiments, and to Dany and Toai for their priceless help in managing software and computers.

I am very honored that Gerard Finet and Guiseppe Pontrelli accepted to review this work and thank them very much.

Many thanks to Bertrand David and Machiel van deer Leest for having accepted to be part of my thesis committee.

Last but not least, I would like to thank people outside the lab for their friendship and loving support during my PhD; my family, my family in law, my friends and of course; my wonderful Vincent: thank you *binôme* !

List of Figures

List of Tables

Nomenclature

a	constant chosen so that W_i varies between 0.5 and 1
A_1	constant, weight of the contribution of the absence of EC to the arterial remodeling
A_2	constant, weight of the contribution of inflammation to the arterial remodeling
A_3	constant, weight of the contribution of the stresses to the arterial remodeling
$A_v(r)$	function giving the average value of the radius of the stent at a given fixed strut
b	constant chosen so that W_i varies between 0.5 and 1
$[COOH]$	concentration of carboxylic end groups
d	damage parameter
d_b	dogboning
d_C	distance of an object to the catheter
$d_{cat}(P)$	distance of a pixel *P* to the catheter
d_{rough}	estimation of the tube thickness
d_{thick}	threshold value for the difference between the tube thickness measured at two close points
E_{C-O}	energy of a mole of oxygen carbon bonds
$E(\gamma)$	energy associated with the potential W_i
$[ester]$	concentration of ester groups
e_{strut}	estimated thickness of the struts
$E(t)$	number of regenerated EC
E_{tot}	energy one would need to bring to a polymer to break all the covalent bonds
$\boldsymbol{F}$	deformation gradient
f_S	foreshortening
$f(t)$	inflammation score
G	Gaussian kernel

GSI_0	theoretical GSI value that would be measured at a distance infinitely close to the catheter
$GSI_{corrected}$	corrected GSI
$GSI_{measured}$	measured GSI
$[H_2O]$	concentration of water
I	intensity of a given pixel
I_1	first invariant of the right Cauchy-Green deformation tensor
$\tilde{I}(P)$	corrected intensity of a given pixel *P*
I_{back1}	a threshold value that I_{max} should not exceed
I_{back2}	threshold value for the intensity along M'C used to differentiate a point belonging to a strut from a point not belonging to a strut
I_{color}	constant intensity value used to increase the brightness of the struts
I_{max}	maximum value of *I* calculated along M'C
I_{ROF}	threshold intensity value used to binarize the image
I_{shadow}	threshold intensity value used to detect points of the outer contour situated in the catheter shadow
J	determinant of the deformation gradient $\boldsymbol{F}$
J_0	minimum value of $J(t)$ reached at time t_0
J_m	plateau value of $J(t)$
$J(t)$	least square fit for the measured GSI
K	constant in the Poiseuille profile
k'	kinetic constant
k_d	rate of death of EC for an healthy endothelium
$k_{div}(E)$	rate of division of EC during wound healing
k_i	rate of division of EC for an healthy endothelium
k_h	hydrolysis kinetic constant, referring to ART stent
k_h'	hydrolysis kinetic constant, referring to Abbott BVS stent
$k_l(load)$	function modeling the contribution of the load to PLA degradation
k_l^{max}	plateau value at which the $k_l(load)$ function saturates
L_0	initial length of the stent
L_{dep}	final length of the stent
L_e	flow entrance length
L_{max}	load threshold at which the $k_l(load)$ function saturates
$L_S(t, X, Y, Z)$	computed von Mises stresses at each point of the stent
$L_{wall}(t)$	computed von Mises stresses averaged at the inside wall of the artery
m_{LactAc}	mass of a monomer of lactic acid
M_{LactAc}	molar mass of lactic acid
M_n	number average molecular weight
$M_{n,0}$	initial number average molecular weight
m_{stent}	mass of a stent
N_A	Avogadro constant
N_{EC}	number of EC killed by stent deployment
N_{init}	initial number of EC participating to the regeneration of EC for wound healing
N_l	number of covalent bonds

p	pressure applied on the stent during deployment
P	pressure in a fluid
p_{stent}	pressure applied on the stent during deployment and degradation
P_{int}	average blood pressure
Q	flow field
Q_0	volumetric flow rate calculated for a standard coronary artery
R	radius
$r_{balloon}(t)$	function describing the evolution of the radius of the inflating balloon during stent deployment
$r_{central}$	stent radius at the centre
r_{distal}	stent radius at the extremities
R_e	Reynolds number
r_{init}	initial radius of the balloon
r_{max}	maximal radius of the balloon
t_0	time at which the minimum of $J(t)$ is reached
$T_{derivative}$	threshold value regarding the derivative of the intensity along a stroke, used to prevent the program from coloring the struts in black
t_{res}	time at which the applied pressure p reaches 0
v_R	velocity imposed at the inlet boundary
$v_z(r)$	fluid velocity in the axial direction *z*
W	strain energy density function
W_i	potential associated with a given image
$w(t)$	thickness of the arterial wall
W_{VM}	work of the von Mises stresses
$Ø_{lumen}$	diameter of the arterial lumen
ΔH	enthalpy of polymerization
γ_0	initial guess for the sought shape
$\gamma(t)$	parameterized curve
κ	bulk modulus
$\lambda_1, \lambda_2, \lambda_3$	principal stretches
μ	shear modulus
μ_0	initial shear modulus
μ_a	shear modulus of the artery
μ_d	dynamic viscosity
$\Pi_{[I_{min},I_{max}]}$	projection of I onto $[I_{min}, I_{max}]$
ρ_a	density of the artery
ρ_{PLA}	density of the PLA
σ_0	homeostatic value for hoop stress
σ_f	fracture strength
$\sigma_{f,0}$	initial fracture strength
$\sigma(t)$	hoop stress
τ_w	shear stress at the arterial wall

Abbreviations

ART	Arterial Remodeling Technologies
BMS	bare metal stent
BRS	bioresorbable stent
BVS	Bioabsorbable Vascular Scaffold
CE	compliant with European regulation
EC	endothelial cell
EEL	external elastic lamina
DES	drug-eluting stent
FEM	finite element method
IEL	internal elastic lamina
IFU	instructions for use
IVUS	intra vascular ultrasound
LDL	low-density lipoprotein
NO	nitric oxide
OCT	optical coherence tomography
oxLDL	oxidized molecules of LDL cholesterol
PBS	Pure Bioresorbable Scaffold
PDLLA	poly-D,L-lactic acid
PGA	polyglycolic acid
PCL	polycaprolactone
PLA	polylactic acid
PLLA	poly-L-lactic acid
QCA	quantitative coronary angiography
ROI	region of interest
SMC	smooth muscle cells

CHAPTER 1

Introduction

1.1 Atherosclerosis: generalities

The major pathological complications of atherosclerosis, namely coronary heart disease and strokes, are the leading cause of mortality in the world (World Health Organization[1]). Atherosclerosis is characterized by the focal accumulation of lipids, fibrosis, calcifications and cells within the innermost layer of the arterial wall, leading to the formation of plaques that protrude into the vessel lumen and perturb blood flow[2,3]. The prevalence of atherosclerosis has increased in the past decades due to the aging populations of many Western countries. Its incidence has also risen due to lifestyle changes including a reduction in physical activity and the increased consumption of diets rich in sugar, fat and sodium. Although the absolute number of deaths has increased continuously since 1990, the age-standardized cardiovascular mortality rates per 100,000 habitants decreased between 1990 and 2010[4]; this reduction is believed to be due to prevention and improved medical care.

The epidemiology of atherosclerosis varies geographically. For instance, the disability-adjusted life years, which is considered as a measure of the overall disease burden and is the sum of the years lost due to early death and to disability for people living with the health condition[5], is highest in Eastern Europe, central Asia and Russia; somewhat lower in Africa, Indonesia and central Europe; even lower in the USA, central and Southern America; and lowest in Western and South Europe, Canada, Australia, Japan and China[6]. These differences may be due to environmental rather than genetic factors[7]. Non-modifiable systemic risk factors for the disease include age, sex and familial history of cardiovascular diseases, while modifiable risk factors include dyslipidemia, arterial hypertension, high body mass indexes or obesity, diabetes mellitus or elevated glucose levels, smoking and physical inactivity[8].

Atherosclerosis is a chronic inflammatory disease of medium and large arteries. The clinical consequences will vary according to the specific location of the plaque[7,9]. Atheromatous plaques located in the carotid arteries are associated with ischemic strokes, whereas plaques in the coronary arteries are associated with angina and myocardial infarcts; these two localizations are the most frequent and account for a high number of deaths. Plaques can be

encountered in various other locations such as the arteries of the lower limbs where they are associated with arteriopathy of lower limbs; in renal arteries leading to chronic kidney disease; and in the aorta where they are associated with aneurysms.

Atherosclerosis provokes chronic complications[7]. Indeed, the presence of advanced plaque in an artery narrows the vessel, reduces blood flow and can therefore induce shortage of oxygen supplies and thus chronic ischemia of the irrigated organ. This can induce chronic pain such as angina. On the other hand, acute events may also occur[7]. Disruption of the plaque can occur and leads to contact between the intra-plaque material and blood which coagulates upon contact with a foreign material; the thrombus or blood clot thus formed obstructs the vessel and can induce dramatic consequences such as strokes and infarcts. Young soft lipid plaques are more prone to rupture[10] than old fibrosed calcified plaques, but they are more difficult to detect and treat; they are thus sometimes associated with sudden unexpected death. Secondly, intra plaque hematoma sometimes occur which can lead to the rapid expansion of the volume of the plaque and even the blockage of the vessel. In both cases, if the organs subjected to acute complete ischemia are not rapidly re-irrigated, necrosis or death of the cells occurs in a few hours.

1.2 Atherosclerosis: physiopathology

Arteries consist of three layers[3,11]. The innermost layer, the intima, contains a monolayer of endothelial cells (ECs) and the basement membrane on which these cells grow. The intima has multiple functions[12] including: control of the proliferation of smooth muscle cells; the regulation of thrombosis (quiescent ECs are non-thrombogenic and prevent the blood from coagulating whereas activated ECs express adhesion molecules promoting leukocyte adhesion and induce thrombus formation); and the regulation of vessel vasomotion. The second arterial layer is the media, made of smooth muscle cells (SMCs) and fibers of elastin and collagen. The media is primarily responsible for the mechanical properties of the artery and for its ability to immediately adapt to changes in blood pressure and blood flow by undergoing vasodilatation and vasoconstriction. The external layer in an artery is the adventitia, which consists of loose connective tissue and anchors the vessel to surrounding structures. In muscular arteries such as coronary arteries, the media is separated from the endothelium and from the adventitia by the internal elastic lamina (IEL) and the external elastic lamina (EEL), respectively.

High levels of cholesterol – and more especially of low-density lipoprotein (LDL) cholesterol – in the blood lead to the accumulation of lipids between the intima and the media. This phenomenon can be promoted if the endothelium is subjected to various inflammatory factors such as smoking or diabetes. The permeability of the endothelial layer is thus increased which facilitates the entry of lipid molecules, and on the other hand, the inflamed ECs express adhesion molecules which promote the attachment of inflammatory cells from the bloodstream[13]. If not cleared, LDL cholesterol molecules may become oxidized (oxLDL). Thereafter, oxLDL can induce dysfunction of the ECs and the over-expression of chemoattractive molecules for inflammatory cells and more especially monocytes. The

monocytes then pass through the intima, and in the vessel they differentiate into macrophages and may ultimately turn into so called foam cells by engulfing the accumulated lipids. Thus, a lipid core is formed in the arterial wall. Yurdagul *et al.*[14] demonstrated that the macrophages produce various types of inflammatory molecules called cytokines. Some cytokines produced by inflammatory macrophages favor the development of atherosclerosis by promoting foam cell formation and cellular apoptosis. Other cytokines produced by wound healing macrophages counter-act the atherogenic effect by decreasing inflammation and leukocyte recruitment. The balance between pro- and anti-atherosclerotic cytokines is likely to have a great impact on the rate at which plaques progress.

Inflammation also induces the transformation of SMCs from a quiescent, contractile state to a migratory and proliferative state. Thus, SMCs migrate from the media into the intima and form around the lipid core a so called fibrous cap, constituted of cells and extracellular matrix. This cap hardens the plaque; but it is also believed to strengthen it and prevent plaque rupture[10]. Figure 1.1 summarizes the different constituents of an atheromatous plaque.

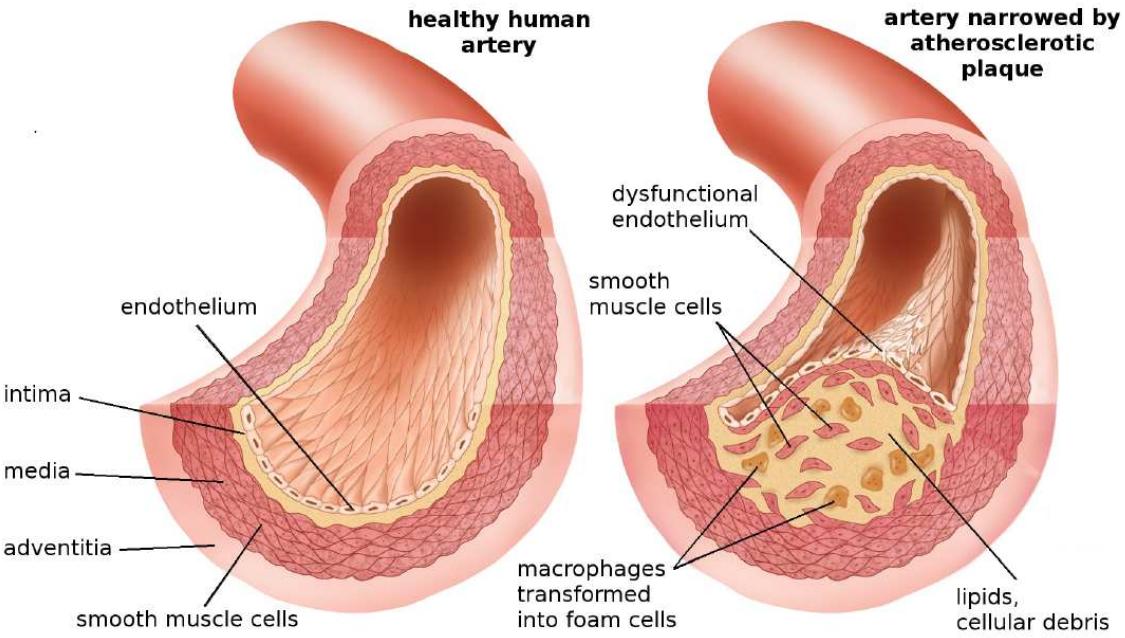

Figure 1.1: Atherosclerosis – left: normal human artery with the three layers: intima, media and adventitia – right: diseased vessel narrowed by an atheromatous plaque constituted of a lipid core surrounded by a fibrous cap – Adapted from the Encyclopaedia Britannica online[15]

Some arterial regions are more prone to the formation of atheromatous plaques than others (Figure 1.2). Indeed, it has long been known that zones of arterial branching, bifurcations and curvatures are more likely to be affected by the disease[16]. In these areas, the flow is highly disturbed and exhibits such irregularities as recirculation, flow separation, changes in flow

direction or even turbulence. The phenotype of the endothelial cells is also different. While nicely elongated in the direction of flow in zones of undisturbed flow, ECs exhibit a cuboidal (round) shape in the zones of disturbed flow. This change in EC shape is furthermore associated with EC dysfunction: the cells exhibiting this round shape are more permeable; produce less nitric oxide (NO) – which is involved in the control of SMC proliferation as well as in the regulation of platelet aggregation; proliferate more rapidly and exhibit enhanced expression of inflammatory genes[14] (Figure 1.2). This phenomenon is a major example of the importance of the micro-environment on the development of atherosclerosis. Indeed, not only are systemic factors implicated in the development of the disease but there are also local risk factors involved in atherosclerosis development, such as the local stresses and more especially the local flow field; the local composition of the extracellular matrix, which can affect among others cell adhesion and LDL deposition; and the local balance between pro- and anti-inflammatory factors[14].

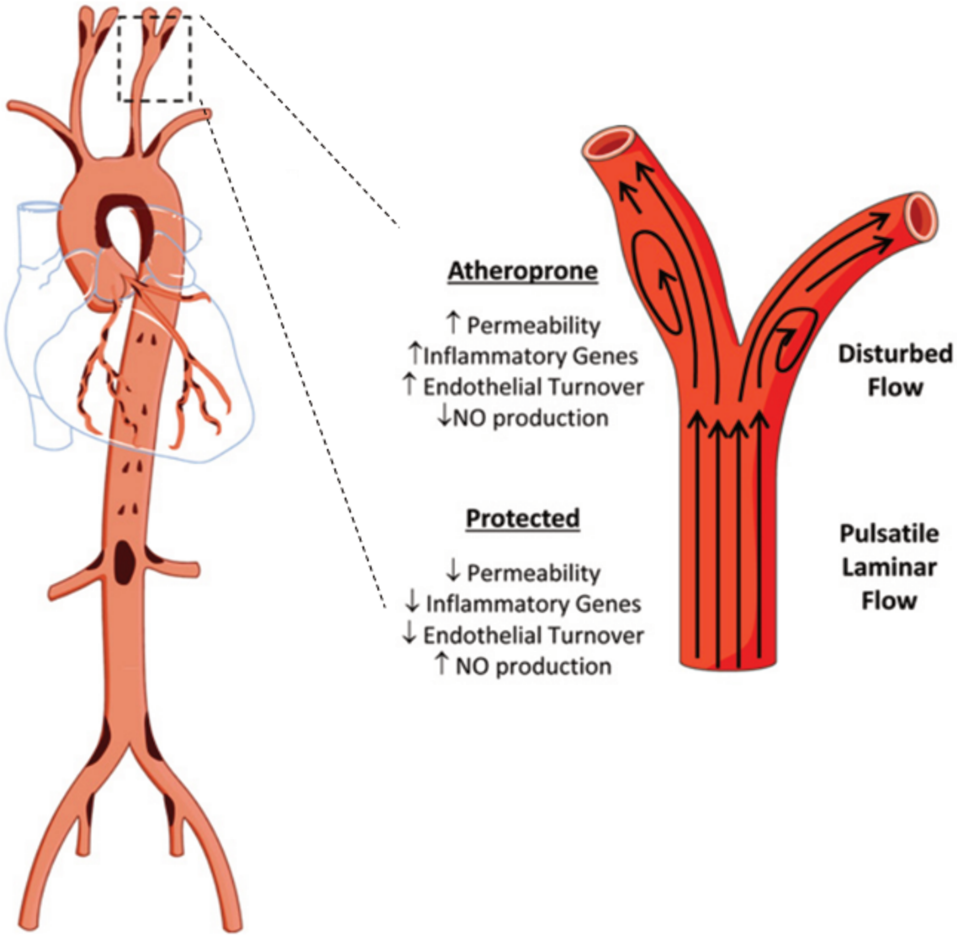

Figure 1.2: *left:* preferential localizations of atherosclerosis in the aorta and its main branches – *right:* endothelial cells' dysfunctions associated with disturbed flow – adapted from Yurdagul *et al.*[14]

1.3 Brief history of commonly used treatments for diseased coronary arteries

Historically, the only available treatment for acute myocardial infarcts due to plaque rupture or intra plaque hematoma was emergency bypass surgery. This procedure requires thoracotomy and is thus associated with an important morbidity. In this context, the development of angioplasty was considered as a true revolution in the field of cardiology. This technique developed in 1977 uses a balloon mounted on a catheter, inserted in the body via peripheral access (most commonly the radial or the femoral arteries) and guided until reaching the stenosed part of the vessel, where the balloon is inflated to push the plaque against the vessel wall and restore blood flow. Angioplasty thereby allows the treatment of chronic ischemia as well as acute events. However, angioplasty was associated to acute dramatic complication such as coronary dissection. Besides, the procedure is associated with high levels of restenosis defined as the recurrence of vessel narrowing[17], due to the combined effects of constrictive remodeling, neo intimal hyperplasia and elastic recoil.

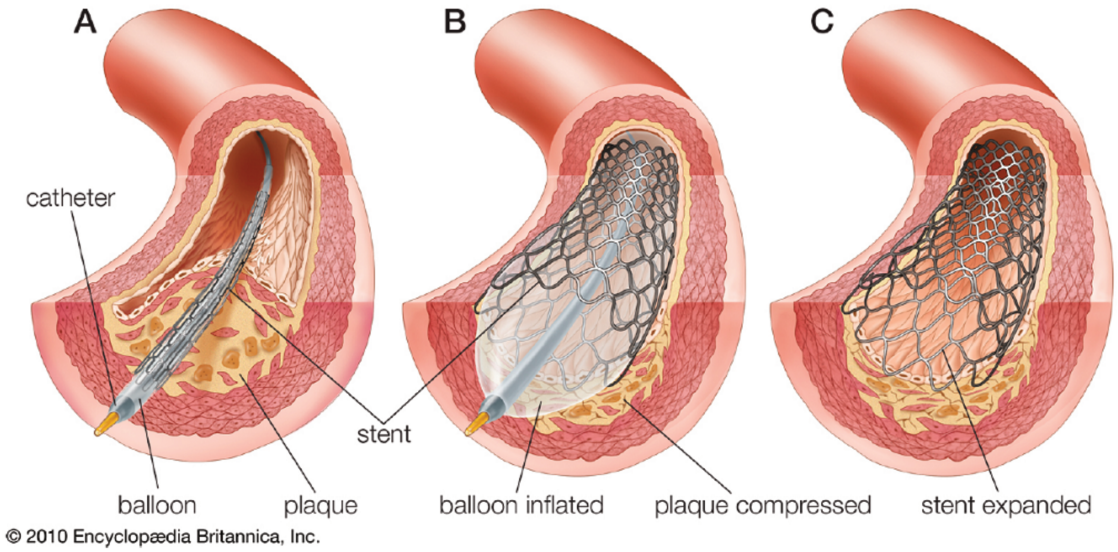

Figure 1.3: Stent implantation in an atherosclerotic artery. A: A balloon-mounted stent is introduced at the site of arterial occlusion. B: The balloon is inflated at high pressure to expand the stent and compress the atherosclerotic plaque against the arterial wall. C: The balloon is retracted leaving the stent in place as a permanent. From the Encyclopaedia Britannica Online[15].

Stents, wire mesh structures mounted on a catheter and inflated in the stenosed vessel thanks to a balloon (see
Figure 1.3), aim to avoid restenosis by preventing the artery from constrictive remodeling and elastic recoil[18,19]. The earliest stents, first used clinically in 1986 were made of bare metal, most commonly of stainless steel. Although highly effective in restoring blood flow and providing structural support to the diseased vessel, 20-30 % of bare metal stent stenting

procedures suffer from restenosis within ~6 months of stent deployment. This happens since the injury and the inflammation due to the deployment and the persistence of the stent in the arterial wall led to uncontrolled proliferation of smooth muscle cells and so to a thickening of the arterial wall. To avoid that, stents were then coated with antiproliferative drugs such as everolimus or sirolimus. Those stents achieved to drastically decrease the rates of restenosis[20,21]. Nevertheless, concerns about those devices rose several years after, since they were associated to non negligible levels of late stent thrombosis[22–24]. These thromboses are believed to be due to some stent struts remaining uncovered and in contact with the blood[25,26]. Indeed, in order for a stenting procedure to be successful, sufficiently rapid endothelial cell proliferation and migration must occur in order to repair the endothelial injury induced by stent deployment. Now, the antiproliferative coating prevents smooth muscle cells from proliferating and inducing uncontrolled neointimal hyperplasia, but it has also be shown to limit endothelial cell migration, thereby hindering the process of endothelial cells wound healing following injury. Late thrombosis is a rare event, but often deadly when it occurs, and can furthermore occur years after the stent deployment, when patients are no longer protected against blood clots by the first six months to one year dual anti platelet therapy given after the implantation of a drug-eluting stent (DES). Besides, this dual anti platelet therapy is yet far longer than the one given after the implantation of a bare metal stent (BMS) which is administrated for only one month. Those therapies are associated with a higher risk of bleeding which is not without consequences especially for elderly patients who are more prone to falls; and which renders any other surgical procedures very difficult. Thus, one would not want to extend this anti platelet therapy any longer. Moreover, another complication associated with both BMS and DES is that they disturb the local blood flow field[27]. These local flow disturbances have been shown to inhibit endothelial cell wound healing[28], thereby further compromising stent performance.

In light of the various problems associated with today's stent technology, there is a critical need for innovative solutions that address the various issues of arterial restenosis, thrombosis, and stent-induced flow disturbance. A potentially revolutionary solution is the concept of a bioresorbable stent (BRS)[29]. The idea would be to have a stent that remains in place only long enough to stabilize the arterial wall following stent-induced injury and then to degrade in a progressive fashion over a period of several months until it disappears completely.

BRS present several advantages. Firstly, contrary to conventional stents such as drug-eluting stents, the risk of long term thrombosis is expected to be reduced due to the absence in the long term of foreign material in the body. Consequently, the need for long term anti platelet therapy would also be reduced. Secondly, because BRS struts dismantle beyond a threshold level of degradation, the artery will no longer be caged which opens the possibility for positive remodeling of the vessel wall and associated late lumen gain[30,31] as well as for the progressive disappearance of the compliance mismatch between the stented and unstented segments of the artery. Thirdly, when the stent is fully degraded, the physiological vasomotion of the artery in response to pulsatile blood flow is expected to be restored. Finally, BRS degradation allows future treatment of the same arterial area and eliminates artifacts during thoracic imaging. One could also consider the problem from another point of

view and ask if there is any interest in having a permanent device in the coronary arteries. Colombo and Karvouni[32] compared biodegradable stents to Cincinnatus, the Roman dictator who humbly returned to his private life after serving his country, and so "fulfilled his mission and then stepped away".

The first BRS implanted in human in 1998 was the Igaki-Tamai stent made with a biodegradable polymer: poly-L-lactic acid (PLLA)[33,34]. It showed good results in term of safety and efficacy, but because of potential concern with the heat used to fasten the expansion - a heated contrast (up to 70°C) was injected in the balloon to facilitate the deployment, the clinical studies did not go further. A peripheral biodegradable stent based on the Igaki-Tamai stent, the Remedy™ stent has been developed and is sold in Europe since 2009. A new design for coronary disease is currently tested in pre clinical work[35]. The first BRS to be available on the market was developed by Abbott. This drug-eluting stent, the Biodegradable Vascular Stent (BVS) is also made of poly-L-lactic acid with an external layer of poly-D,L-lactic acid (PDLLA) which contains and releases the everolimus drug. In a first two-years trial – the cohort ABSORB A, they showed that BVS was safe; that there was no malapposed strut; and that it was bioasborbed at two years with a restored vasomotion[36]. Furthermore, eight patients from this cohort underwent imaging follow up at five years which showed late lumen gain between two and five years[31]. Because of concerns regarding the radial strength of the first version 1.0, a second version 1.1 was designed with an adapted geometry improving mechanical properties and a modified fabrication of the polymer leading to longer rate of degradation[37,38]. It now has the CE mark and more than 150,000 BVS have been implanted in patients until now.

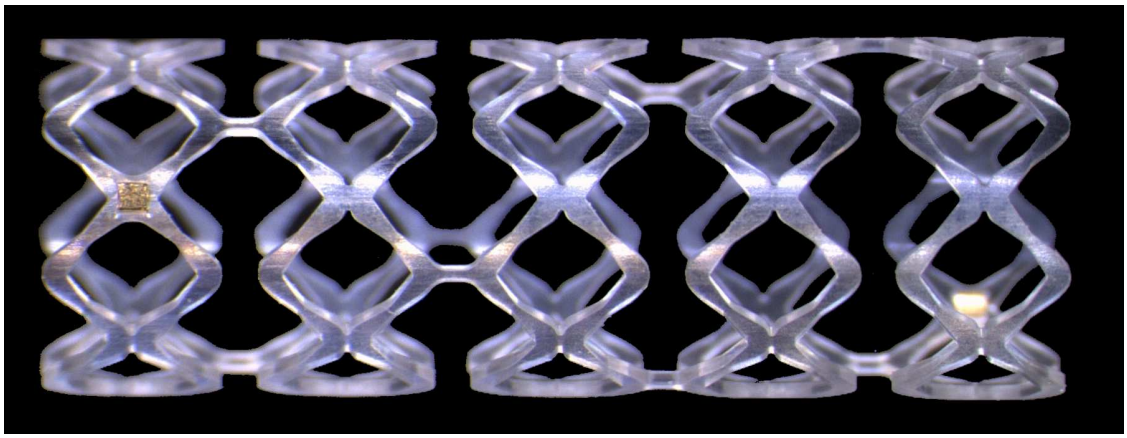

Figure 1.4: an example of biodegradable stent: the ART Pure Bioresorbable Scaffold (from ART website art-stent.com)

The REVA company built a stent including a slide-and-lock mechanism to increase the radial strength, but abandoned it because of poor results in clinical studies. Elixir Medical developed a drug-eluting BRS made of PLLA, the DESolve® stent, which also has the CE mark. Arterial Remodeling Technology (ART), a Paris-based start-up company has recently acquired the CE mark after the clinical trials ARTDIVA for the Pure Bioresorbable Scaffold (ART PBS) (shown on Figure 1.4). This scaffold made of poly-D,L-lactic acid (PDLLA) and not coated is

fully resorbed at two years, with a positive remodeling appearing as early as between the third to the sixth months[30]. The Tokyo-based company Terumo and ART are now collaborating to develop a coated version of the ART PBS and showed promising pre clinical work. Several others companies are currently developing BRS[39,40]. Most BRS are made of biodegradable polymers, but metals have also been considered as potential candidates. Thus, Biotroniks developed a stent made of biodegradable magnesium. The first design of their stent had a degradation rate of a few weeks – it showed complete absorption at two months – but first clinical studies showed dramatic consequences of this short time of arterial support, with high restenosis rates and target lesion revascularization having been needed for 45 % of all patients at one year[41]. This highlights the crucial importance of understanding the transient behavior of BRS and their interaction with the arterial wall.

1.4 Modeling biodegradable stents to improve their efficiency and safety

Biodegradables stents are thus complex devices expected to scaffold the artery long enough to allow for its healing, and to provide sufficient mechanical strength although their mechanical properties vary with degradation. Besides, note that the radial strength of polymers is usually lower than the strength of metallic materials, resulting in thicker struts for BRS than for conventional DES and BMS to ensure sufficient support. BRS thus furthermore need to exhibit acceptable geometries. However, there is a lack of understanding and characterization of the transient behavior of bioabsorbable materials. For now, their behavior is studied mainly by *in vitro* experiments and *in vivo* trial and error works which are long, expensive and difficult[35]. Thus, the need for theoretical models experimentally validated is crucial. Until now, many studies have described the deployment of stents alone[42] and modeled the balloon driven expansion[43–45]. Besides, several authors studied the stresses induced by the stent in the arterial wall, for various designs of stents[46,47] or different arterial and plaque properties[48]. Some studies have focused on the degradation of the stent and theoretical models of hydrolytic degradation of PLA[49]. And a few studies have taken into account the influence of stresses on the degradation of the stent, since this degradation has been experimentally shown to be accelerated by load[50–53]. Thus, Soares *et al.* for instance developed a theoretical[54] and computational[55] model of the load induced degradation of polylactic acid (PLA), considering a stent without an artery but using *in vivo* compatible loads. Debusschere *et al*. described the behavior of a metallic biocorrodible stent, considering both stress corrosion and pitting corrosion[56]. The coupling between stent and artery is taking into account by calculating at each time step of the corrosion the stresses experienced by the device. However, as far as we know, there is no model describing the complex coupling between a polymeric biodegradable stent and an artery during both deployment and degradation, integrating on a one hand the degradation of the BRS both hydrolysis and load driven, and on the other hand the stresses experienced by the artery and its biological remodeling.

1.5 Scope of the present work

In this study, we first aim to develop a theoretical model of the stent degradation process in order to describe the evolution of the stent mechanical properties with hydrolysis-driven degradation accelerated by the experienced loads – a combination of the residual loads due to the plastic deformation occurring during the deployment and the stresses induced by the arterial wall pushing the stent inward. Secondly, a theoretical model of the thickening of the wall in response to the injury and the stresses induced by the deployment and the persistence of the stent is developed, taking into account three phenomena: 1) the uncontrolled proliferation of SMCs in the absence of ECs, 2) the cell proliferation induced by inflammation, and 3) the wall thickening in response to increased experienced stresses. Thereafter, these laws of behavior are implemented in a computational finite element model using the multi-physics finite-element software COMSOL 5.1. The deployment of the stent is first modeled by a pressure-driven deployment simulating the inflation of a balloon. The resulting stresses and deformed geometries are then used as initial conditions for the second step modeling the stent degradation and arterial remodeling with an implicit method calculating at each time step the stresses to update the values of the stent mechanical properties and the arterial thickness.

As will be seen in the next sections, this computational model strongly depends on parameters characterizing the stent degradation and the arterial remodeling. For the stent, an interesting method to follow its degradation is optical coherence tomography (OCT), an intravascular imaging technique. OCT is a non-destructive and minimally invasive method that can be used both *in vitro* and *in vivo*. Furthermore, it has been shown that the appearance of stent struts on OCT images varies qualitatively with degradation. We aim to study the potential of OCT as a quantitative method to follow stent degradation and to determine parameters characterizing stent degradation. To this end, we allowed three types of stents to degrade in a saline solution at 37°C for two years and regularly performed OCT acquisitions. In collaboration with researchers from the laboratory of applied mathematics of Ecole Polytechnique, we developed a method to automatically detect the stent struts on OCT images and thereafter studied the quantitative evolution of the strut gray scale intensity (GSI) and used this quantity as a measure of the extent of stent degradation.

Arteries are known to be able to adapt their geometrical features to a perturbation in the experienced stresses in order to restore homeostatic values of those stresses. Our computational model takes into account the adaptation of arterial thickness to the increase in experienced hoop stress. However, it does not consider the arterial lumen adaptation to modified shear stress. Nevertheless, one could wonder if a stented vessel is still able to adapt its lumen diameter in response to modified blood flow even if caged by a stent; and thus whether or not this phenomenon should be taken into account. With the aim of comparing this adaptation for both BRS and BMS, we study the evolution of lumen diameter of porcine coronary arteries stented by BRS and BMS and followed by OCT, and deduce from these geometrical features an estimation of the experienced shear stress.

We will thus try to give some answers to the following questions:

- In chapter 2: how does a polymeric stent degrade? How does the arterial wall thickness vary in response to a stenting procedure?
- In chapter 3: could OCT be an interesting technique to quantitatively follow stent degradation and would it be useful to determine some parameters for more accurate computational models?
- In chapter 4: is an artery still able to adapt its lumen diameter to modified shear stress even if stented?

In the last chapter we will summarize the answers given to these different questions and then highlight some recommendations for future work.

CHAPTER 2

Deployment and Degradation of a Biodegradable Stent: a Coupled Computational Model between Stent and Artery

2.1 Introduction

Atherosclerosis and the resulting cardiovascular illnesses are the first cause of death in the world according to the World Health Organization[1]. In its advanced stages, atherosclerosis leads to the formation of a plaque that protrudes into the arterial lumen and obstructs blood flow. One of the most common treatments for atherosclerosis is the insertion of a stent, a wire-mesh structure that is mounted on a catheter, pushed to the stenosed portion of the vessel, and then deployed most typically via the inflation of a balloon catheter, with the aim of re opening the vessel and restoring blood flow[57]. It is estimated that more than 5 million coronary stenting procedures are performed in the world each year[58]. The first stents, bare metal stents (BMS), were initially used in 1986. Although broadly effective in restoring blood flow, they were associated with high restenosis rates – up to 20 to 30 % in early generations[17,18] – due to the uncontrolled proliferation of smooth muscle cells (SMC). To avoid restenosis, the next generation of stents, drug-eluting stents (DES), was coated with an antiproliferative drug. DES managed to drastically decrease the rate of restenosis[20,21] but were associated with an increased risk of late thrombosis[22–24], which can occur years after the insertion of the stent. This rare but often fatal event is thought to be mainly due to the persistence of uncovered struts because of the delayed re endothelialization[25,26]. Another complication associated with both BMS and DES is that they disturb the local blood flow field[27], which is thought to increase the likelihood of both restenosis and thrombosis.

In light of the various problems associated with today's stent technology, there is a critical need for innovative solutions that address the various issues of arterial restenosis, late thrombosis, and stent-induced flow disturbance. An interesting solution is the concept of

bioresorbable stents (BRS): stents whose aim is to remain in the artery for only the time they are needed and then disappear[29,59]. An advantage of BRS is the expected reduction in the risk of long term thrombosis due to the absence in the long term of foreign material in the body. The reduction in thrombosis risk also implies an expected reduction in long-term dual anti-platelet therapy. Another advantage of BRS is that strut dismantling and resorption during degradation frees the arterial wall from the caging effect present in BMS and DES which opens the possibility for positive wall remodeling and late lumen gain[30,31]. A third advantage is that BRS degradation progressively eliminates the compliance mismatch between the stented and unstented portions of the artery, which reduces the risk of stent complications[60]. Yet another advantage is that when the stent is fully degraded, the physiological vasomotion of the arteries in response to blood flow pulsatility is expected to be restored. Finally, BRS disappearance upon degradation opens the door for future treatment of the same vascular area and induces fewer stent-associated artifacts encountered during the use of imaging techniques such as magnetic resonance imaging (MRI).

The first BRS implanted in humans (in 1998) was the Igaki-Tamai stent which was made of the biodegradable polymer poly-L-lactic acid (PLLA)[33]. The Igaki-Tamai BRS showed good results in terms of both safety and efficacy; however, because of potential concerns about the heat used to fasten the expansion – a heated contrast (up to 70°C) was injected in the balloon to facilitate the deployment – the clinical studies were halted. A peripheral (rather than coronary) biodegradable stent based on the Igaki-Tamai stent concept, the Remedy™ stent, has more recently been developed and has been sold in Europe since 2009, and a new coronary design is currently in pre-clinical trials[35]. The first commercially available coronary BRS was Abbott's Biodegradable Vascular Stent (BVS), a poly-L-lactic acid (PLLA) DES. The first design of their BVS is largely bioasborbed at 2 years[61] and shows complete resorption by five years (no strut discernible on optical coherence tomography imaging (OCT))[31]. The second design degrades more slowly and the OCT appearance of the struts remains the same between 6 and 24 months[62]. More than 150,000 BVS have been implanted in patients to date. The REVA company developed a poly(iodinated desaminotyrosyl-tyrosine ethyl ester) carbonate biodegradable stent that has a slide-and-lock mechanism in order to increase radial strength; however, the design was subsequently abandoned it because of poor results in clinical studies. Elixir Medical developed a drug-eluting PLLA BRS, the DESolve® stent, which has received CE marking. Arterial Remodeling Technology (ART), a Paris-based start-up company has recently acquired the CE mark after the clinical trials ARTDIVA for the Pure Bioresorbable Scaffold (ART PBS). This scaffold made of poly-D,L-lactic acid (PDLLA) and not coated is fully resorbed at two years, with a positive remodeling appearing as early as between the third to the sixth months[30]. Several others companies are currently developing BRS[39,40].

While most BRS are made of biodegradable polymers, metallic BRS have also been considered as potential candidates. In this context, Biotroniks developed a biodegradable magnesium stent. The first design of that stent exhibited a degradation rate of only a few weeks with complete resorption at two months; but first clinical studies showed catastrophic consequences of this short time of arterial support, with high restenosis rates and target lesion revascularization having been needed for 45 % of all patients at one year[41]. This study

underscores the need for accurate determination of how long an artery needs to be maintained open by a stent and how stents need to be designed in order to provide sufficient support without inducing unacceptably high restenosis rates.

Biodegradable stents are complex devices that need to be sufficiently strong structurally to maintain the artery open and scaffold it during healing while simultaneously exhibiting favorable geometrical properties. This is especially important since polymeric biodegradable stents are considerably softer than metallic stents, thus typically requiring thicker struts to provide an equivalent radial strength. In addition, biodegradable stents need to degrade in a controlled manner so as to disappear when they are no longer needed. However, there is currently a lack of understanding and characterization of the transient behavior of bioresorbable materials whose mechanical properties vary with degradation. Typically, the behavior of bioresorbable materials is studied using either *in vitro* experiments or *in vivo* trial and error investigations that are long, expensive and difficult to perform and interpret[35]. Thus, the need for experimentally validated theoretical and/or computational models is crucial.

The literature contains many studies that have described the deployment of stents in arteries[46–48]. Some of these studies have focused on stent degradation and on models of hydrolytic degradation of PLA[49]. Although polymeric degradation has been experimentally shown to be accelerated by mechanical load[50,52,53,63], only a few studies have taken this effect into account. For instance, Soares *et al.* developed a theoretical[54] and computational[55] model of the load-induced degradation of a PLA stent using loads representative of those expected to be encountered *in vivo*. One limitation of this study is that it did not include interactions between the stent and the artery. Debusschere *et al.* described the behavior of a metallic biocorrodible stent, accounting for both stress corrosion and pitting corrosion[56]. The coupling between stent and artery was taken into account in this study by calculating at each time step of the corrosion process the stresses experienced by the device. To our knowledge, there is currently no model that describes the complex coupling between a polymeric biodegradable stent and an artery during both deployment and degradation and accounting for both hydrolysis- and load-driven stent degradation. Another major gap in the present literature is the absence of models that describe arterial wall biological remodeling in response to the dynamic stress field present after the deployment of a biodegradable stent and during the degradation process.

In light of the gaps identified above, the aim of the present study is to develop a computational model that describes: 1) the stresses within the stent and the arterial wall during BRS deployment, 2) the evolution of these stresses during hydrolysis- and load-driven BRS degradation, and 3) the biological responses of the arterial wall to the dynamic mechanical stress field. In the model, hydrolysis-driven degradation is accelerated by the stresses to which the stent is subjected, and these stresses are due to both residual stresses due to plastic deformation of the stent during deployment as well as stresses induced by interactions between the stent and the artery. The biological response of the arterial wall takes the form of wall thickening driven by three specific processes: 1) loss of endothelial cells provoked by the deployment of the stent which leads to uncontrolled proliferation of

SMCs 2) inflammation in the vessel wall due to both the arterial wound created by the stent and its degradation, and 3) homeostasis whereby the arterial wall adapts its thickness so that the hoop stress in the wall is restored to a stable homeostatic value. While homeostasis *in vivo* occurs for both hoop stress and fluid dynamic shear stress, only hoop stress homeostasis is considered in the model.

To develop the model, we focused on a PLA polymeric BRS. PLA is a biodegradable and biocompatible polymer metabolized via the Krebs cycle into carbon dioxide and water. It was first used in the biomedical field in the 1970's to make suture[64,65] and has since been widely used for various medical applications including orthopedic devices[66,67] such as screws or spinal cages[68,69], drug delivery systems[59] and stents[35,40]. An interesting property of PLA is that its rate of degradation and its mechanical properties can be tuned by varying specific aspects of its chemical properties such as the rate of crystallinity or the ratio of enantiomers[70]. We used a stent design and material properties that resemble those of a first generation ART BRS, which is made of poly-D,L-lactic acid (PDLLA) with complete resorption at ~24 months. We modeled the interaction between the stent and a model artery during both deployment and degradation.

2.2 Materials and methods

2.2.1 Theoretical model of stent degradation

The aim of this section is to obtain a description of the evolution of the stent mechanical properties with time which can subsequently be implemented into a computational model.

2.2.1.1 Chemical reaction of PLA degradation

Polymer degradation can be either hydrolytically- or enzymatically-driven. In the case of PLA, no enzymes are required and polymer degradation occurs spontaneously in the presence of water. PLA consists of chains of lactic acid monomers linked by ester bonds. During its degradation, those chains are randomly broken due to the hydrolysis of the ester bonds; this scission leads to the formation of a carboxyl end group and a hydroxyl end group according to the following reaction:

$$\sim \mathrm{COO} \sim + \mathrm{H_2O} \overset{\mathrm{COOH}}{\rightarrow} \sim \mathrm{COOH} + \mathrm{HO} \sim \qquad (2.1)$$

The presence of the carboxyl end groups allows for the acid-catalyzed hydrolysis of the ester bonds.

In the case of a biodegradable polymeric solid, degradation can occur either at the material's surface or within the entire volume. Polymers are thus classified as either surface-eroding polymers or bulk-eroding polymers[71]. The specific mode of degradation depends on the relative speeds of water diffusion within the sample and the rate of hydrolysis. If water diffusion speed is high compared to the hydrolysis rate, then the polymer will undergo bulk

erosion. Conversely, if water diffusion speed is small relative to the hydrolysis rate, then the polymer will undergo surface erosion. Burkersroda *et al.*[72] developed a theoretical model to compare water diffusion speed to the speed of hydrolysis, and they showed that the behavior of the polymer towards degradation also depends on the size of the sample. They defined a critical length for which the polymer will shift from surface degradation behavior to bulk degradation behavior. For poly(α-hydroxy-esters) such as PLA, they calculated this critical length to be several centimeters. Therefore, thin samples of PLA such as stent struts can be considered as bulk-eroding solids.

It has been shown that in a thick sample of amorphous PLA, little monomers or oligomers of lactic acid can remain trapped inside the sample, whereas if the sample is sufficiently thin, then the monomers and oligomers are evacuated toward the surface and do not stay trapped within the material. In a sufficiently thick material, this internal and local accumulation of acid degradation products leads to zones of lower pH and thus to increased catalysis. Thus, bulk erosion appears heterogeneous, with internal zones of the sample degrading faster[73]. This phenomenon appears not to occur for submillimeter samples[73] and is usually less pronounced for crystalline samples[73]. Therefore, it is not expected to apply to stents made of semi-crystalline PDLLA whose struts are 160 μm thick, so that hydrolysis within the stent can be considered homogeneous.

PDLLA is a semi-crystalline polymer; its degradation occurs faster in the amorphous regions, thus leading to an increase rate of crystallinity of PLA during degradation. This also means that the more crystalline the polymer, the longer its degradation time. Another consideration is that the right-handed enantiomer PDLA degrades faster than the left-handed PLLA. Controlling PDLA-to-PLLA ratio allows tuning the degradation rate to the desired level[70].

2.2.1.2 Kinetics of degradation

PLA hydrolysis has typically been described using first order kinetics[49,74]; therefore, the rate of production of the carboxyl end groups can be given by:

$$\frac{d[COOH]}{dt} = k'[ester][H_2O][COOH] \tag{2.2}$$

where $[COOH]$, $[ester]$ and $[H_2O]$ denote the concentrations of carboxyl end groups, ester groups and water, respectively, and k' a kinetic rate constant. In the early stages of degradation, the concentration of ester groups is very high compared to that of carboxyl end groups; therefore, $[ester]$ can be assumed constant. We also saw previously that water diffusion is far faster than water-induced hydrolysis and can therefore be considered as instantaneous[49], leading to a spatially homogeneous water concentration within the material so that $[H_2O]$ is also constant.

In light of these arguments, we can define a new hydrolysis kinetic rate constant $k_h = k'[ester][H_2O]$, and Equation (2.2) becomes:

$$\frac{d[COOH]}{dt} = k_h[COOH] \tag{2.3}$$

The constant k_h varies with external conditions of degradation such as load, pH and temperature. The temperature and pH are assumed constant in the body, while the effect of load will be explicitly taken into account in the next steps of the study. Since $[COOH] = 1/M_n$, where M_n is the number-average molecular weight of the polymer, the solution of Equation (2.3) yields[49,74]:

$$M_n(t) = M_{n,0} \times e^{-k_h t} \tag{2.4}$$

where $M_{n,0}$ is the number-average molecular weight of the polymer at the beginning of degradation.

To fix the value of k_h, we used measurements of the evolution of M_n for samples of ART stents that were allowed to degrade in physiological serum at 37°C over a period of three months. Plotting $\ln(M_n/M_{n,0})$ as a function of time yielded a linear correlation with excellent coefficients of determination R^2 ranging from 0.95 to 0.99, thus confirming the exponential behavior given in equation (2.4). This allowed us to establish that k_h lies in the range of 0.01 to 0.02 day^{-1}.

2.2.1.3 Evolution of the stent mechanical properties with hydrolysis-driven degradation

In their work, Vieira *et al*.[49] studied the *in vitro* degradation of suture fibers made of a blend of PLA and polycaprolactone (PCL), both biodegradable polymers. They showed that M_n – a chemical property – and the fracture strength σ_f – a mechanical property – evolve in the same manner; thus, they described the evolution of the fracture strength as:

$$\sigma_f(t) = \sigma_{f,0} \times e^{-k_h t} \tag{2.5}$$

where $\sigma_{f,0}$ is the fracture strength of the non-degraded polymer. To quantify the amount of degradation of a sample at a given time point, they defined a hydrolysis damage parameter as:

$$d = 1 - \frac{\sigma_f(t)}{\sigma_{f,0}} = 1 - e^{-k_h t} \tag{2.6}$$

Thus, d ranges from 0 for the non-degraded material to 1 when the sample is fully degraded.

Hooke's law describes the mechanical behavior of elastic materials and can also be used to approximate the behavior of inelastic materials undergoing small deformations. In this case, the relationship between stress and strain is linear. However, many polymeric materials fall in a regime where small stresses can induce large deformations, so that the displayed behavior is clearly non-linear[75]. New constitutive laws were necessary to describe the mechanical properties of such materials. Hyperelastic models such as the neo-Hookean law were developed to extend the linear theory of elasticity[75–77]. They are based on strain-energy functions for which the relation between stress and strain is no longer linear.

PLA, as well as many others polymeric materials, exhibit a hyperelastic behavior. Assuming they are isotropic, their mechanical behavior can be described by a neo-Hookean strain energy density function W[54,78], one of the simplest models for non-linear elastic materials which still has reasonable agreement with experimental data, given by:

$$W = \frac{1}{2}\mu(I_1 - 3) + \frac{\kappa}{2}(J-1)^2 \tag{2.7}$$

where μ is the shear modulus of the material, κ its bulk modulus, I_1 the first invariant of the right Cauchy-Green deformation tensor and J the determinant of the deformation gradient $\boldsymbol{F}$, describing the current state of strain and given by:

$$I_1 = {\lambda_1}^2 + {\lambda_2}^2 + {\lambda_3}^2 \tag{2.8}$$

$$J = \det(\boldsymbol{F}) = {\lambda_1}^2.{\lambda_2}^2.{\lambda_3}^2 \tag{2.9}$$

where λ_i denotes the principal stretches. For an incompressible material, $J = 1$; therefore, W is given by:

$$W = \frac{1}{2}\mu(I_1 - 3) \tag{2.10}$$

This form has been commonly used by various authors for the modeling of polymeric materials[78] and PLA[49,54] even if more complex hyperelastic laws can of course be used[49,53]. Soares *et al.*[54] defined the evolution of the shear modulus with degradation as:

$$\mu(t) = (1-d)\mu_0 \tag{2.11}$$

where μ_0 is the shear modulus of the non-degraded material and d the damage parameter, understood in their study as the fraction of broken bonds at a given location[54]. This linear relationship between the shear modulus and the degradation damage has also been verified experimentally by the team of Vieira[49]. We combined this concept of the shear modulus evolving with the damage parameter with equation (2.6) to obtain the following equation:

$$\mu(t) = \mu_0 e^{-k_h t} \tag{2.12}$$

which describes the evolution of the mechanical properties of the stent due to hydrolysis.

2.2.1.4 Evolution of the mechanical properties with load-driven degradation

Stents are subjected to mechanical load due not only to the residual stresses that develop as a result of the plastic deformation during deployment but also due to the load induced by the arterial wall pushing on the stent. Mechanical stresses are known to influence the degradation of polymeric materials. Indeed, various *in vitro* studies have demonstrated this phenomenon and have primarily described an acceleration of the degradation of the material, whatever the type of polymer: PLLA[53], PLA reinforced by 3D carbon fibers[63], blend of PLA and polyglycolic acid (PGA) [51,52], PDLLA and chitosan/glutin[52], etc. One *in vivo* study in rabbits[50] has also shown similar behavior. To the best of our knowledge, only the study of Deng *et al.* on PLA-PGL fibers[79] found no significant impact of load on the degradation of

polymer, but the stresses they applied were only 1 % of the baseline strength of their sample, and the results might have been different had higher stresses been used.

Different assumptions have been made to explain the phenomenon of load-accelerated polymer degradation[51,80]. One idea is that the applied load imparts a sufficient amount of energy to break the bonds in the polymer. Another idea is that the load decreases the activation energy of the chemical reaction and so accelerates it. Yet another concept is that the load induces morphological changes of the polymer facilitating the chemical reaction. We modeled the influence of the load by simply introducing an additional factor in the expression of the kinetic rate constant:

$$k = k_h + k_l(load) \tag{2.13}$$

where $k_l(load)$ is assumed to be a stepwise function of the load, taken as the von Mises stress within the stent. The function is assumed to evolve linearly with load up to a prescribed threshold L_{max} beyond which it saturates to a given value k_l^{max}.

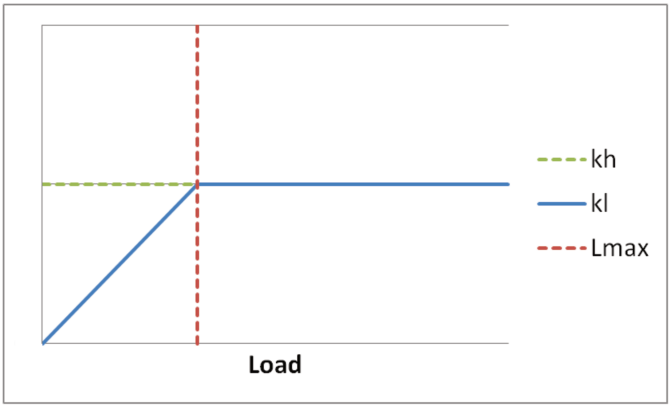

Figure 2.1: evolution of the function k_l(load)

The polymers tested in the *in vitro* studies we found in literature were of various types, but even for any given polymer – for example PLA – varying the chemical properties such as the degree of crystallinity or the rate of enantiomers modifies the degradation behavior considerably; thus, the experimental results are very sensitive to the exact properties of the polymer. As a result, although the literature data are broadly informative on the non negligible influence of load, it was not possible to determine precisely the constants corresponding to our polymer. However, because the literature seems to indicate that the acceleration due to load is experimentally of the same order of magnitude as that due to hydrolysis regardless of the type of the polymer tested[50–52], we assume $k_l^{max} = k_h$. In light of the above, Figure 2.1 schematically depicts the assumed behavior of k_l as a function of load.
We used several approaches to estimate the value of L_{max}, the load at which k_l reaches its maximum value. One approach is to consider that L_{max} corresponds to the load that imparts the total energy E_{tot} needed to break all covalent bonds in the polymer. PLA is a linear polymer whose chains are composed of ~1000 monomers of lactic acid.

Thus, the number of covalent bonds N_l would, to a first approximation, equal the number of monomers within the stent:

$$N_l = \frac{m_{stent}}{m_{LactAc}} = \frac{m_{stent} \times N_A}{M_{LactAc}} \tag{2.14}$$

where m_{stent} and m_{LactAc} respectively denote the mass of the stent and that of a lactic acid monomer, M_{LactAc} is the molecular weight of lactic acid and N_A is Avogadro's number. Thus, E_{tot} can be written as:

$$E_{tot} = \frac{E_{C-O} \times N_l}{N_A} = \frac{E_{C-O} \times m_{stent}}{M_{LactAc}} \tag{2.15}$$

where E_{C-O} is the energy of a mole of oxygen carbon bonds. Based on this analysis, we obtain $E_{tot} \simeq 39\,J$. Another approach is to think of L_{max} as the load needed to deliver the energy of polymerization of the polymer, i.e. the energy needed for monomers to become a polymer. Garlotta[81] gave an enthalpy of polymerization for PLA of $\Delta H = -27\,kJ/mol$. Using this approach, we obtain $E_{tot} \simeq 4\,J$.

To use these values in the context of our model, we need to determine the work W_{VM} of the von Mises stresses during the degradation of the stent, knowing that the stresses experienced by the stent push the stent struts inwards by around 10 µm between the beginning and the end of degradation. The corresponding energy is then equal to $W_{VM} \simeq 5.10^{-3}\,J$. Consequently, using this approach, E_{tot} would correspond to von Mises stresses that are three to four orders of magnitude higher than the ones experienced by our stent. Since the average von Mises stresses in the stent are $\simeq 10^7$ Pa, we estimate $L_{max} \simeq 10^{10} - 10^{11} Pa$.

Yet another approach to determine an order of magnitude for L_{max} would be to consider the *in vitro* experimental studies on how the degradation of polymers is accelerated by load. From these studies, one can deduce the values for k_l corresponding to the specific load applied to the samples and subsequently deduce the slope of the assumed linear dependence of k_l on load; this will allow determination of the threshold value of load for which k_h would be reached (since $k_l^{max} = k_h$ is assumed). Recall that $\mu(t) = \mu_0 \times e^{-kt}$, with $k = k_h + k_l(load)$; thus, if the degradations with and without load are compared, one can deduce the value of k_l for a given load from the following relation:

$$k_l(load) = [\ln(\mu_h/\mu_0) - \ln(\mu_l/\mu_0)]/t \tag{2.16}$$

where μ_l and μ_h are the degradations with and without load. A similar expression can be written in terms of M_n knowing that $M_n = M_{n,0} \times e^{-kt}$.

Using these relationships, we obtain the following results:

1. From the work of Fan *et al.*[52] on PDLLA foam, we calculate a k_l of 0.01 for a load of ~2x10^6 Pa, which means that k_h would be reached for an $L_{max} \simeq 4 \times 10^6\,Pa$, for PDLLA foam.

2. From the work of Miller *et al.*[50,82] on polyglycolic acid (PGA), we calculate k_l values of 0.04 and 0.09 for loads of ~1.6x10^{8}Pa and ~3.2x10^{8}Pa, respectively. From the evolution of M_n [83] we deduce $k_h = 0.1$. Thus, k_h would be reached for $L_{max} \simeq 4 * 10^8\ Pa$.
3. From the work of Wan *et al.*[63] on PLA reinforced with 3D carbon fibers, $k_l = k_h$ for a bending load of $L_{max} \simeq 10^7\ Pa$.

The results above are summarized in Table 2.1. To conclude, we clearly see from this literature review that our estimates for L_{max} vary over several orders of magnitude. As a result, in order to probe the sensitivity of the degradation results on L_{max}, we chose to launch simulations in which this parameter varied between 10^6 Pa to 10^{10} Pa.

The dynamic behavior of the stent with degradation and the variation of its mechanical properties are thus fully described by the following equation:

$$\mu(t) = \mu_0 e^{-(k_h + k_l(load))t} \tag{2.17}$$

which takes into account the hydrolysis-driven degradation of PLA as well as the acceleration of this hydrolysis by mechanical loading.

Table 2.1: Summary for the values of Lmax determined by different methods.

Lmax determined from				
Enthalpy of polymerization	Energy of all the C-O bonds	*In vitro* experiments		
		PDLLA foam Fan *et al.*[52]	PGA fibers Miller *et al.*[50]	PLA-c3d Wan *et al.*[63]
10^{10} Pa	10^{11} Pa	4×10^6 Pa	4×10^8 Pa	10^7 Pa

2.2.2 Theoretical model of arterial remodeling

A well documented arterial response to stenting during the first few months is neointimal hyperplasia, which corresponds to a thickening of the arterial wall due to the excessive proliferation of smooth muscle cells and the increased synthesis and deposition of extracellular matrix proteins. Neointimal hyperplasia can be thought of as an exaggerated scarring reaction of the artery in response to stent implantation. The aim of this section is to: 1) describe the various factors contributing to neointimal hyperplasia, 2) model the contributions of these factors to the thickening of the arterial wall, and 3) devise a law of behavior that describes the evolution of arterial wall thickness with time.

2.2.2.1 Neointimal hyperplasia due to the loss of endothelial cells

The deployment of a stent leads to extensive damage of the intima, the innermost layer of the artery which simply consists of a monolayer of endothelial cells (ECs) and basement

membrane. Histological studies have shown that a few days after endothelial denudation, some SMCs lose their contractile phenotype and acquire a proliferative and synthetic phenotype, with some cells migrating toward the intima. This, in combination with the synthesized extracellular matrix proteins, leads to the formation of neointimal hyperplasia, which thickens the arterial wall. A few weeks after full reendothelialization of the artery, SMCs return to their quiescent contractile phenotype. ECs have indeed been proposed as regulators of SMC proliferation, with the absence of ECs leading to greatly enhanced SMC proliferation[84,85]. In support of this notion, Asahara *et al.*[86] showed that following balloon denudation of rabbit carotid arteries, accelerating reendothelialization via the application of an EC-specific mitogen leads to a reduction in the wall thickening compared to control animals. Similarly, Sprague *et al.*[87] developed micro-grooved stents with the aim of facilitating EC migration and thus the reendothelialization of the wound. Comparison between micro-grooved and smooth-surface stents of the same design implanted in porcine coronary arteries showed increased reendothelialization at 3 days and decreased neointimal hyperplasia at 28 days. Therefore, the faster ECs are regenerated, the smaller the amount of neointimal hyperplasia. That is why we model the evolution of the wall thickness $w(t)$ due to the loss of EC using the following formulation:

$$\frac{dw}{dt} = A_1\big(N_{EC} - E(t)\big) \tag{2.18}$$

where N_{EC} is the number of ECs denuded due to stent deployment, $E(t)$ is the number of regenerated cells, and A_1 is a constant to be determined.

Following a stenting procedure, ECs have been reported to start proliferating from the edges of the wound[84,88] to heal the denuded area of the vessel. In healthy arteries, ECs are some of the most stable cells of the human body, with a doubling time of hundreds of days[12,89,90]. However, when needed, for example for angiogenesis, regeneration of the uterine membrane or arterial wound healing, ECs are capable of proliferating very rapidly, with a doubling time of only a few hours/days[12,89,91]. Thus, the rate of proliferation k_{div} of ECs is expected to change as the cell density increases with the progress of wound healing: this rate is assumed to start at a maximal value k_i at denudation and to progressively decrease towards the "regular rate" when $E(t)$ tends to N_{EC}, i.e. when the initially denuded area becomes fully covered by new ECs. This "regular rate" should be equal to the rate of death k_d, since the total number of endothelial cells in a healthy artery is expected to remain constant. We thereby define the evolution of k_{div} as a function of $E(t)$ by the following equation:

$$k_{div}(E) = \frac{k_i - k_d}{{N_{EC}}^2}(N_{EC} - E(t))^2 + k_d \tag{2.19}$$

where $k_{div} = k_i$ at the beginning of arterial remodeling, i.e. when $E(t) = 0$, and $k_{div} = k_d$ when the wounded artery is fully re-endothelialized, i.e. when $E(t) = N_{EC}$. Considering EC doubling times as described above, one can set $k_i \simeq 0.5$ created cells/day/number of existing cells and $k_d \simeq 0.01$ dead cells/day/number of existing cells. This behavior is depicted in Figure 2.2 for the specific case of $N_{EC} \simeq 140{,}000\ cells$.

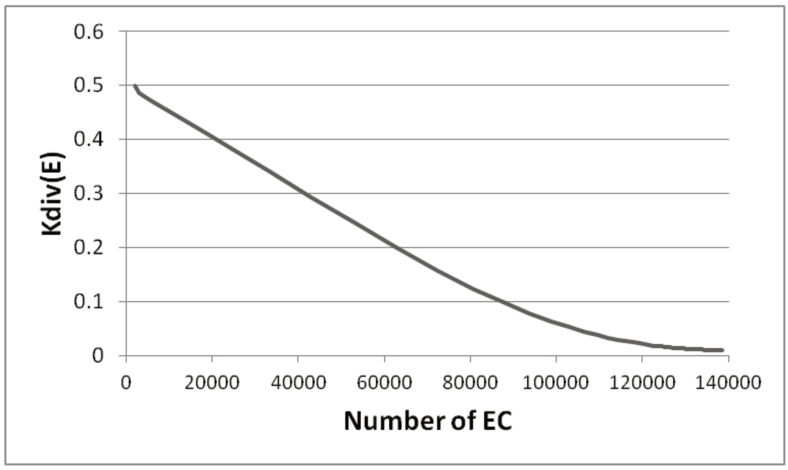

Figure 2.2: Evolution of $k_{div}(E)$ for Nec=140,000 cells.

During each time step Δt, the number of ECs regenerated is equal to the number of created cells minus the number of dead cells, that is to say:

$$E(t+\Delta t) = E(t) + E(t)\times[k_{div}(E) - k_d]\times\Delta t \tag{2.20}$$

Thus, we can write:

$$\frac{dE}{dt} = E(t)\times[k_{div}(E) - k_d] \tag{2.21}$$

with:

$$E(0) = N_{init} \tag{2.22}$$

where N_{init} is the initial number of ECs that remain viable immediately after stenting and thus proliferate to heal the arterial wound.

To determine N_{EC}, the number of ECs denuded by the stent, we need to know the density of ECs in a normal artery. To this end, we examined microscopic images in the literature of ECs from human mesenteric, mammary and epigastric arteries, which have approximately the same caliber as coronary arteries and can be used as coronary grafts for bypass surgery[92]. From these images, we estimate an average EC density of ≃1500 cells/mm^2. Considering a 1 cm-long stent in a 1.5 mm-radius artery, the number of denuded ECs is approximated to be $N_{EC} \simeq 140{,}000\ cells$.

In the stented portion of an artery, ECs have been reported to be largely denuded during stent deployment[85,93]. Autopsy studies have in some cases revealed no surviving ECs after stent deployment[94]. As already mentioned, new ECs that ultimately populate the denuded zone are believed to start proliferating from the edge of the wound to heal the artery[84,88]. Therefore, the initial number of cells N_{init} is taken as equal to the number of cells lining the two edges of the wound. To estimate the value of this parameter, we assume that each EC has an average width of 10 μm; therefore, a 10 μm-wide strip over the perimeter of the

lumen for both wound edges yields a value for $N_{init} \simeq 2{,}000\ cells$. This represents our initial estimate.

We also considered the fact that some authors have suggested that rather than proliferating from the edges of the wound, reendothelialization may also occur from patches of surviving ECs or even from the seeding of EC progenitor cells circulating in the blood. Tahir *et al.*[95] developed computational 2D models of EC regeneration and associated SMC proliferation for those two scenarios and compared them to the *in vivo* reaction of stented porcine arteries. They showed that considering patches of ECs described more accurately the evolution of wound healing observed *in vivo*, since considering this pattern allowed them to describe a homogeneous hyperplasia whereas considering ECs only originating at the wound edges led to higher hyperplasia at the center of the wound (reendothelialized later) than the proximal and distal parts (reendothelialized earlier). To take into account the hypothesis of patches of surviving cells[95,96], we will also consider scenarios where $N_{init} = 10{,}000\ cells$ and $N_{init} = 15{,}000\ cells$.

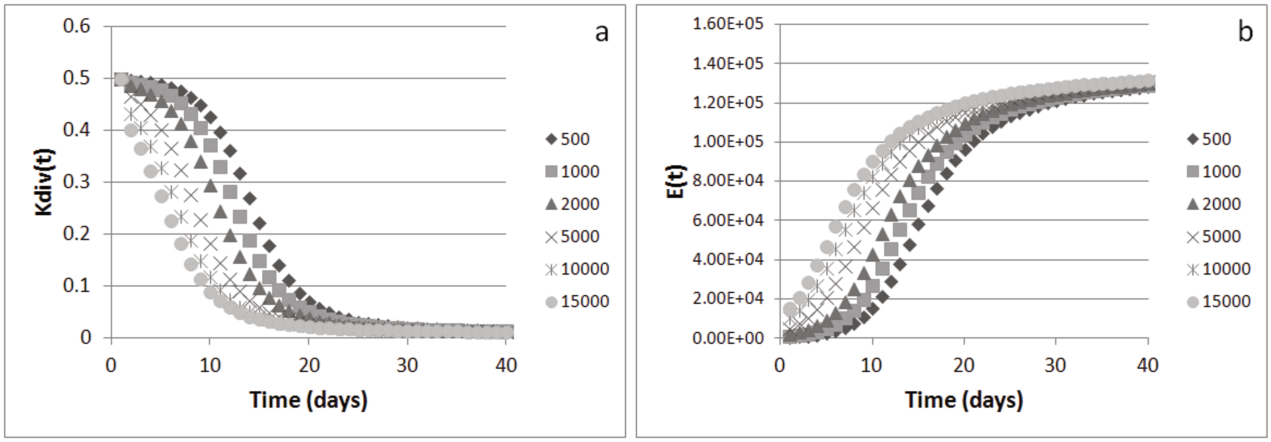

Figure 2.3: Evolution of $k_{div}(t)$ (a) and E(t) (b) for various N_{init}.

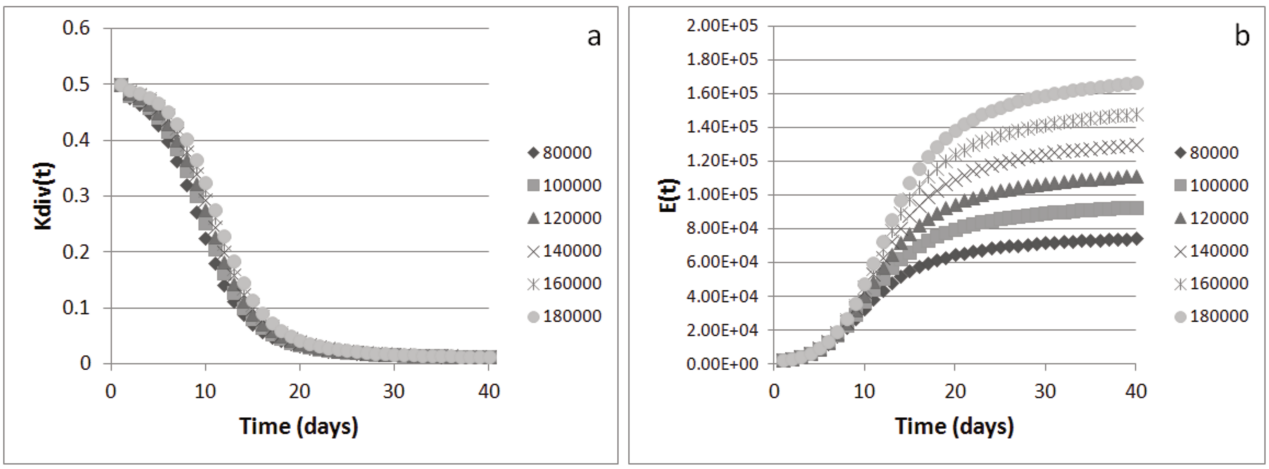

Figure 2.4: Evolution of $k_{div}(t)$ (a) and E(t) (b) for various N_{EC}.

Since equation (2.21) cannot be easily solved analytically, we studied the evolution of $E(t)$ with the recursive equation (2.20) and the initial condition (2.22). To better understand the influence of the total number of cells and the initial number of cells on the rate of division and the wound healing, we plot the evolution of k_{div} and $E(t)$ for various values for N_{init} and N_{EC} in Figure 2.3 and Figure 2.4. The results demonstrate that larger values of N_{init} are associated with a more rapid decrease in k_{div} and faster EC regeneration. Interestingly, N_{EC}, which represents the number of damaged ECs due to stenting, does not seem to have a large impact on the evolution of k_{div}. Another interesting finding is that although the final value of $E(t)$ increases with N_{EC} as expected, the time at which $E(t)$ reaches its plateau value is the same for all values of N_{EC}. We believe that this is the case due to the fact that k_{div} depends on the percentage of missing cells rather than the exact number of lost cells. Thus, in our model, increasing the initial number of ECs leads to an earlier repair of the wound, whereas decreasing the number of cells damaged by stent deployment does not significantly change the time at which the wound is repaired. It should be noted that either increasing N_{init} or decreasing N_{EC} will lead to an increase in wall thickening according to equation (2.18).

Based on the above, the parameters of the baseline model for the study of ECs are summarized in Table 2.2.

Table 2.2: Parameters for the baseline model of the evolution of the number of endothelial cells. k_i and k_d are in [number of created cells/day/number of existing cells] and [number of dead cells/day/number of existing cells] respectively.

$K_{div}(t)$		**EC**	
k_i	k_d	N_{ec}	N_{init}
0.5	0.01	140 000	2 000

2.2.2.2 Neointimal hyperplasia due to inflammation

Inflammation is known to induce cell proliferation and consequently hyperplasia. The wound provoked by the deployment of a stent triggers a rush of inflammatory cells. Moreover, the presence of stent polymeric materials[97] and BRS degradation products also induce inflammation. Inflammation induced by stenting can be quantified using inflammatory scores on histological sections. For instance, the following semi-quantitative score is widely used by authors[70,98] and defines four states of inflammation defined for each strut: 0: absence of inflammatory cells; 1: scattered monocyte-macrophage infiltrates associated with struts; 2: notable monocyte-macrophage infiltrates associated with struts; and 3: monocyte-macrophages circumscribing the struts. The data are subsequently averaged for the entire stent to provide a single overall inflammation score. Through our collaboration with ART, we have access to data on the evolution of the inflammatory scores one year after the insertion in pig arteries for the ART stent[99,100].

Since it has been shown that intimal hyperplasia increases with inflammation[98,101], we model the contribution of inflammation to the thickening of the wall by:

$$\frac{dw}{dt} = A_2 \times f(t) \tag{2.23}$$

where $f(t)$ represents the experimental evolution of the inflammatory score and A_2 is a constant to be determined.

Figure 2.5 depicts $f(t)$ for BRS represented as smoothed data extracted from the ART study previously described. In the case of BRS, the inflammation is taken as constant at a basal level of 0.33 during the first months, increases to 1.75 from 6 to 9 months, and finally decreases to an average of 0.95 thereafter. It is thought that the degradation of the stent may have contributed to the observed peak of inflammation at 6-9 months.

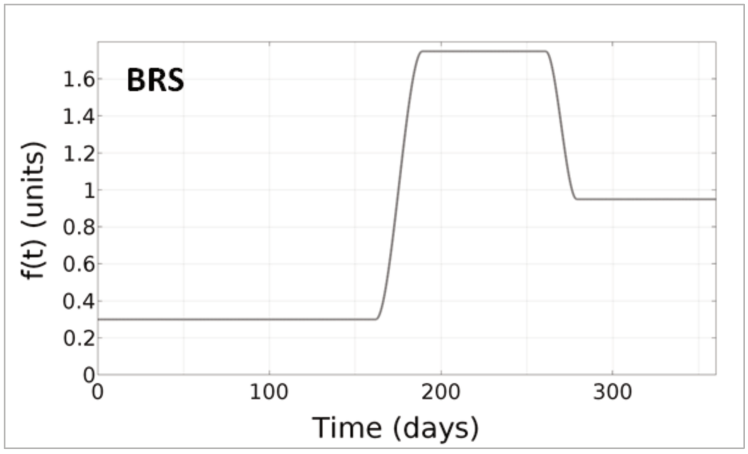

Figure 2.5: Inflammation scores for BRS

2.2.2.3 Arterial remodeling due to hoop stress

In response to a perturbation in its mechanical environment, an artery is able to modify its geometrical parameters, namely the vessel length, lumen diameter and wall thickness, in order to restore homeostatic values of the axial stress, shear stress and hoop stress[102]. Thus, an artery subjected to hypertension increases its wall thickness so as to maintain the hoop stress constant[103].

Stent implantation induces a significant increase in hoop stresses within the arterial wall. This is particularly important in light of data demonstrating a link between arterial stresses and that the incidence of restenosis as well as increased neointimal hyperplasia with an increase in arterial stresses[47,104,105]. We thus model the influence of the hoop stress $\sigma(t)$ on wall thickening as:

$$\frac{dw}{dt} = A_3[\sigma(t) - \sigma_0] \tag{2.24}$$

where σ_0 is a homeostatic value of the hoop stress, and A_3 a constant to be determined.

2.2.2.4 *Evolution of the overall arterial wall thickness with time*

The sections above described how loss of ECs, inflammation, and altered hoop stress in the arterial wall potentially contribute to arterial wall remodeling. Combining these three contributions, we obtain:

$$\frac{dw}{dt} = A_1\big(N_{EC} - E(t)\big) + A_2 \times f(t) + A_3(\sigma(t) - \sigma_0) \tag{2.25}$$

In a first step, we will show the results obtained for an idealized case with parameters empirically chosen as roughly relevant to describe what happens *in vivo* (meaning leading to arterial thickening of an order of magnitude similar to the *in vivo* situation). The evolution of the wall thickening with the loss of endothelial cells is simplified as:

$$\frac{dw}{dt} = A_1' \times e^{-0.033*t} \tag{2.26}$$

The inflammatory score is simplified as shown on Figure 2.6. The fixed values of σ_0, k_h, A_1', A_2', A_3' for this idealized case are summarized in Table 2.3.

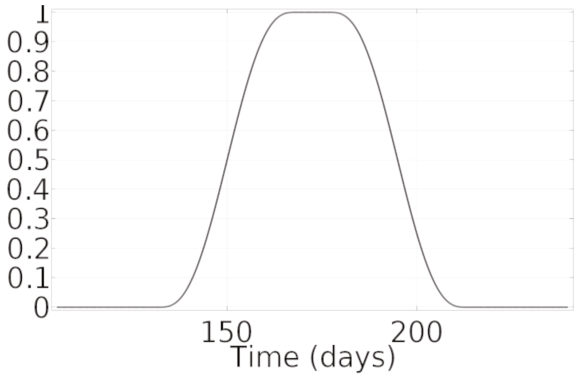

Figure 2.6: simplified inflammatory scores used in the idealized case

Table 2.3: parameters values for the idealized case

k_h	σ_0	A_1'	A_2'	A_3'
0.007	2.10^5 Pa	2.7µm/day	1.7µm/units/day	0.33µm/kPa/day

In a second step we aim to determine the relative weights of the three contributions (i.e. the values of the constants A_1, A_2 and A_3) from a literature study. Indeed, determining exact values for these constants would require extensive experiments that are beyond the scope of the present work. Nevertheless, we can find order-of-magnitude estimates for A_1, A_2 and A_3 by analyzing a number of experimental studies in the literature. The idea is to identify studies in which only one of the three contributions varies, in order to be able to understand its contribution. The estimated values of these three constants are provided in Table 2.4, and the bases for these values are described next.

Table 2.4: Determination of the weights of the three contributions to the arterial thickening.

A_1	A_2	A_3
0.2 µm/day/1000cells	5 µm/day/units	10 µm/MPa/day
Asahara *et al.*[86]	Kornowski *et al.*[98]	Timmins *et al.*[104]

Asahara *et al.*[86] studied the impact on arterial remodeling of the application of an EC-specific mitogen during 30 minutes after balloon denudation of rat carotid arteries. As no stent was used, the only contributions at stake here are inflammation and loss of endothelial cells. The amount of inflammation is considered to be the same for both control and test rats whereas the number of regenerated ECs varies because of the influence of the applied mitogen. The authors measured the area of reendothelialization at two and four weeks, which we converted into numbers of cells using the density of ECs we found for rabbits[106] (considered as closer to rats than humans) using the same method as previously described. They also measured the intima-to-media area ratio that we considered as a first approximation of the intima-to-media thickness ratio. Given the average value of rat carotid media thickness in literature (~60[107] to 110µm[108]), the thickness of the neo-intimal hyperplasia can be calculated. Comparing the control and test groups and assuming the level of inflammation is the same in both groups, it is possible to estimate $A_1 \simeq 0.2\ \mu m/day/1000\ cells$.

Kornowski *et al.*[98] studied the correlation between inflammation scores and neointimal thickness after the deployment of stents in pig coronary arteries. The scores and the thickness were calculated for each strut. Although some of the struts had an inflammatory score of zero, they still exhibited some neointimal hyperplasia. We presume that this hyperplasia is likely due to the stent-induced increase in hoop stress and loss of ECs. Comparing the thickness of the hyperplasia for struts having inflammatory scores >0 and those having scores =0, and assuming the hoop stresses and the number of damaged ECs are similar for both groups, we obtain $A_2 \simeq 5\ \mu m/day/unit\ of\ inflammation$.

Timmins *et al.*[104] studied the influence of two different stent designs on restenosis. Using numerical simulations, they showed that one of the stents induced higher stresses on the internal surface of the arterial wall relative to the other stent[46,104]. They deployed both stents in pigs and measured the amount of restenosis on histological sections at one month. They stated that the histological inflammation scores were the same for both designs. Considering that the number of damaged ECs is the same, comparing both stents designs allows us to estimate $A_3 \simeq 10\ \mu m/MPa/day$.

2.2.3 Computational model

The two preceding sections allowed us to describe the theoretical evolution of the mechanical properties of the stent with degradation as well as the evolution of the wall thickness in response to the injury provoked by the stenting procedure and its resulting

stresses. The aim of this section is to implement these equations into a computational model developed using the commercial finite element multi-physics code COMSOL 5.1.

2.2.3.1 Geometry of stent and artery

A 3D model of a closed-cell stent design is considered, with a Palmaz Schatz-like design and characteristics similar to the very first generation of ART stents (Figure 2.7). The struts are 160 μm thick. This strut thickness is larger than that seen in the case of BMS; this is needed to ensure adequate radial strength. To reduce computational costs, only 1/16th of the stent is represented due to geometric symmetry. Indeed, there is an orthogonal symmetry with respect to the axial mid plane of the stent and symmetries of rotation with the basic unit-cell shown in Figure 2.8 being repeated eight times. Moreover, the stent length consists of only three unit cells. This is justified because test simulations conducted in our group have shown that longer stents increase computational cost without having a significant influence on the results [data not shown].

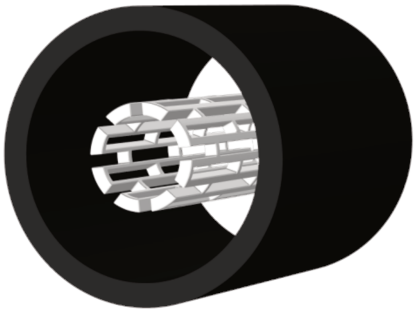

Figure 2.7: Initial geometry of stent and artery

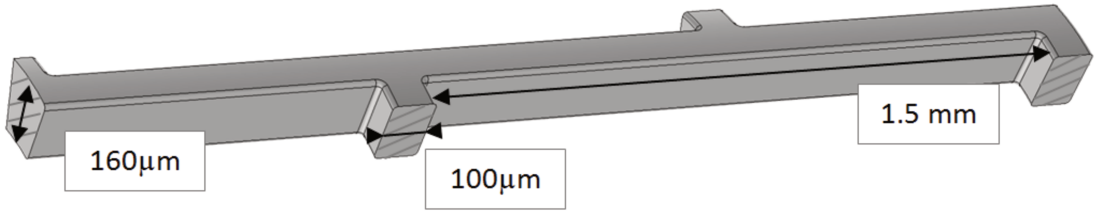

Figure 2.8: One 16th of the stent drawn with dimensions. The faces with stripes are the one submitted to symmetries.

In vivo, the arterial wall consists of three layers: the intima, the media and the adventitia. However, the media is primarily responsible for the mechanical properties of a healthy artery[11]. Therefore, our computational model considered a one-layer model for the artery (Figure 2.7). The arterial wall is assumed to be 300 μm thick and has a luminal diameter of 3 mm.

2.2.3.2 *Contact between stent and artery*

To model the contact between stent and artery, an augmented Lagrangian approach based on a penalty method is used. The penalty method prevents the surfaces in contact from interpenetrating. The augmented Lagrangian method is an adaptation of the penalty method which gives more accurate results as far as contact pressure is concerned. The contact is considered as frictionless.

In the contact pair created in COMSOL, the artery is considered as the "destination", which means that it is the material that deforms in response to the contact, whereas the stent is the "source", which means that it is the stiffer material that pushes the artery. It is the destination that is constrained not to penetrate the source.

2.2.3.3 *Mesh of stent and artery*

The geometry is discretized using tetrahedral and triangular elements. The mesh is finer at the location of strut intersections where gradients are expected to be the largest (Figure 2.9). To assess the quality of the drawn mesh, the density of the elements and their shape can be examined. For element shape, COMSOL defines a parameter ranging from 0 for a degenerate element to 1 for a perfectly regular shape. One should avoid too low an average quality since this can lead to convergence issues. Our final mesh demonstrated an average quality of 0.72 and readily achieved convergence.

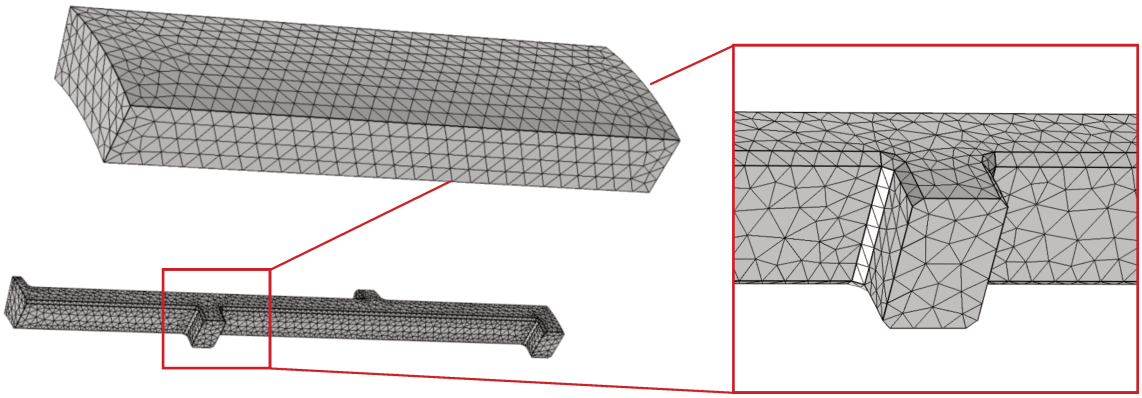

Figure 2.9: Mesh for the stent and the artery.

As in all computational simulations, it is essential to ensure that the results are mesh-independent. We performed separate mesh independence studies for the stent and for the artery. For the artery, the mesh independence study needs to show that the results are correct whatever the final thickness of the artery after remodeling. Thus, the study was performed on a model of stent deployment in an artery without stent degradation but with progressively increasing wall thickness until a final hyperplasia of 750 µm – which is higher than the expected final neointimal hyperplasia. The mesh independence study for the artery was conducted on this model for 12,396 nodes in the stent. To perform a variation of the arterial geometry, its mesh had to be as uniform as possible. We then progressively refined

the mesh by uniformly increasing the computational node density. The difference in the computed average von Mises stresses was calculated between a given mesh and the one with the next level of mesh density (Figure 2.10a) and is seen to be below 1 % once an arterial mesh density of 7,003 nodes is attained.

For the stent, the mesh independence study needed to show that the results are correct regardless of the final stage of degradation of the stent. Thus, the study was performed on a model of stent deployment and degradation without arterial remodeling. As will be detailed in the Results section, the regions of strut intersections are subjected to higher stress concentrations during deployment and degradation than other zones. Thus, the computational node density had to be particularly increased at these locations when considering finer meshes. The mesh independence study for the stent was conducted initially for an artery with 11,127 computational nodes and the mesh was subsequently progressively refined. The results demonstrated a difference in computed average von Mises stresses between a given mesh and the one with the next level of mesh density below 1 % once a stent mesh density of 12,396 nodes is reached (Figure 2.10b).

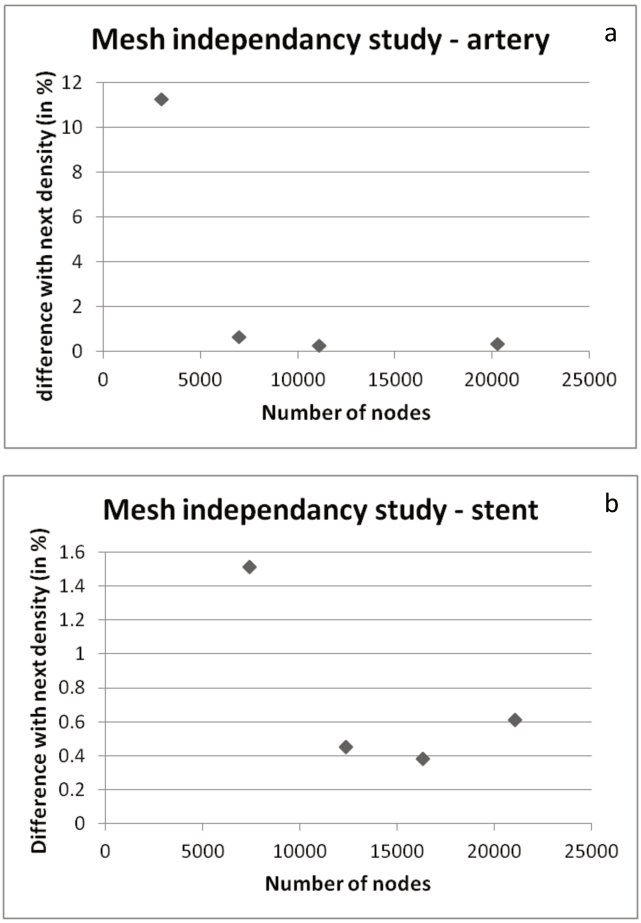

Figure 2.10: Mesh independency study for the artery (a) and for the stent (b). The difference for the results given for the average von Mises stresses are calculated between a mesh and the next finer one, for the last points shown here the difference has been calculated with a mesh of 27471 nodes for the stent and 29028 nodes for the artery.

2.2.3.4 Mechanical properties of the stent and the artery

As indicated above, the mechanical properties of the stent evolve with degradation as described by equation (2.17). The initial value of the shear modulus μ_0 is considered to a first approximation to be equal to one third of the Young's modulus of PLA as it would be for a linear elastic material. Literature values for PLA Young's modulus are 3-5 GPa[81,109]; however, due to computational issues in limiting the recoil of the stent post deployment, we used a value of 20 GPa. The bulk modulus for a nearly incompressible material is calculated to a first approximation using the equation: $\kappa = E/[3(1-2\nu)]$, where ν is the Poisson's ratio, which is assumed to have a value of 0.47 (nearly incompressible material). This expression would be exact for a linear elastic material. PLA density is taken as $\rho_{PLA} = 1300\ kg/m^3$[109]. PLA also exhibits plastic properties, which means that when the stress reaches the yield stress L_{max}, the material becomes ductile and its deformation is irreversible. PLA has a yield stress of 70 MPa[110].

Biological materials have been shown to usually behave non-linearly and can be well described using the hyperelastic constitutive law[111]. Thus, the artery is modeled as a hyperelastic, nearly incompressible material that follows a neo-Hookean behavior. The shear modulus is fixed to $\mu_a = 6.2\ MPa$[112], the bulk modulus at $K = 2MPa$ [113], and the density at $\rho_a = 960\ kg/m^3$. These are the values for a healthy artery. To model to a first approximation the influence of an atherosclerotic plaque, we investigated the sensitivity of the results to the shear modulus over the range $\mu_a/2$ to $2\mu_a$. This range was selected since atherosclerotic plaques can be either softer than the arterial media (in the case of young unstable plaque at high risk of rupture), of similar stiffness as the media, or stiffer than the media (for old calcified plaque)[48] (Table 2.5). The mechanical properties of the stent and the artery for the baseline model are summarized in Table 2.6.

Table 2.5: Different shear modulus for the artery to model in a first approximation the presence of a plaque.

	Healthy artery	**Soft plaque**	**Stiff plaque**
Shear modulus	μ_a = 6.2 MPa	$\mu_{soft} = 0.5\times\mu_a$ = 3.1 MPa	$\mu_{stiff} = 2\times\mu_a$ = 12.4 MPa

Table 2.6: mechanical properties of stent and artery

	density (kg/m^3)	**neo-Hookean model**		**Plastic properties**
		shear stress	**bulk modulus**	**Yield stress**
Stent	1300	6.7 GPa	111 GPa	70 MPa
Artery	960	6.2 MPa	2 MPa	-

2.2.3.5 Modeling the deployment phase

To computationally model stent deployment, a function $r_{balloon}(t)$ that represents the evolution of balloon radius with time is considered. The function evolves from $r_{init} = 0.5\,mm$ to $r_{max} = 1.45\,mm$ and then decreases again to r_{init} and thus represents the inflation and deflation of the balloon on which the stent is deployed. The general principle is to apply a pressure to the internal surface of the stent, calculated so that the stent-induced displacement follows the balloon inflation. When the applied pressure reaches zero, the stresses in the stent are the residual stresses due to the plastic deformation of the stent. After this point, an average blood pressure P_{int} of 100 mmHg is applied on the stent inner surface.

To this end, we first used a global equation defined in COMSOL as a pressure p applied to the internal surface of the stent and defined such that it satisfies the condition $A_v(r) - r_{balloon}(t) = 0$, where $A_v(r)$ is the average of the internal radius r of the stent calculated for the next to most distal strut and t is time[114]. Running this simulation leads to the deployment but also the deflation of the stent because the stent follows the displacement of the balloon. However, this procedure allows determination of the time t_{res} at which the applied pressure p reaches 0. Thereafter, we adapted the global equation defining the pressure p as given by:

$$[A_v(r) - r_{balloon}(t)]\times(t < t_{res}) + p\times(t \geq t_{res}) = 0 \tag{2.27}$$

where $(t < t_{res})$ and $(t \geq t_{res})$ are two Boolean expressions equal to 1 if true and 0 if false. The pressure applied on the stent p_{stent} was then defined as:

$$p_{stent} = p + P_{int}\times(t \geq t_{res}) \tag{2.28}$$

Therefore, from $t = t_{res}$ the stent is only subjected to the internal blood pressure and does no longer follows the deflation of the balloon; the degradation can then begin in the subsequent time steps. This two-step model enables one to use the deformed geometries as obtained at the end of deployment and the stresses calculated both in the stent and in the artery as initial conditions for the degradation step.

Not only is this parametric deployment of the stent more realistic than a one-step approach in which the stent displacement is imposed, but the ramping of the applied load also greatly facilitates the convergence of the non-linear problem. A parametric solver is used with continuation, meaning that the results of the previous time step are used to calculate the next time step. The time step used is not constant but is rather adapted to be smaller for the more challenging steps such as the time when stent and artery make contact, the time at which the embedment of the stent in the arterial wall is maximal, and the time points around t_{res} when the residual stresses are computed. Nevertheless, too small a time step poses difficulty because it can hamper convergence. Thus, due to the high non-linearity of both stent and artery and the contact modeling, the evolution of the time step size needs to be balanced carefully.

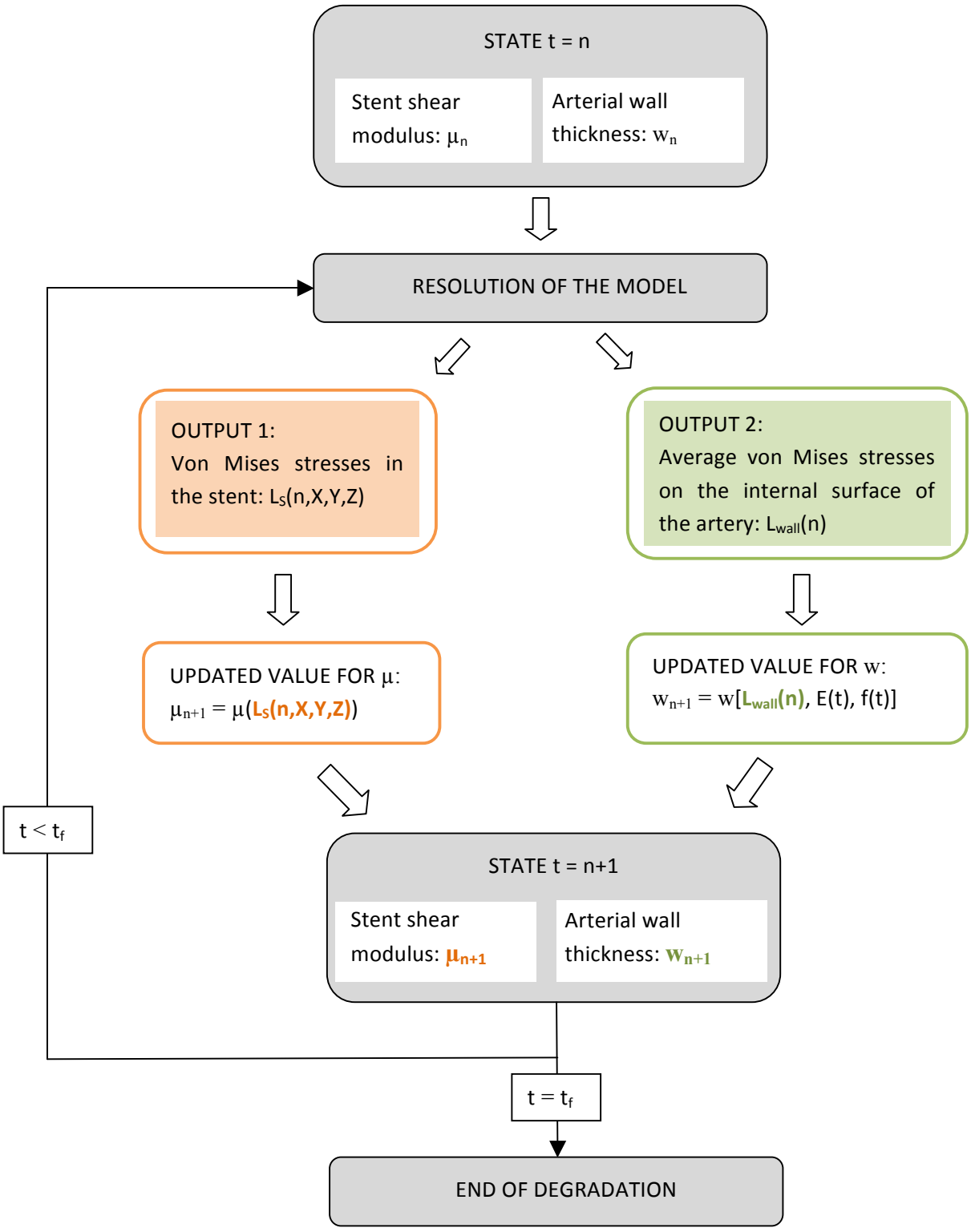

Figure 2.11: an implicit and recurrent method to model stent degradation and arterial remodeling: method to go from one step n to the following one n+1

2.2.3.6 Summary of boundary conditions

The stent and artery are constrained by three conditions of symmetry. A rigid body movement is prevented in all directions, and the problem is sufficiently constrained to allow for a force-controlled contact. Indeed, a displacement-controlled contact is usually easier to achieve than a force-controlled contact because the latter can lead to an initially ill conditioned system if the problem is not sufficiently constrained, especially if the contact is frictionless since sliding may be unconstrained. However, a force-controlled contact is desirable in our case since a method modeling the inflation of a balloon has been shown to be closer to reality to model the stent's deployment than a prescribed uniform displacement[45].

The boundary conditions are thus:

- three conditions of symmetry on both the stent and the artery
- a contact pair between the inner surface of the artery and the outer surface of the stent
- a pressure applied on the inner surface of the stent, initially set to zero
- a zero pressure on the outside surface of the artery.

2.2.3.7 Modeling the degradation phase

The degradation phase is modeled by the evolution of stent mechanical properties as already described. The material behavior law (2.17) is implemented in COMSOL. To account for the influence of mechanical loading on stent degradation, the considered loads are the von Mises stresses $L_S(t, X, Y, Z)$ at each point in the stent. Therefore, at each time step, the problem is solved, the stresses in the stent are computed and stored, and the new values of the shear modulus are calculated from the stored stresses and updated for the next time step. This implicit method used to model the evolution of the mechanical properties of the stent with degradation is detailed in Figure 2.11. We note that similar implicit methods using stored stresses to update a state of degradation have been used by Soares *et al.*[55] to model the load-driven degradation of expanded BRS made of PLA subjected to a constant inward pressure without considering an artery and, more recently, by Debusschere and co authors to model the degradation of biocorrodible metallic stents within an arterial wall[56].

The speed of degradation is a fundamental characteristic of BRS. To compare the situations of two stents degrading at different speeds, we used k_h extracted from the evolution of the number-average molecular weight of ART's PLA as described previously, but also a k'_h extracted from the evolution of M_n during the degradation of the Abbott stent BVS, a stent made of PLA that degrades in four to five years – that is to say twice to three times as long as the degradation time of ART stents. Two different designs have been developed for BVS, a first version called 1.0 and a second version named 1.1, exhibiting a slower hydrolysis rate and some geometrical modifications allowing for a more uniform stress distribution[37]. Only the second one is currently available on the market. Nevertheless, as far as we know, there is precise data in the literature about the evolution of M_n for the 1.0 version[61] but not for the 1.1 version. We thus chose to use two values of k'_h: 0.0055 which was deduced from the

literature values of the evolution of M_n for BVS 1.0[61], and half of this value as an estimation for BVS 1.1, as summarized in Table 2.7. As explained previously, we also launched several simulations with the yield stress L_{max} varying from 10^6 to 10^{10} Pa, with the value considered for the baseline model being 10^8 Pa.

Table 2.7: Different values for the rate of hydrolysis

	ART PBS	**BVS 1.0**	**BVS 1.1**
kh	0.01	0.0055	0.00275
From	experiments	Onuma *et al.*[61]	modeled as $k_{1.0}/2$

2.2.3.8 Modeling arterial remodeling

To model the thickening of the arterial wall, we used the "deformed geometry function" in COMSOL, which allows adding mass to the outside layer of the artery. The thickening is considered to a first approximation to occur at the outside surface of the arterial wall, as observed *in vivo* when the hoop stress is increased during hypertension[103]. It is of course recognized that stenting induces not only higher wall stresses (as occurs during hypertension) but also an arterial wound; therefore the remodeling after stenting *in vivo* is expected to also occur inside the lumen. This effect could not be taken into account due to computational limitations in COMSOL.

In the deformed geometry, displacements or speeds of displacement can be applied to the mesh. These displacements are defined in the material frame of reference, i.e. in the reference frame associated with the geometry, and thus on the initial geometry. The mesh is not refined but only stretched or compressed to follow the geometric variations; thus, the number of nodes remains constant. However, the mass and the volume change with time according to the geometric variations. The displacements are defined in the material reference frame as follows (Figure 2.12):

- no displacement on the inside wall of the artery;
- zero normal displacement on the faces where symmetry is applied;
- a prescribed displacement $w(t)$ on the external wall of the artery corresponding to the arterial thickening;
- the mesh inside the boundaries is free to deform.

Assuming quasi-static evolution of the arterial remodeling, it can be written that:

$$w(n+1) = w(n) + \Delta w \tag{2.29}$$

where $w(n)$ is the arterial thickness at time n, $w(n+1)$ is the arterial thickness at the following time step (n+1) and Δw is the variation of arterial thickness deduced from equation (2.25):

$$\Delta w = \left[A_1.\left(N_{EC} - E(t)\right) + A_2.f(t) + A_3.(\sigma(t) - \sigma_0)\right].\Delta t \tag{2.30}$$

As far as the hoop stress component of arterial remodeling is concerned, the load considered $\sigma(t)$ is the average von Mises stresses $L_{wall}(t)$ calculated at the internal surface of the arterial wall, since this surface is the one supporting the higher stresses and so is representative of the stresses induced by stent deployment. Those stresses are also the ones studied by various authors in the literature, which allows for comparison with previous work on this subject[46,104]. The average von Mises stresses calculated within the wall could have also been a good candidate; however, it was not possible in COMSOL 5.1 to determine and use at each time step the average value of the von Mises stresses calculated on a deformed volume. Thus, similar to the method described for the degradation of the stent, at each time step the mechanical problem is solved, the average stresses on the internal wall of the artery is computed and stored, and the wall thickness of the next time step is calculated from the stored stresses and updated. This implicit method is detailed in Figure 2.11.

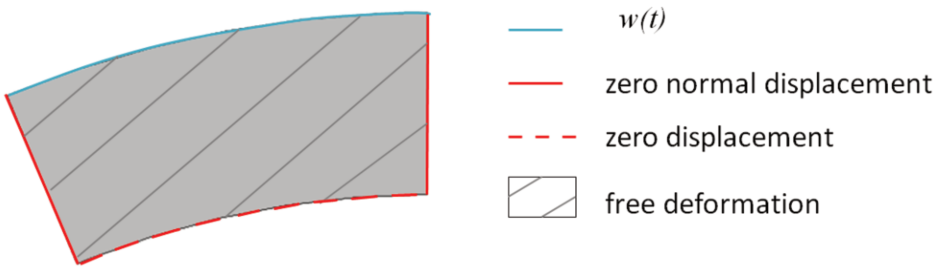

Figure 2.12: Applied displacements on the mesh during the arterial remodeling, shown on an axial section of the artery.

To determine the value of the homeostatic load σ_0, we first considered an artery subjected only to blood pressure and used the value of the load calculated at the inner wall as σ_0. However, upon implementing this approach, we obtained unrealistically large values of the wall thickness that far exceeded the expected ones. In this case, the average value of the hoop stresses at the inner arterial surface were equal to σ_0, but the stresses inside the wall were markedly smaller than the homeostatic values. In reality, one would expect the thickening of the wall to have a similar impact on the stresses at the inside surface as those within the wall when the average blood pressure is increased in order to restore homeostatic values for both stresses – as occurs in the case of hypertension[103]. However, this is not the case here because of the presence of a stent, which probably has a greater impact on the inside surface stresses than on the stresses within the wall. Thus, determining σ_0 is not obvious. We chose to use a trial and error method, making σ_0 vary and studying its influence on the remodeling. This is recognized as a limitation of the present model.

To better understand the individual contributions of endothelial loss, inflammation, and altered hoop stresses on arterial wall thickening, we initially studied these different effects separately. Once the effect of each of these contributions was understood, we combined them to determine their aggregate effect on wall thickening. The computational results for the evolution of the thickness of the arterial wall are compared whenever possible to experimental *in vivo* data on ART stents deployed in pig coronary arteries[30].

2.3 Results

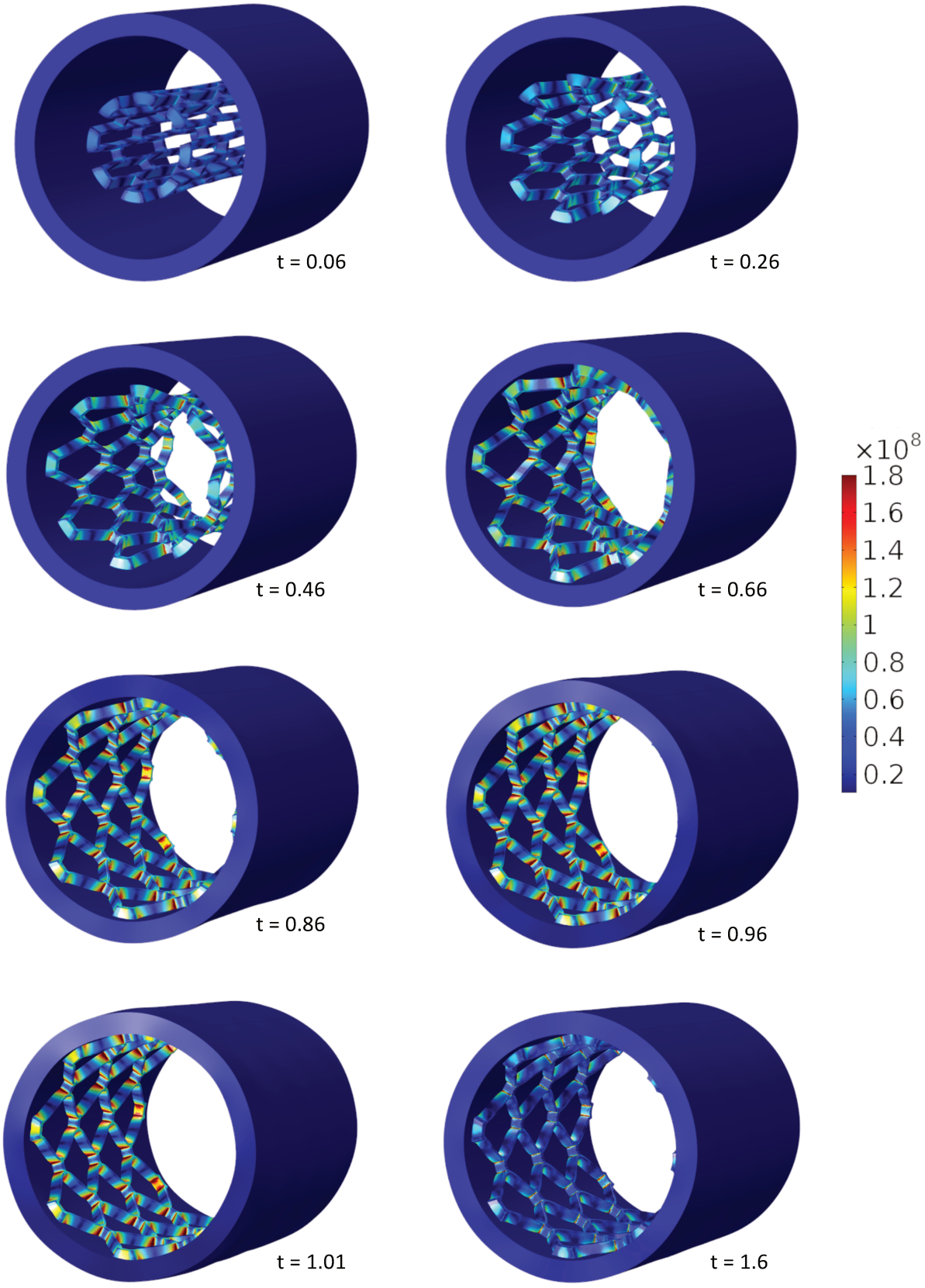

Figure 2.13: Average von Mises stresses (Pa) in the stent during deployment (from t = 0.06 to t = 1.01) and after elastic recoil (t = 1.6).

2.3.1 Deployment of the stent

2.3.1.1 Evolution of stent geometry during deployment

Figure 2.13 depicts a series of images of the stent deployment process and associated von Mises stresses within the stent. As can be clearly seen (see t=0.26, for example), the stent exhibits the so called "dogboning" effect, whereby the extremities of the stent are opened before the rest of the stent because of the smaller resistance to opening at the ends. The entire stent is deployed after this dogboning effect. This phenomenon corresponds to what is observed during an *in vivo* deployment of a stent. It should be noted that this effect would not have been observed with a simple imposed displacement[45], which underscores the need for deploying the stent via the application of an internal pressure. It is generally thought that excessive dogboning should be avoided in order to prevent the extremities of the stent from damaging the arterial wall. The dogboning $\mathrm{d_b}$ is defined in Migliavacca[42] as:

$$d_b = \frac{r_{distal} - r_{central}}{r_{distal}} \tag{2.31}$$

Where r_{distal} is the stent radius at the extremities and $r_{central}$ the stent radius at the centre. For our stent the maximal dog boning is of 0.23 at 0.65 s, and the final dogboning is of 0.0095. The deployment also induces a foreshortening f_S i.e. a reduction in the length of the stent due to its expansion; it is defined as[42]:

$$f_S = \frac{L_0 - L_{dep}}{L_0} \tag{2.32}$$

Where L_0 and L_{dep} are the initial and the final length of the stent respectively. In our baseline simulation shown in Figure 2.13, the foreshortening is here of 0.12.

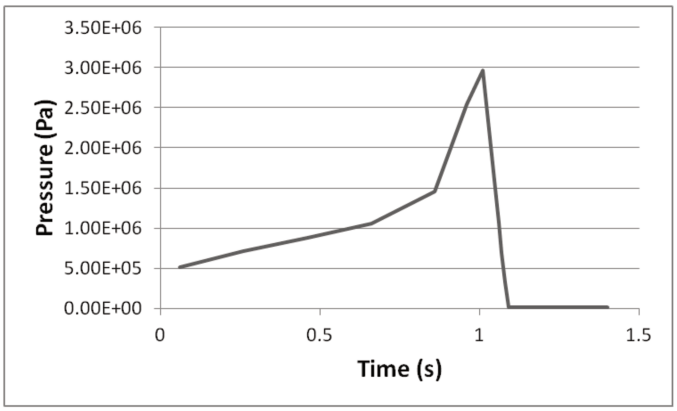

Figure 2.14: Evolution of the applied pressure during deployment.

As shown in Figure 2.14, the applied pressure initially increases smoothly and then more rapidly after $t = 0.86s$ to reach a maximum of 2.96 MPa. It then decreases rapidly until $t_{res} = 1.08s$. From that point onward, only the average blood pressure (100 mmHg) is applied to the stent.

The average stent radius increases continuously with time during the deployment phase (Figure 2.15a). The maximum embedment in time averaged over the length of the stent is ~100 μm. Immediately after deployment, the stent undergoes rapid elastic recoil and reaches a final average embedment in the arterial wall of ~30 μm which corresponds to a recoil of ~5.4 %. This value is comparable to that reported for BRS *in vivo*[30]. The *in vivo* embedment values are approximately 150 to 200 μm[30] [vascular surgeons, personal communication], but one fundamental difference is that the internal layer of the artery is extensively damaged during *in vivo* deployment – not only the endothelial layer but also the internal elastic lamina – and the stent penetrates within the arterial wall. Taking into account this phenomenon is beyond the scope of the presented work.

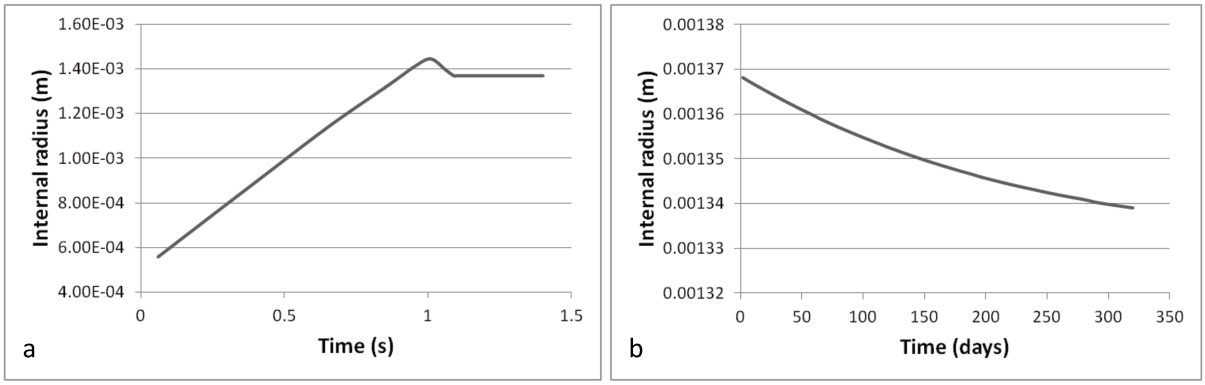

Figure 2.15: Evolution of the radius of the stent with time during deployment (a) and degradation (b).

2.3.1.2 Evolution of the von Mises stresses within the stent and the artery

From a qualitative point of view, the von Mises stress distributions shown in Figure 2.13 show that certain parts of the stent, most notably strut intersections, experience higher stresses than the other portions of the stent. This distribution of the stresses persists during deployment and after stent recoil. From a quantitative point of view, the stresses obviously increase during deployment, reach a peak at the end of it, and then decrease with the recoil. The stent is eventually subjected to the residual stresses due to plastic deformation and to the stresses induced by the arterial wall pushing it inwards.

As illustrated in the cross-sectional views in Figure 2.16, the von Mises stresses within the arterial wall reach their peaks not surprisingly at the zone of contact between the stent and the artery both during deployment and after recoil. Similar to the evolution of the stresses within the stent, the stresses within the arterial wall initially increase, reach a peak and then decrease with stent recoil.

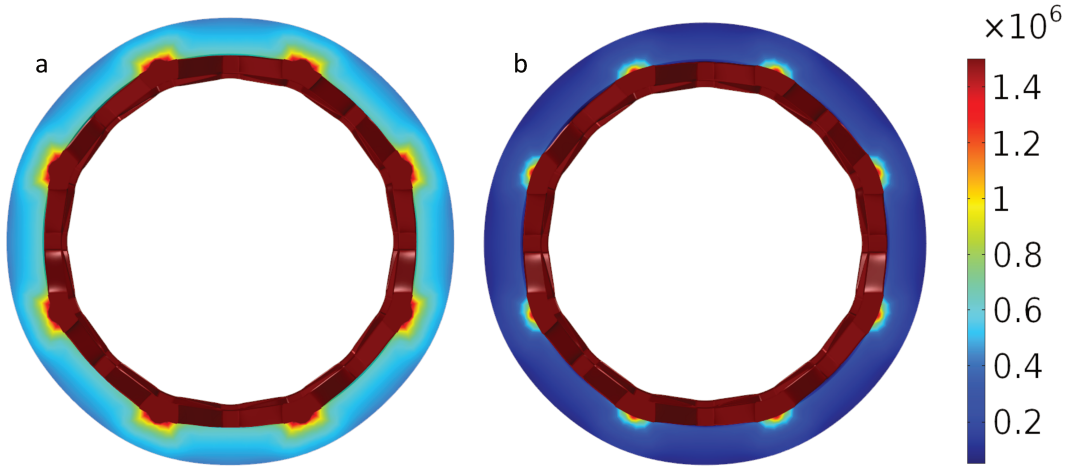

Figure 2.16: Average von Mises stresses in the arterial wall (Pa) at the maximal point of embedment (a) and after elastic recoil (b).

2.3.1.3 Influence of the variation of the shear modulus of the artery

Varying the value of the shear modulus μ_a of the arterial wall changes the extent of stent embedment. The stiffer the wall, the smaller the embedment (Figure 2.17). Whereas the influence of the stiffness of the artery on the maximal embedment is moderate – a decrease of only 2 % and an increase of only 2 % for the stiffer and softer walls, respectively – the final embedment is decreased by 15 % if the shear modulus is twice the initial one and increased by 19 % if the shear modulus is half the initial one.

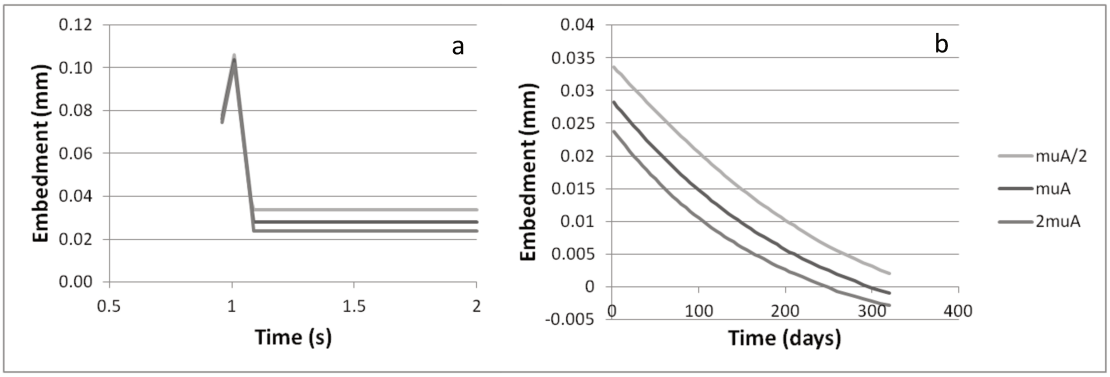

Figure 2.17: Influence of the shear modulus of the artery on the average embedment during the deployment (a) and the degradation of the stent (b).

Varying the shear modulus μ_a has a marked effect on the average von Mises stresses within the artery. At the point of maximal embedment of the stent, these stresses are increased by 39 % for the stiffer wall and decreased by 34 % for the softer wall (Figure 2.18a). After recoil, the stresses are increased by 24 % and decreased by 24 % for the stiffer and the softer walls, respectively. The stresses in the stent during the deployment phase are insensitive to the stiffness of the arterial wall (Figure 2.18b). During this phase, the stresses are very likely

primarily due to the applied pressure, and the contribution of the arterial wall is negligible. However, after stent recoil, the stresses in the stent are increased by 6.0 % and decreased by 6.5 % for the stiffer and the softer arteries, respectively.

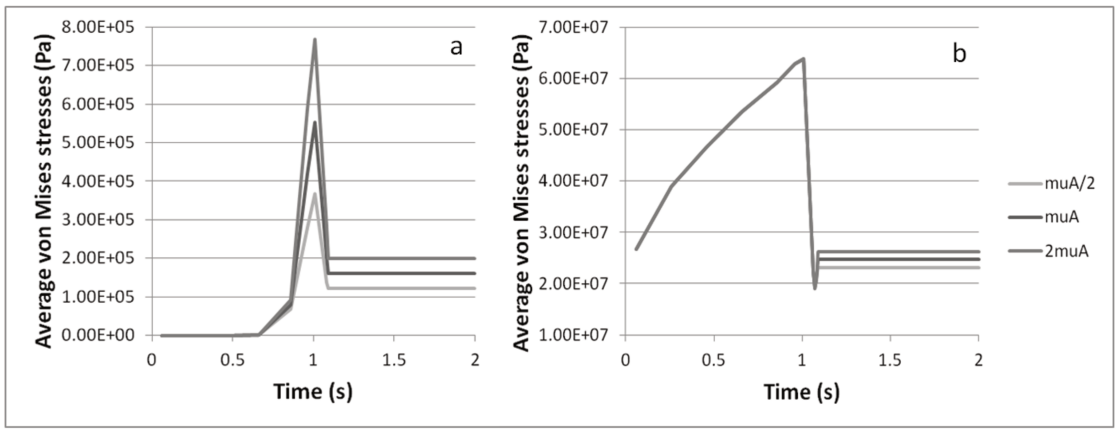

Figure 2.18: Influence of the shear modulus of the artery on the von Mises stresses in the artery (a) and in the stent (b) during deployment.

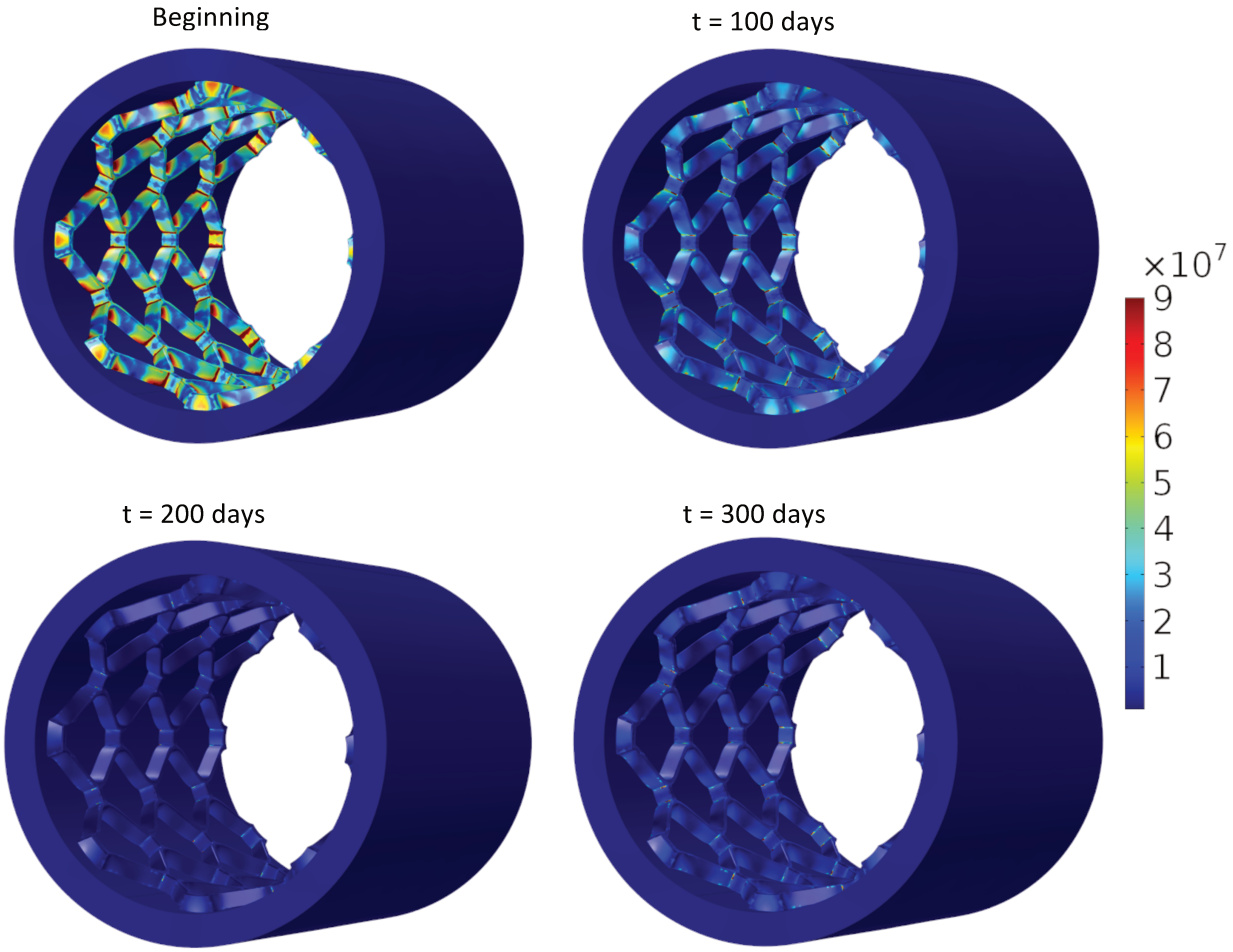

Figure 2.19: Von Mises stresses (Pa) in the stent at the beginning, at 100 days, 200 days and 300 days of degradation

2.3.2 Hydrolysis-driven degradation is accelerated by the mechanical load

2.3.2.1 Internal radius of the stent

During degradation, the stent radius decreases progressively (Figure 2.15b). For the baseline model, the decrease is 2.1 % of the post-recoil radius at 10 months. From that time point onwards, the stent is so weak that it is on average no longer embedded in the artery. Due to the dogboning effect, some portions of the stent remain embedded but others progressively detach from the vessel wall.

2.3.2.2 Von Mises stresses in the stent and in the artery during degradation

Qualitatively, the zones experiencing the highest stresses, namely the intersections of stent struts (Figure 2.19) and the zones of contact between the struts and the arterial wall (Figure 2.20), remain unchanged during stent degradation. The average von Mises stresses in the stent and in the arterial wall exhibit largely similar time evolution, decreasing slowly with degradation. Relative to the beginning, the average von Mises stresses at the 10 month time point are reduced by a factor of 6.2 for the artery and 12.1 for the stent.

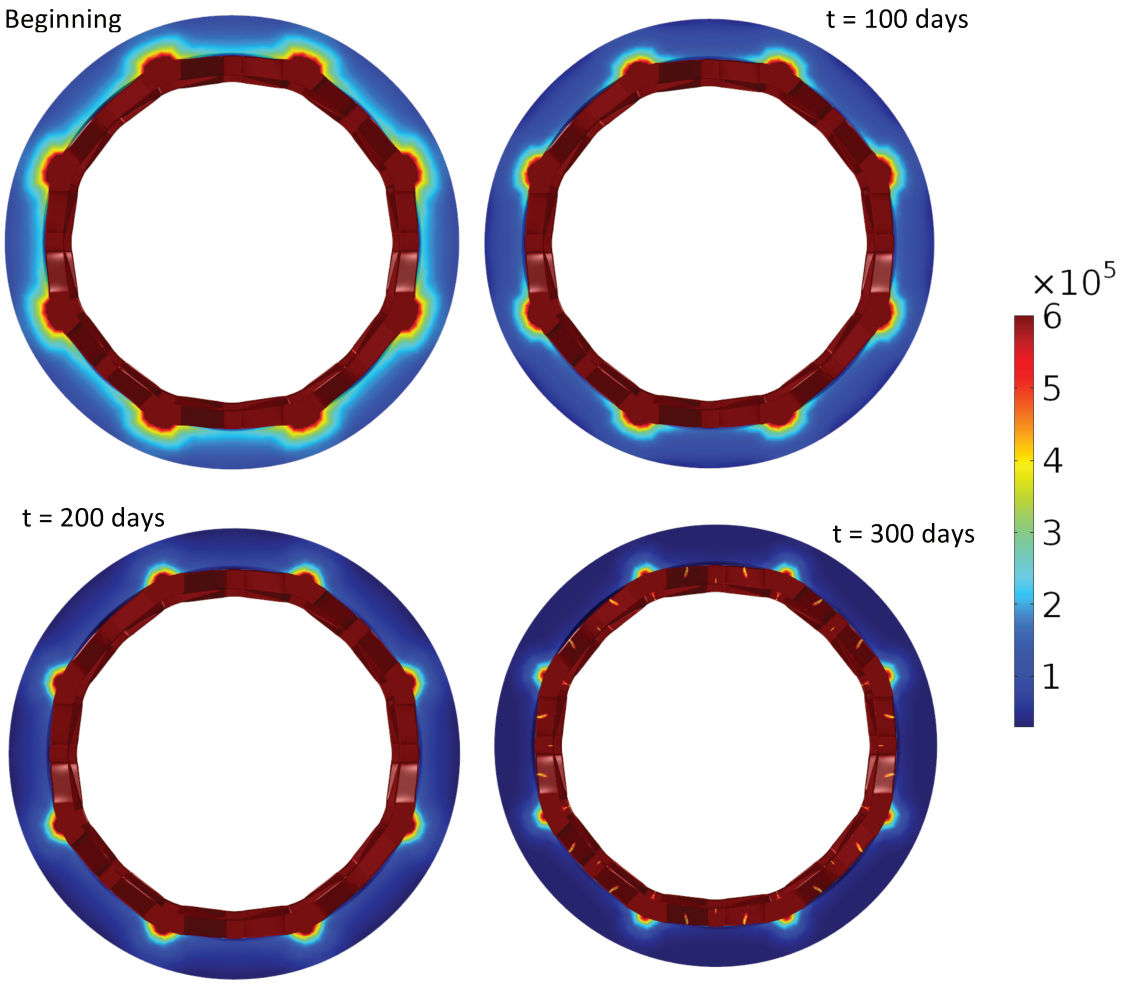

Figure 2.20: Von Mises stresses (Pa) in the artery at the beginning, at 100 days, 200 days and 300 days of degradation.

2.3.2.3 *Evolution of the shear modulus of the stent*

BRS degradation is modeled here as a progressive decay in stent mechanical properties driven by both polymer hydrolysis and the mechanical stresses within the polymer. Water diffusion is assumed instantaneous and so spatially homogeneous within the material; thus, the degradation due to hydrolysis is spatially homogeneous within the stent. However, the spatially heterogeneous mechanical stress field within the stent induces inhomogeneous degradation, as can be clearly seen in Figure 2.21b which depicts the heterogeneous distribution of the shear modulus μ at the end of degradation (the initial shear modulus is spatially uniform and has the value μ_0 – Figure 2.21a). The effect of mechanical loading is more pronounced at strut intersections corresponding to the stent areas subjected to the highest stresses. As a result, those areas are the most fragile and may be the first to exhibit discontinuities during stent dismantling.

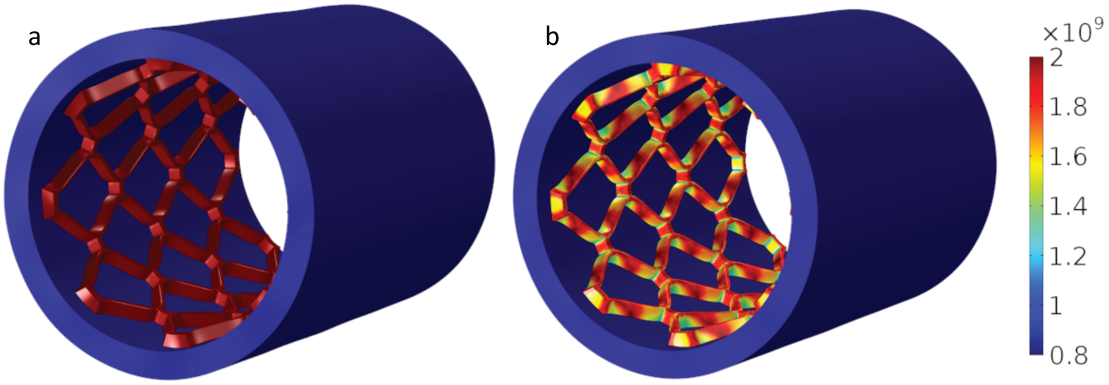

Figure 2.21: Color map of the shear modulus (Pa) of the stent at the beginning (a) and at 120 days of degradation (b).

A plot of the standard deviation of μ (normalized by its average value), which is a good measure of the spatial heterogeneity of stent degradation, reveals that for the baseline model this heterogeneity increases until 4.5 months and then begins to decrease beyond that point (Figure 2.22b). In fact, the areas of the stent where μ decreases the fastest are those subjected to the highest stresses, thus leading to not only a decrease in mechanical properties but also a reduction of the stresses in those areas. Thus, a homogenization of the stresses within the stent ultimately occurs. This may explain the behavior seen in Figure 2.22b.

2.3.2.4 *Influence of the kinetics of degradation*

According to their chemical properties and the fabrication processes, the speed of degradation of BRS can be adjusted. Figure 2.23 and Figure 2.22 depict the evolution of different quantities of interest for three values of k_h corresponding to three different degradation behaviors as detailed in Table 2.7. The higher the value of k_h, the faster is the decrease in arterial (Figure 2.23a) and stent (Figure 2.23b) stresses. At 10 months, arterial wall stresses are reduced by factors of 6.2, 2.6 and 1.6 for ART PBS, BVS 1.0 and BVS 1.1

respectively. The equivalent drops for stresses in the stent are 12.1, 4.0 and 2.1. The decay in mechanical properties (Figure 2.22) is more pronounced and more rapid for the ART stent, which is likely to lead to earlier dismantling of that stent relative to the Abbott stents, thus allowing an earlier positive remodeling. Besides, the maximum heterogeneity of the shear modulus occurs at a later time point when the stent degrades more slowly. More specifically, it occurs at 8 months for a $k_h{}'$ = 0.0055 and at 15.5 months for a $k_h{}'$ = 0.00275. However, the maximal values reached for the heterogeneity are nearly identical for the three rates of degradation.

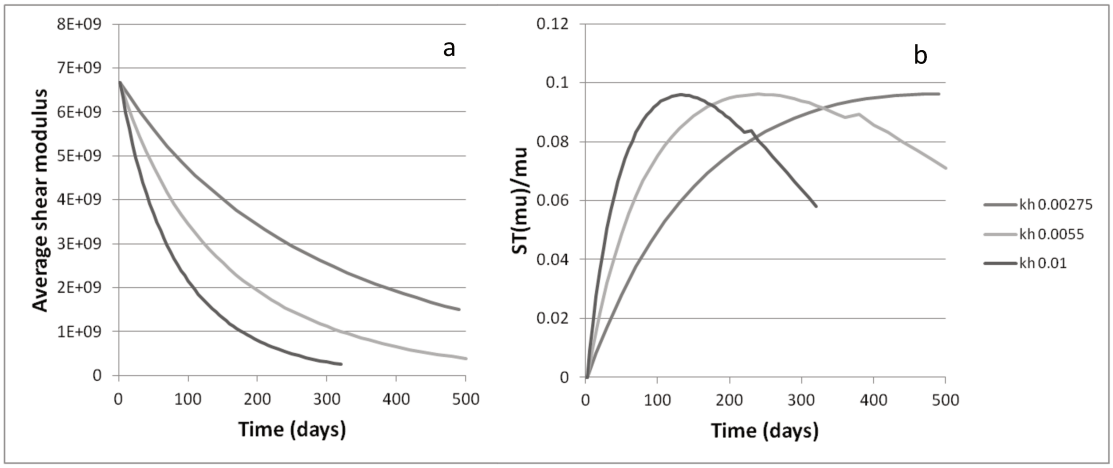

Figure 2.22: Influence on the rate of hydrolysis k_h on the evolution of the average value of shear modulus (a) and the standard deviation of the shear modulus normalized by its average value (b).

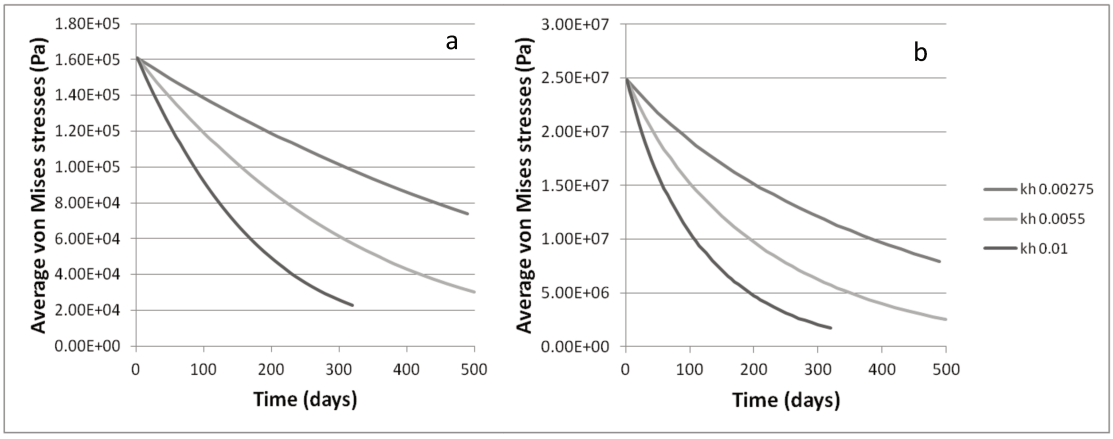

Figure 2.23: Influence on the rate of hydrolysis k_h on the stresses in the artery (a) and in the stent (b).

2.3.2.5 Influence of the shear modulus of the artery

The stiffer the artery, the sooner the stent loses its embedment in the arterial wall (Figure 2.17b). Furthermore, the stresses in the arterial wall (Figure 2.24a) and in the stent (Figure 2.24b) exhibit similar behaviors: the weaker the stent, the less pronounced is the difference

between the three values of the stiffness of the arterial wall, until the stresses reach the same values at the end of degradation.

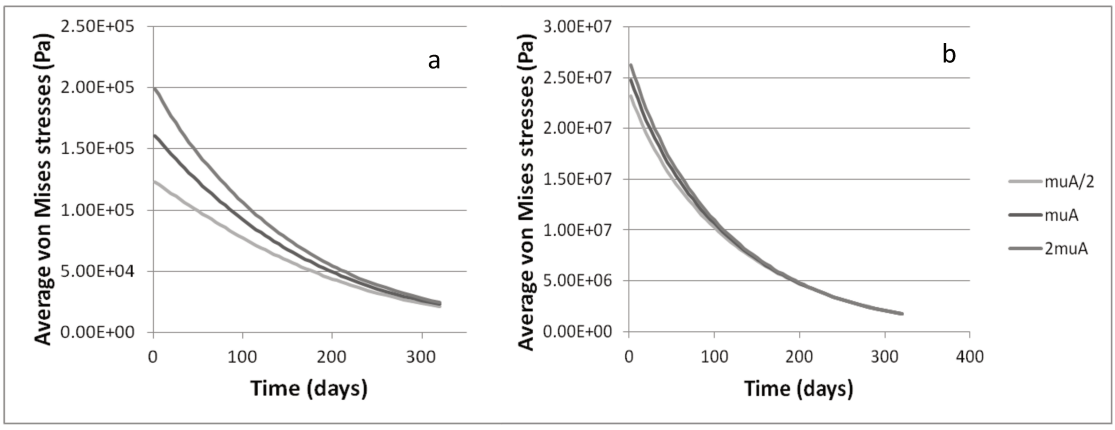

Figure 2.24: Influence of the shear modulus of the artery on the von Mises stresses in the artery (a) and in the stent (b) during the stent's degradation.

2.3.2.6 Influence of the threshold chosen for $k_l(load)$

Figure 2.25 shows the evolution of stent embedment, stent shear modulus and von Mises stresses within the stent and the artery for L_{max} varying from 10^6 to 10^{10} Pa. Not surprisingly, the decrease in the shear modulus, the embedment and in the stresses within both the stent and the arterial wall are generally larger and quicker when L_{max} is decreased. Indeed, reducing L_{max} means that less load is required to accelerate the degradation, and it thus increases the contribution of the load to stent degradation.

More precisely, it can be noted that there are two kinds of behaviors depending on whether L_{max} is larger or smaller than the average value of the stent stresses at the beginning of deployment ($2.5\ 10^7$ Pa). To improve clarity, the results for $L_{max} > 2.5\ 10^7\ Pa$ are shown in dots whereas when $L_{max} < 2.5\ 10^7\ Pa$, they are shown in lines. When $L_{max} < 2.5\ 10^7\ Pa$, the majority of the points has the same level of degradation – the maximum one k_l^{max} which is independent of L_{max} ; thus, during the first months of degradation, the average values of the stresses, the embedment and the shear modulus are very similar regardless of the value of L_{max} . For $L_{max} > 2.5\ 10^7\ Pa$, on the other hand, a larger L_{max} is associated with slower a decay. However, when $L_{max} < 2.5\ 10^7\ Pa$, the total range of variability between 0 and the threshold value L_{max} is reached, and thus the heterogeneity of the shear modulus is higher than when $L_{max} > 2.5\ 10^7\ Pa$, as shown in Figure 2.25e. Indeed, when $L_{max} > 2.5\ 10^7\ Pa$, the threshold value is so high that the points do not reach the total range of variability between 0 and L_{max} . To conclude, for $L_{max} < 2.5\ 10^7\ Pa$, the majority of the points have the same level of degradation, but for those that do not reach it, the heterogeneity is high since the total range of variability is available. Thus, they have similar average values whatever the exact value of L_{max} but exhibit more heterogeneity. On the other hand, for $L_{max} > 2.5\ 10^7\ Pa$, the majority of the points have different levels of degradation, but the

heterogeneity is not maximal because the total range of variability is not available. Thus, they have different average values but less heterogeneity.

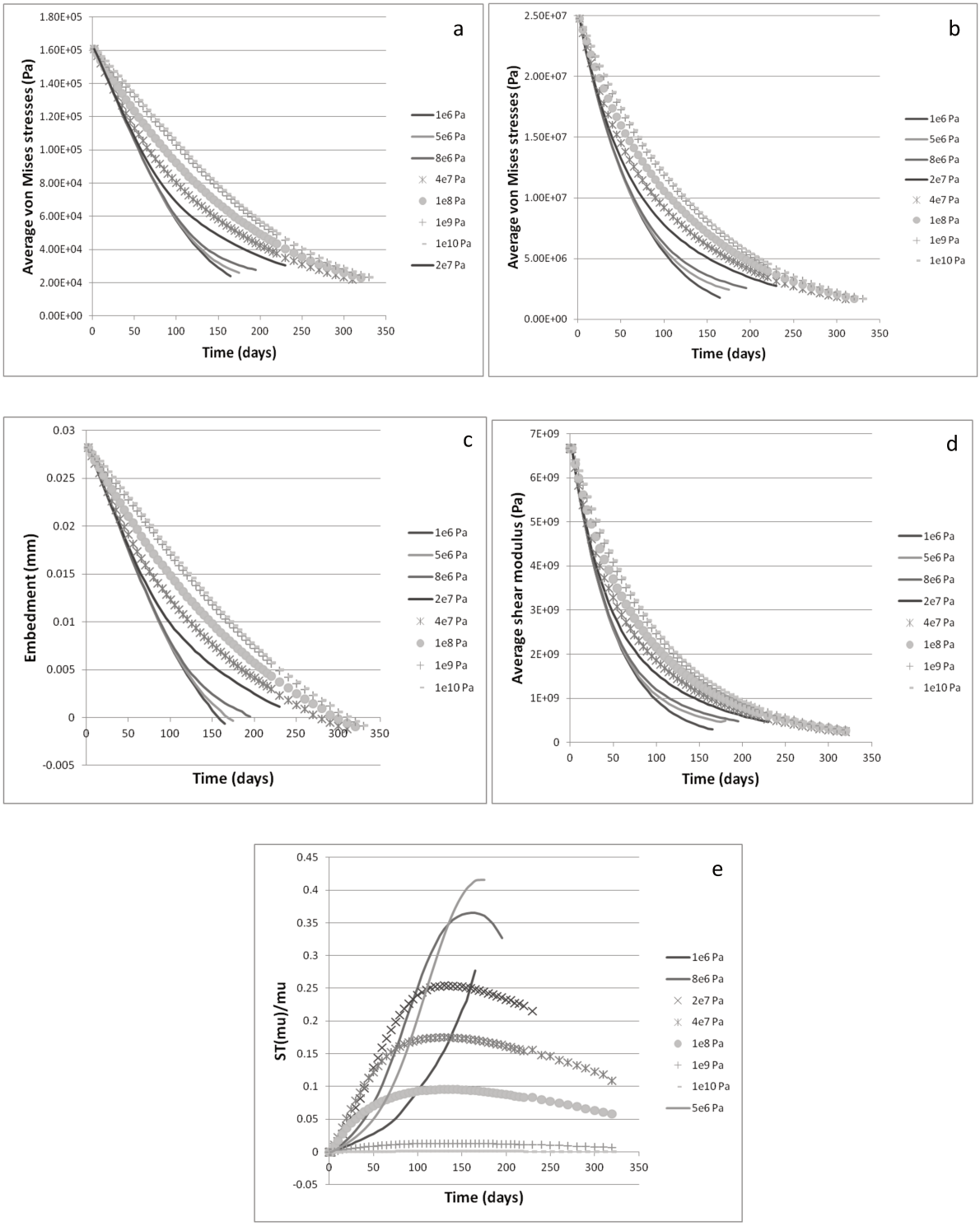

Figure 2.25: Influence of the chosen L_{max} on the average von Mises stresses in the artery (a) and in the stent (b), on the embedment (c), on the average shear modulus (d) and on the standard deviation of the shear modulus normalized by the shear modulus (e).

2.3.3 Arterial remodeling : idealized case

2.3.3.1 Arterial remodeling due to loss of ECs and to inflammation

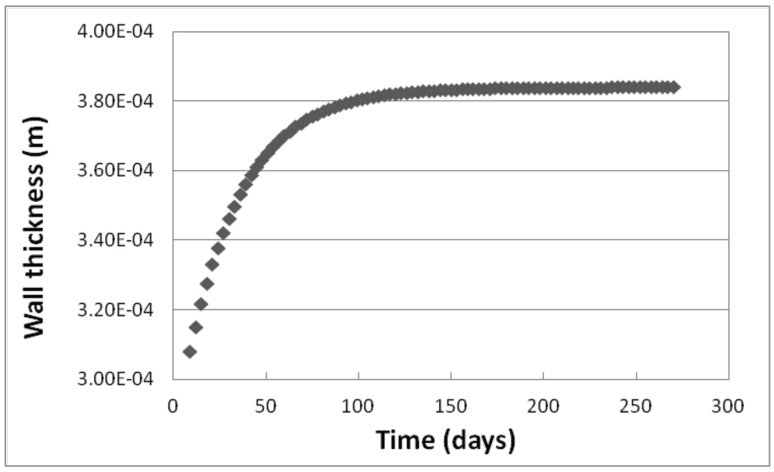

Figure 2.26: Idealized case: arterial remodeling due to the loss of endothelial cells: evolution of the wall thickness with time.

We begin by exploring the separate effects of EC denudation and inflammation on arterial wall remodeling. In the case of complete loss of ECs in the stented zone, the thickness of the arterial wall increases until reaching a plateau value which corresponds to the time when the wound is healed, as shown in Figure 2.26. In the case of inflammation, the arterial wall is thickest when the inflammation is maximal (Figure 2.27). This period is likely to correspond to the stent degradation because the degradation products are expected to elicit vascular inflammation.

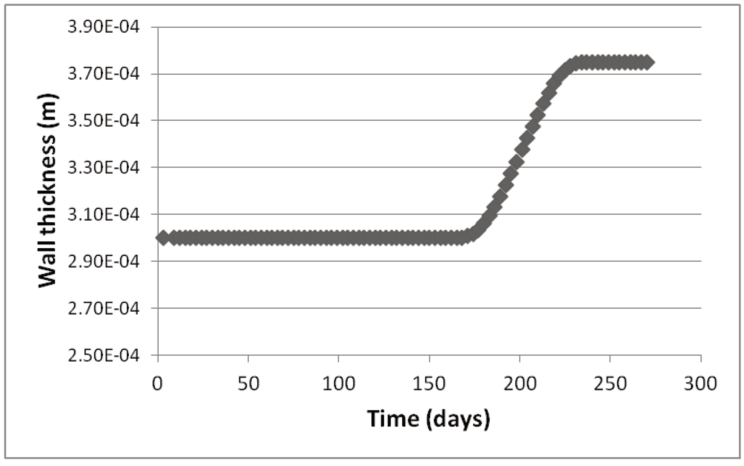

Figure 2.27: Idealized case: arterial remodeling due to inflammation: evolution of the wall thickness with time.

2.3.3.2 *Arterial remodeling due to hoop stress*

When we consider the contribution of only the stresses in the arterial wall, we observe that the arterial thickness first increases, reaches a peak of 450 µm at 100 days, and then decreases continuously (Figure 2.28B). The von Mises stresses decrease, reach a minimum below the homeostatic value, and then increase slightly and tend to the homeostatic value (Figure 2.28A).

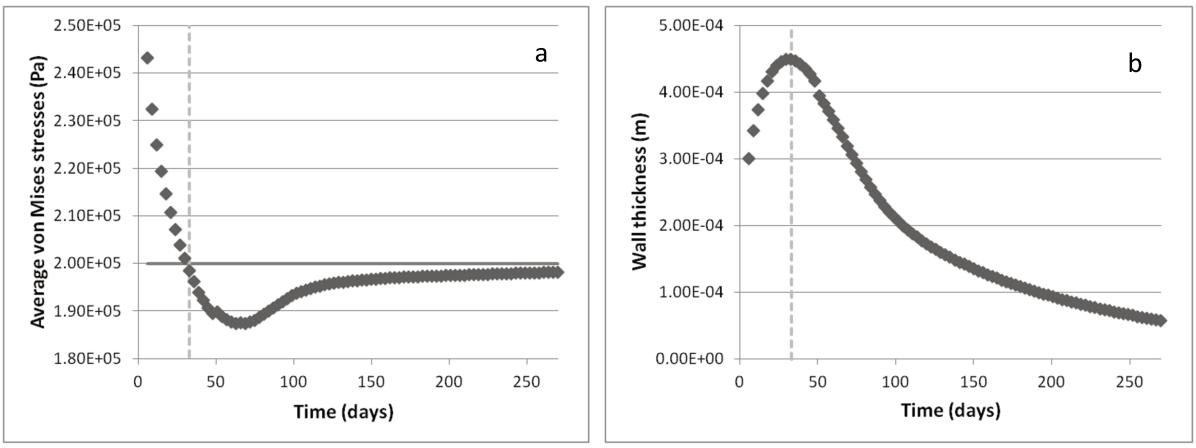

Figure 2.28: Idealized case: arterial remodeling induced by the experienced stresses. a: Average von Mises stresses at the inside wall of the artery. b: evolution of the wall thickness. Dash gray line: time at which the homeostatic value of the hoop stress is reached. Solid gray line: homeostatic value for the hoop stress.

In fact, the experienced von Mises stresses are initially higher than the homeostatic stress. To restore homeostatic values of the stresses, the arterial wall thickens. At ~35 days (marked with a dash line in the figures), the stresses reach the homeostatic value σ_0, and the arterial thickness is maximal. However, from that time point onward, the stent continues to degrade and thus induces progressively lower stresses within the arterial wall; that is why the observed stresses decrease below the homeostatic values. The artery thus reacts by decreasing its thickness, with the aim of restoring the homeostatic value. From around 150 days onward, an equilibrium is reached, where to maintain $\sigma = \sigma_0$ constant while the stent degrades, the artery constantly decreases its thickness.

2.3.3.3 *Combination of three contributions*

When the three factors that contribute to wall remodeling are combined, the results are largely similar to what was observed in the previous section, namely the arterial stresses decrease, reach a minimum below the homeostatic stresses, then globally increase to ultimately tend to σ_0 (Figure 2.29a). Between 150 and 200 days the stresses exhibit a decrease which corresponds to the period where the inflammation is maximal and thus thickens the arterial wall, leading to this observed drop for the stresses. The wall thickness (Figure 2.29b) also evolves similarly to the previous section; exhibiting a marked increase and subsequent decrease with time.

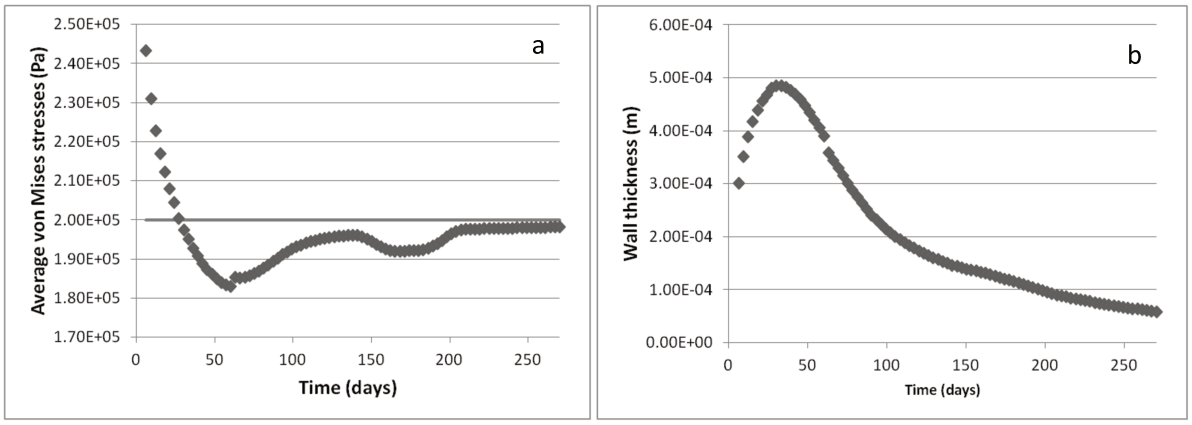

Figure 2.29: Idealized case: arterial remodeling induced by stresses, inflammation and loss of endothelial cells. a: Average von Mises stresses at the inside wall of the artery. b: evolution of the wall thickness. Solid gray line: homeostatic value for the hoop stress.

2.3.4 Arterial wall remodeling: parameters from literature

2.3.4.1 Arterial wall remodeling due to loss of ECs and due to inflammation

The remodeling due to the loss of ECs leads to an increase in wall thickness (Figure 2.30a) and a decrease in the average von Mises stresses on the inner surface of the arterial wall (Figure 2.30b). The initial number of cells has a pronounced impact on the final hyperplasia, thus underscoring the idea that a procedure that limits the arterial wound and more specifically endothelial denudation would be expected to lower the incidence of restenosis. Figure 2.31 shows the evolution of the wall thickness due to inflammation alone. As expected, the rate of wall thickening increases with the extent of inflammation.

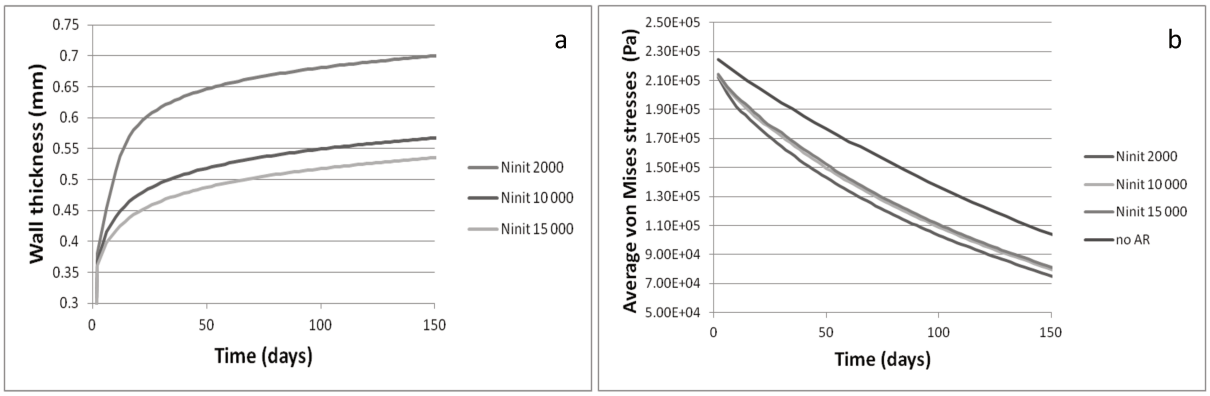

Figure 2.30: Wall thickness (a) and stresses at the inner surface of the artery (b) for different initial numbers of endothelial cells.

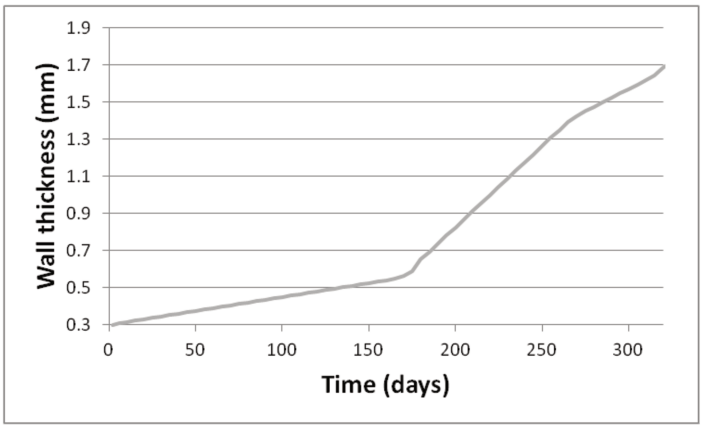

Figure 2.31: arterial remodeling and inflammation: evolution of the wall thickness with time.

2.3.4.2 Arterial wall remodeling due to hoop stress

As shown in Figure 2.32 and similarly to what has been observed in the idealized case, the experienced stresses decrease below the homeostatic value of the hoop stress. However, they do not increase again. In the idealized case the stent degrades slower, the homeostatic value σ_0 is higher, as is the allowed amount of remodeling per stress A_1'. It may thus be easier for the artery to adapt to the modified stresses, and this may explain the fact that the stresses in this case do not reach the target homeostatic value. The wall thickness (Figure 2.33) exhibits a similar shape to that in the idealized case with an increase and subsequent decrease when the homeostatic value is reached. As expected, the lower the value of σ_0, the earlier the stresses reach the target value and the earlier the maximal value of the wall thickness is attained.

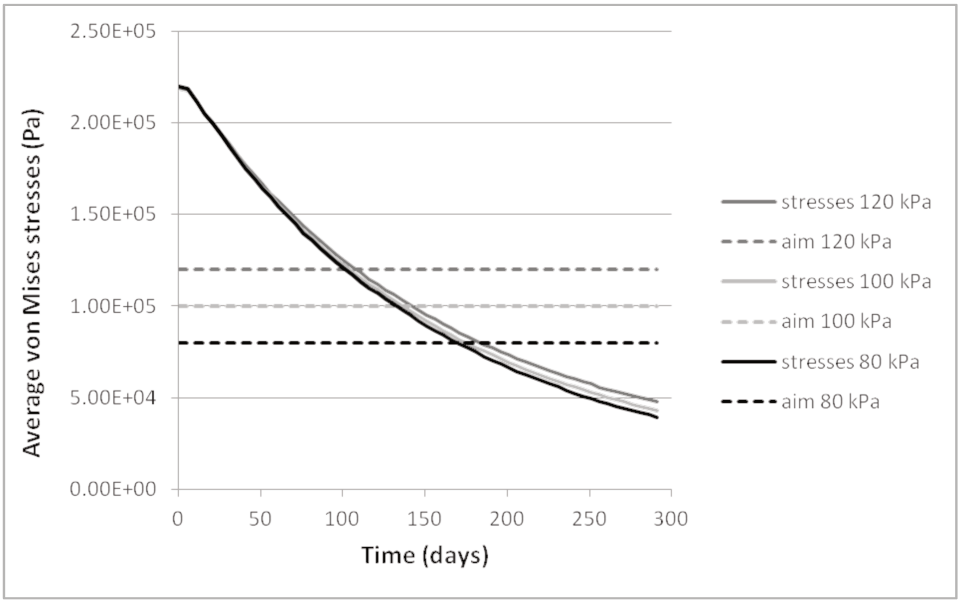

Figure 2.32: Arterial remodeling due to hoop stresses: evolution of the average von Mises stresses at the inner wall of the artery for different value of σ_0 – the dash line corresponds to σ_0 for the stresses of the same color.

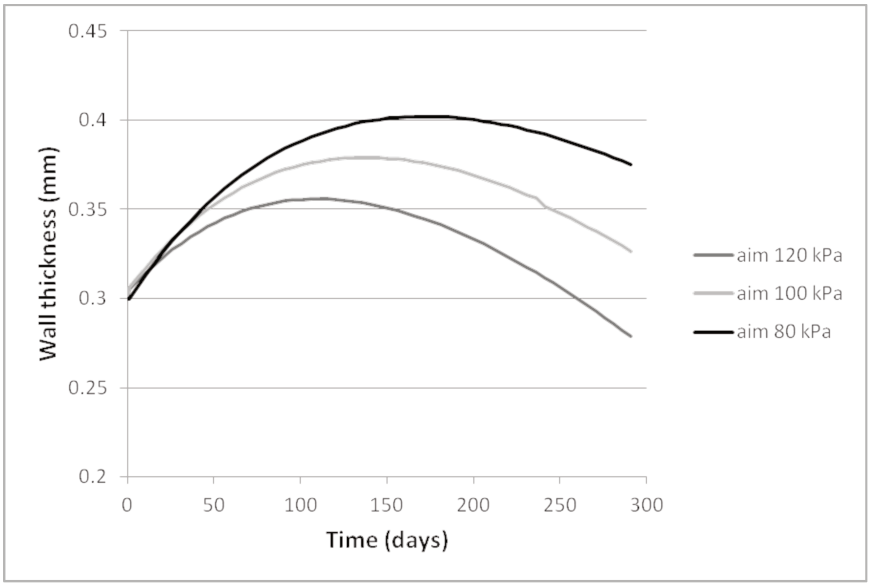

Figure 2.33 : Arterial remodeling due to hoop stress: evolution of the arterial wall thickness for different values of σ_0.

2.3.4.3 Combination of the three contributions

The evolution of average von Mises stresses and of the wall thickness for the combination of the three contributions is shown in Figure 2.34a and Figure 2.34b, respectively. The stresses decrease continuously whereas the arterial thickness increases continuously. While the idealized case was dominated by the contribution of the stresses to the arterial remodeling, here the role of the inflammation is quite important.

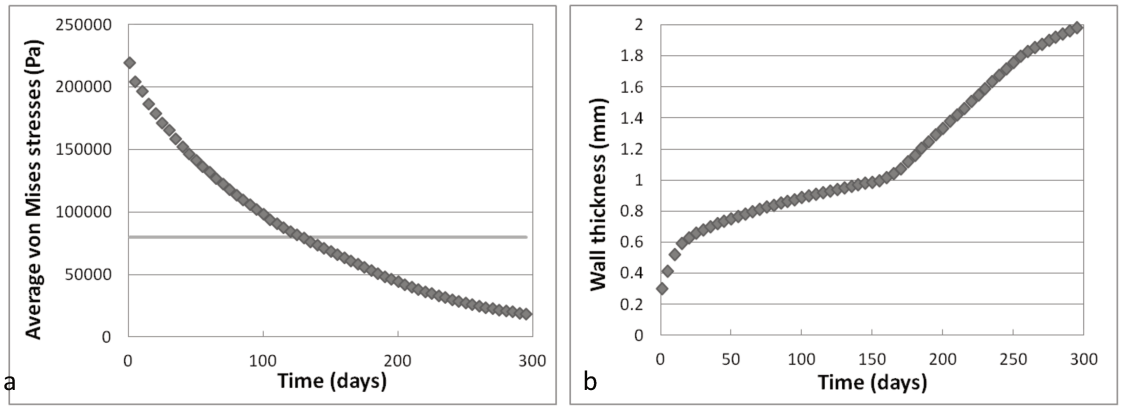

Figure 2.34: Arterial remodeling induced by stresses, inflammation and loss of endothelial cells. a: Average von Mises stresses at the inside wall of the artery. b: evolution of the wall thickness. Solid gray line: homeostatic value for the hoop stress.

2.4 Discussion

BRS are more and more used by surgeons. For instance, at least 150,000 Abbott BVS have been implanted in patients until now; the ART PBS has recently acquired the CE mark; and many others designs are currently undergoing clinical tests. Besides, accurate theoretical and computational models are needed to better improve BRS design and properties.

It is known that a stent injures the artery during its deployment and modifies permanently the mechanical environment of the vessel. On the other hand, arteries are living materials able to dynamically react and adapt to this perturbation. In the case of a BRS, this perturbation is varying with time because of the degradation of the stent, which leads to a modification of the mechanical properties and so, a modification of not only the stresses induced within the arterial wall but also on the ability of the device to maintain the diseased vessel open. Furthermore, the degradation of the sent is accelerated by the experienced load, both due to residual stresses and also to the artery-induced stresses. Thus, the coupling between a bioresorbable stent and artery during both deployment and degradation is complex and its understanding is crucial to predict the efficacy of the implanted device. Historically, BRS safety and efficacy were first studied using experimental trial and error works. Accurate computational models can be a great help to better understand the behavior of BRS.

We developed a model of the coupling between a BRS and an artery during both deployment and degradation. The stent is first submitted to a pressure calculated so as to reach a desired final radius. After elastic recoil, the stent is only submitted to the average blood pressure. During the second step of the model, with respect to the degradation of the stent and the biological response of the artery, the stent experiences two kinds of stress: the residual stresses due to plastic deformation and the stresses induced by the artery. Its degradation, primarily induced by hydrolysis, is accelerated by those experienced stresses. The degradation of the stent is theoretically modeled as a progressive decay of its mechanical properties taking into account hydrolysis and load. The inserted device thus submits the artery to a varying mechanical environment. The artery reacts to this by adapting its geometric wall thickness in order to maintain the experienced hoop stress constant to a homeostatic value. Two other important phenomena also contribute to the thickening of the arterial wall. First the loss of ECs – who usually control SMCs and maintain them in their contractile phenotype – leads to uncontrolled proliferation of SMCs and so to the thickening of the wall. Second, the inflammation induced both by stent-related injury and degradation of BRS induces cell proliferation. Most values for the parameters of our model are determined either from literature analysis – as it is the case for A_1, A_2, A_3, L_{max}, k_l^{max}, N_{EC}, k_i, k_d – or from experiments *in vitro* or *in vivo* in pigs conducted by a group we collaborate with – as it is the case for k_h, $f(t)$.

The first step of our model studies the deployment of a stent within an artery. Dogboning and foreshortening are observed during this phase, as it was in previous works[42,44,45] as well as during the *in vivo* deployment of BRS. The areas of the stent submitted to the higher stresses are the struts' intersections[44], and the areas submitted to the higher stresses remain the

same during both deployment and degradation. The stent experiences a recoil of ~5 % which is comparable with *in vivo* values for BRS recoil[30]. As discussed previously, the final embedment is ~30 µm which is less than the *in vivo* observed embedment – around 150 to 200 µm. An increase in the stiffness of the arterial wall leads to greater wall stresses, as previously highlighted by Timmins *et al.*[48]. However, they demonstrated that the stiffness of the plaque did not have an influence on the final radius of the artery, whereas in our model it has an impact on the embedment, even if moderate. In their study, they considered two designs of BMS stents having low and high radial rigidity[46], and plaque whose stiffness varies between half and twice the rigidity of the artery. The artery is over inflated to reach a final radius superior to the radius of a deployed stent, the stent is then translated into the lumen and the arterial wall is subsequently deflated upon the stent until reaching diastolic blood pressure. Thus, the elastic recoil of the stent may not be modeled using this method, and that might explain the observed differences regarding the final radius of the artery. Furthermore, BMS stents are stiffer than BRS stents and so their recoil will be less important; the stiffness of the artery thereby has a smaller impact on the final embedment.

Degradation is modeled here as a progressive decay of mechanical properties of the stent. Previous authors have modeled the evolution of mechanical properties of PLA with degradation[115]. In their work, Soares *et al.*[54] developed a theoretical material model of the degradation of PLLA fibers based on load driven degradation only, as Rajagopal *et al.* did previously more generally for polymeric material[78]. They wrote:

$$\mu = \mu_0(1 - d) \tag{2.33}$$

With:

$$\frac{\partial d}{\partial t} = C(1 - d)[(I_1 - 3)^2 + (I_2 - 3)^2]^{1/2} \tag{2.34}$$

With C a constant and I_1 and I_2 the first and the second invariants of the right Cauchy-Green deformation tensor. Thus the rate of hydrolysis depends both on the amount of degradation and the state of deformation. Nevertheless, in this type of formulation, there is no degradation in an undeformed state. Thereafter, Soares and co authors used more complex hyperelastic laws such as the Knowles' model[53,116], a generalization of the neo-Hookean law. They found it to more accurately describe the behavior of PLA than simple neo-Hookean law. These models were also based on load driven degradation. Although load is known to accelerate the degradation of the polymers, and may even provoke a reaction by itself in some cases[80]; this model would not fully reflect what happens experimentally since hydrolysis alone can also lead to the degradation of PLA fibers. That is why we chose to model the degradation of the stent by another method. We started from equation (2.11) defined by Soares *et al.*, but we used the definition given by Vieira *et al.* for the definition of the damage parameter. Their definition is based on a theoretical model of the chemical degradation experimentally justified[49]. Lacking precise experimental data on the influence of the load, we chose to model it with a simple linear dependency on load for the kinetic rate of hydrolysis. We obtained a material model taking into account both hydrolysis and load induced degradation.

Whereas the hydrolysis driven degradation induces a homogeneous variation of these properties within the stent[49], taking into account the acceleration due to load induces a spatially heterogeneous degradation of the material, as highlighted previously in the works of Soares *et al.*[35,55] and Debusschere *et al.*[56]. The zones experiencing the higher stresses degrade faster, and are thus very likely to be the breaking zones of the dismantling stent[35,55]. We also showed that the heterogeneity of the mechanical properties increases during the first months of degradation, and then decreases. This is due to the fact that accelerated degradation of the zones experiencing the highest stresses not only leads to the decay of mechanical properties but also to a decrease of the experienced stresses; as a result this secondarily drives to a homogenization of mechanical properties of the stent.

The internal radius of the stent decreases by ~2 % during degradation. A weaker stent seems to be less able to withstand the arterial wall. Soares *et al.*[55] found similar results for polymeric degrading stents submitted to a constant inward pressure of 1 atm. The amount of recoil varied according to the considered stent design, ranging from ~7 to ~42 % in their study. Thereby, our results are qualitatively coherent with previous works but the quantitative values differ. This may be due to the different design we used, but also to the stresses we considered: they used a constant inward pressure applied on the stent whereas in our model the stent is submitted to the residual stresses due to plastic deformation, to the stresses induced by the arterial wall and to the average blood pressure. The coupling between a BRS and an artery as modeled here – and also used by Debusschere and co workers to model the degradation of a metallic biocorrodible stent[56] – may be an interesting tool to more realistically model the stresses the stent is submitted to.

An increased rate of hydrolysis accelerates the degradation in an important way, which is likely to lead to an earlier dismantling and potential late lumen gain. Indeed, ART PBS degrades faster than both design of BVS and *in vivo* studies show a positive remodeling appearing between three to six months[30] whereas an increase in lumen diameter was shown between 2 and 5 years for BVS 1.0[31].

To our knowledge, arterial remodeling has not been taken into account previously in computational models describing the stent deployment and degradation. Here we proposed a first model of arterial remodeling taking into account the hoop stresses experienced by the artery, the injury caused by the stent during the deployment, and the inflammation both induced by the injury and the degradation of the stent. We first presented the results of an idealized case, then achieved a literature analysis to determine more accurate values for our model parameters and present the results hence obtained. In the idealized case, focusing first on the stresses induced remodeling, one can observe that the artery thickens to restore a homeostatic value for the experienced stresses, stops its hyperplasia when the aimed value of stresses is reached, then faces a decrease in the stresses induced by the degrading stent, and subsequently thins to reach the homeostatic value. When the three contributions are combined, this evolution with an increase in wall thickness and a secondarily decrease is also observed. This evolution is strikingly similar to what is observed *in vivo*. For instance, in *in vivo* studies conducted in pigs stented with ART BRS, Durand *et al.*[30] have shown that the neointimal hyperplasia reached a peak between 3 and 6 months and then decreased. Our

model thus seems to give results qualitatively coherent with what happens *in vivo* for the first step of arterial remodeling. However, in a second step, one would note that the modeled thickness of the artery reaches values thinner that at the beginning of degradation, which does not happen *in vivo*. Nevertheless, from that point, others phenomena not taken into account in this study will happen and are likely to become predominant and thus modifying the evolution of the stresses and the wall thickness; such as the embedment of the struts in the arterial wall and the dismantling of the stent. Besides, the values of the different contributions are not accurately determined in this idealized model.

Thereafter, we presented the results obtained for parameters directly deduced from literature experiments. The results for the contribution of hoop stress were at first similar to the idealized case with the stresses exhibiting a decrease below the aimed value and the artery exhibiting the typical increase and subsequent decrease in thickness. However, the stresses do not yet eventually tend to the aimed value. Considering the three contributions of the arterial remodeling leads to continuously decreasing stresses and an increasing thickness which reaches non physiological values (eight times the initial values of the wall thickness). We saw that the inflammation was here the predominant contribution. This may be questionable. Indeed, the effect of inflammation may be indirectly partly taken into account by the contribution of the absence of ECs, since it is due to an injury and thus associated with inflammation. Moreover, the cells could also be expected to adapt to permanent levels of inflammation and may exhibit decreasing rates of proliferation if submitted to constant rate of inflammation. Thus, too high an influence given to the contribution of inflammation may explain the non physiological behavior thus obtained from those simulations combining the three contributions.

Thereby, the model shows here strong dependence upon the values of the different parameters. The experiments from which values were extracted seem not sufficient to accurately determine them. The model would therefore benefit from tailored experiments. However, the evolution of the wall thickness which increases and subsequently decreases is observed firstly in the idealized case and secondly when considering the contribution of the stresses in the literature base case, and is qualitatively similar to experimental data. This suggests that modeling the arterial remodeling with accurate biological parameters may be helpful to forecast the evolution of arterial thickness for a given stent and to design BRS inducing as low as possible a neointimal hyperplasia.

We therefore developed in this study a model of the complex coupling between BRS and artery during both the deployment and the degradation of the stent; on the one hand the artery submits the stent to stresses which accelerates its degradation, and on the other hand the stent submits the artery to varying stresses inducing remodeling. Some limitations and improvements can be pointed out.

Firstly, some parameters of our model are extracted from experiments on pigs, as well as the validation of the computational results made thanks to experimental porcine data. Even if those data need to be validated in humans, it is a good first approximation since pigs have been shown to be a good model to study angioplasty and stenting procedures[117].

Secondly, the model could be improved by taking into account more accurate geometrical and mechanical features for stent and artery. Regarding the geometry, the design of the stent could be adapted to the last generation of stent showing an open cell design instead of a close cell design; and a three layer model could be considered for the arterial wall, with a separate plaque.

Vieira and co workers experimentally studied the mechanical properties of degrading PLA-PCL fibers, and the accuracy of different hyperelastic material laws to describe their behavior. They showed that although neo-Hookean law was reasonably satisfying in describing mechanical properties, other models such as the Mooney-Rivlin and the second reduced order model showed better accuracy[49]. Hayman *et al.* used the Knowles model, a generalization of the neo-Hookean law[53]. As a result, even if a simple law such as the neo-Hookean one seems a reasonable choice for a first approach, more complex laws could be implemented in further studies to describe more accurately the non linear elastic behavior of polylactic acid. Furthermore, the viscoelasticity of PLA has been shown[118,119] and could also be taken into account. It is for instance possible to use models adapted from the Bergström and Boyce constitutive model used by Vieira *et al.* to describe the evolution of PLA-PCL fibers' mechanical properties during *in vitro* degradation[120] and by Debusschere *et al*. for a numerical implicit method of BRS deployment[121]. Eventually, models accounting for PLA anisotropy[122] could also be implemented. Besides, the stent crimping could be taken into account. As far as the artery is concerned, an anisotropic model as the one developed by Holzapfel[11] could be implemented to study the influence of the orientation of collagen fibers. Moreover, to be more realistic, one could model the artery as prestressed and take into account the stresses induced by the pulsatility of the blood flow.

Thirdly, the balloon is not directly modeled in our study. Nevertheless, Gervaso *et al*.[45] compared three methods of stent deployment – a prescribed displacement, a constant pressure, and an inflating balloon – and concluded that the differences between the three methods were mainly due to the dogboning effect being shown only with their third method. As a result, methods enabling to represent the dogboning phenomenon should be preferred. Thus, even if there is no physical balloon in our study, our model which calculates at each time step the pressure needed to follow the radius of an inflating balloon and which clearly shows a dogboning effect can be consider as sufficiently realistic.

Fourthly, as far as the parameters of our theoretical model are concerned, as mentioned previously it is very difficult and sometimes even impossible to define their exact values from literature. Now, the degradation dynamics are very sensitive to the composition of the stent polymer. This model would benefit from more detailed experiments on the degradation dynamics of the polymeric stent to complement the behavior assumed in the present study. Similarly, the model of the arterial remodeling and the weight of the different contributions would benefit from experiments comparing them for the same stent in the same animal model.

Fifthly, to model the chemical degradation, it was assumed that the concentration of the ester groups was constant compared to the concentration of carboxyl end groups, which is

rather exact during the first stages of degradation but not at the end of it since the hydrolytic degradation of the polymer leads to an increase in carboxyl end groups and scission of the ester groups. Our model of the stent degradation is then likely to be less valid and less precise by the end of degradation. However, as it can be observed from the experimental evolution of M_n, and as it will be seen in the next chapter, an exponential shape is of good agreement with the experimental data to model the evolution of PLA's properties during degradation.

Lastly, a crucial phenomenon which could be implemented in further studies is the dismantling of the stent. Indeed, at some point the stent is going to break. The weaker parts where the stent is likely to dismantle can be deduced from the analysis of the von Mises stresses experienced by the stent and the study of the shear modulus[55]. The pieces of the stent remaining embedded in the arterial wall will prevent it from collapsing, but will allow potential positive remodeling. Indeed, the artery is able to adapt its geometrical properties to maintain a homeostatic value for the hoop stress, but also for the shear stress. It is known that arteries modify their lumen diameter in order to maintain wall shear stress constant[102,123]. With a metallic stent, the artery is caged by the device and it is not able to adapt to a modified shear stress. When the dismantling of the BRS occurs, the artery is not caged anymore, and can adapt its lumen diameter in order to restore the experienced shear stress to a homeostatic value; or to decrease the compliance mismatch between the diameters of the stented part and of the unstented part of the artery, since this also induces variations of shear stresses. *In vivo* studies show evidence of this positive remodeling with BRS and late lumen[30,31]. Associated with stent dismantling, further studies could take into account the ability of the artery to adapt its geometry to modified shear stress.

CHAPTER 3

Optical Coherence Tomography Following of the Degradation of Three Different Stents

3.1 Introduction

Today, stent deployment is the most common treatment for symptomatic atherosclerosis[59]. Bioresorbable stents (BRS) are based on the premise that a stent is needed only until arterial wound healing occurs after which it would be desirable for the stent to degrade so that the arterial wall recovers its natural compliance. BRS present several advantages. Firstly, contrary to conventional stents such as drug-eluting stents, the risk of long term thrombosis is expected to be reduced due to the absence in the long term of foreign material in the body. Consequently, the need for long term anti platelet therapy would also be reduced. Secondly, because BRS struts dismantle beyond a threshold level of degradation, the artery will no longer be caged which opens the possibility for positive remodeling of the vessel wall and associated late lumen gain[30,31] as well as for the progressive disappearance of the compliance mismatch between the stented and unstented segments of the artery. Thirdly, when the stent is fully degraded, the physiological vasomotion of the artery in response to pulsatile blood flow is expected to be restored. Finally, BRS degradation allows future treatment of the same arterial area and eliminates artifacts during thoracic imaging. For all the above reasons, BRS are considered as very promising devices in the field of interventional cardiology[29].

Since the first implantation in humans of the Igaki-Tamai BRS in 1998[33], different designs and materials have been developed and tested in pre-clinical and clinical studies[39,40]. Existing BRS exhibit widely different degradation characteristics, most notably in terms of the speed of degradation. For instance, whereas the commercially available version of Biodegradable Vascular Stent (BVS) of Abbott Vascular, the first BRS to be available on the market, shows similar appearance on optical coherence tomography technique between 6 and 24 months[62], the Pure Bioresorbable Scaffold (PBS) developed by Arterial Remodeling Technologies (ART) degrades in less than two years. These differences are present although both stents are made of polylactic acid (PLA), a bioabsorbable polymer widely used in the medical field. Indeed, the

degradation speed of PLA can be tuned by adjusting various chemical properties of the polymer, such as the rate of crystalinity or the ratio of the enantiomers[70]. Although the dismantling and the disappearance of the stent is desirable to allow for positive remodeling and facilitate vasomotion, exceedingly rapid degradation can also provoke the failure of the device's ability to provide a stable scaffold for the artery during its healing period. A prominent example of such a failure is the first design of the metallic (magnesium) biodegradable stent developed by Biotroniks which shows complete absorption at two months; the device failed to provide sufficient mechanical support to the arterial wall and thus led to very high rates of restenosis[41]. BRS are hence complex devices that need to provide sufficient support for the artery even as they mechanically weaken with degradation. As a result, contrary to the behavior of non degrading stents which can be fully determined only by achieving initial tests, it is crucial to understand and characterize the transient behavior of BRS since this behavior has a profound influence on BRS safety and efficacy.

With this aim, one needs methods to follow the stent degradation and modifications of its properties. *In vitro*, BRS degradation can be followed either by measuring chemical properties[81,124,125] such as the number average molecular weight or the rate of crystalinity or by testing mechanical properties such as the fracture strength or the elongation at rupture[125–127]. *In vivo*, stent degradation in animal studies can be followed using histology[61]. For clinical studies and evaluation of the behavior of BRS in patients with various diseases and co-morbidities, the only available methods are quantitative coronary angiography (QCA) and intra vascular imaging techniques such as intra vascular ultrasound (IVUS) and optical coherence tomography (OCT)[128]. QCA is one of the most commonly used techniques to assess the efficacy of a stent procedure, but it is primarily useful for providing geometrical parameters such as late lumen loss or gain and functional parameters such as vasomotion. IVUS is commonly used in the study of atherosclerosis and deployed stents. It has a penetration depth of 10 mm, a lateral resolution of 100-200 μm and an axial resolution of 200-300 μm. OCT uses infrared light and rebuilds images thanks to the analysis of the interferences induced by back scattered light. Its penetration depth of 1 to 2.5 mm is less powerful than that of IVUS; however, it is more precise, allowing for a lateral resolution of 15-20 μm and an axial resolution of 20-40 μm[129]. OCT has the ability to confirm the presence or the absence of atherosclerosis and to accurately measure the luminal stenosis of the vessel, with results that are very likely to be more precise than those measured with QCA[129]. It is also a very useful technique for studying stents[130]. As such, it has been shown to be a good method for detecting uncovered stent struts[131–133], quantifying the amount of neointimal formation post stenting[134,135], and detecting neo-atherosclerosis[136]. Despite its limited penetration depth compared to IVUS, OCT's accuracy renders it a very versatile technique for assessing stent behavior.

Of particular relevance to the present study, OCT also allows following BRS degradation as strut appearance on OCT images changes considerably with time. A semi-quantitative method to track BRS degradation based on OCT images has previously been developed[137]. This method subdivides BRS struts into four stages of degradation: preserved box, open box, dissolved black box, and dissolved bright box, see an example in Figure 3.1. Thus, the percentage of struts in each of the four categories can be counted at each time point, which

gives an evaluation of the extent of degradation of a given BRS with time[30,36,61]. Although this semi-quantitative technique provides a very useful method for tracking stent degradation, it has a certain level of subjectivity because the user needs to make a judgment in the choice of categories. It is also very time-consuming.

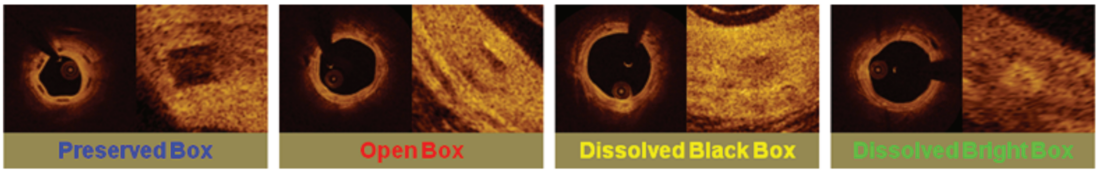

Figure 3.1: classification of the struts appearance in four stages for *in vivo* degradation

Besides, this classification based on BRS strut appearance and brightness suggests that the intensity of the struts on the OCT images provides a useful measure of the extent of BRS degradation. The current work thus aims to develop a quantitative method (rather than a semi quantitative one) to analyze stent's degradation based on the analysis of the stent's struts grey scale intensity (GSI) on OCT images. The developed algorithm automatically detects stent strut contours and quantitatively determines their GSI. To demonstrate the capabilities of this new method, we compare the *in vitro* degradation kinetics of two BRS: the Abbott BVS and the ART PBS.

3.2 Materials and methods

3.2.1 In vitro degradation of BVS and PBS

3.2.1.1 Stents and Experimental Setup

Three 18 mm-long and 150 μm thick Abbott BVS were used in the experiments. BVS consist of a poly(L-lactic) acid scaffold with an external layer of poly(D,L-lactic) acid which contains and releases the everolimus drug. ART provided three samples of each of two types of stents that have a length of 11 mm, the same design and chemical composition, but different strut thicknesses - 130 and 170 μm; these two stent types are henceforth respectively referred to as ART1 and ART2. ART stents are made of poly(D,L-lactic) acid without any coating. The difference in the rates of PLA enantiomers between BVS and PBS is believed to be primarily responsible for their different kinetics of degradation. One sample of each type of stent was deployed using a balloon catheter in accordance with the manufacturers' instruction in a tube made of a styrene-ethylene-butylene-styrene based thermoplastic elastomer (Cawiton Meb) with an inner diameter of 3.2 mm and a thickness of 200 μm, henceforth simply referred to as tube or tubing. As depicted in

Figure 3.2, each tube contained one of each type of stent (BVS, ART1, and ART2); three separate tubes were imaged. The tubes were in turn inserted into glass tubes filled with a saline solution of sodium chloride at 0.9 % and maintained at 37°C in a water bath. The saline solution and glass tubes were changed at each image acquisition.

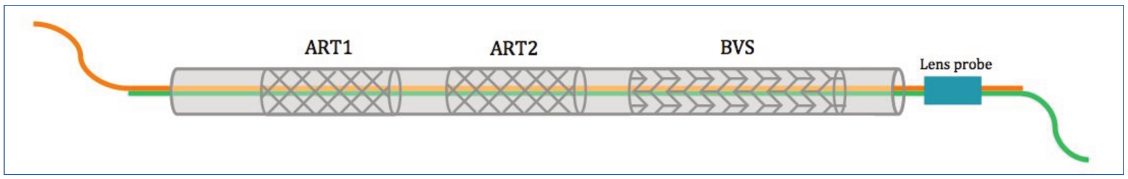

Figure 3.2: Schematic of the setting of the experiments, showing the three stents deployed in the soft plastic tube, the metallic guide (in orange) and the OCT catheter (in green).

We note that the stent degradation in the present study occurs in the absence of flow. Mechanical loading is known to accelerate the degradation of polylactic acid[53]; thus, flow-induced shear stress may have an influence on the kinetics of the reaction. However, physiological levels of shear stress are much smaller than the other mechanical stresses that are taken into account, namely the residual stresses in the stents due to the plastic deformation occurring during deployment and the stresses induced by the tube into which the stents are deployed. Another potential effect of flow is to remove the degradation products of the reaction and so increase the speed of degradation. However, *in vitro* polymeric degradation in the absence of flow has previously been validated against the *in vivo* situation and has been shown to provide an accurate model for the evolution of the number average molecular weight of the polymer[125]. Based on the above arguments, we consider the impact of flow on the kinetics of degradation to be negligible.

3.2.1.2 OCT imaging

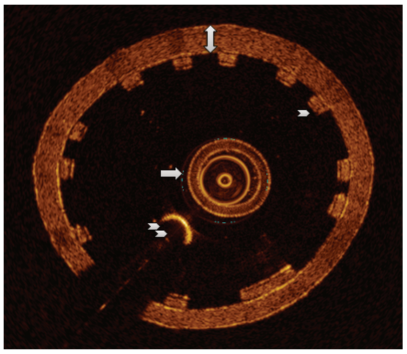

Figure 3.3: Example of the obtained images: an axial section of ART1 at four months. The arrow indicates the acquisition probe; the double arrow the plastic tube in which the stent is deployed; the single arrow head a strut of the stent; the double arrow heads the metallic guide.

OCT images were acquired using the C7-XR™ OCT intravascular imaging system (St. Jude Medical, St. Paul, MN, USA). To perform the imaging, a metallic guide wire (Hi-Torque Balance Middleweight Guide Wire, Abbott; in orange in Figure 3.2) is first inserted into the tube, and the acquisition probe (C7 Dragonfly™, Dragonfly™ Duo, or Dragonfly™ OPTIS™ Imaging catheters, St. Jude Medical; in green in Figure 3.2) is then inserted driven by the metallic guide. The tubes are thus rewired at each image acquisition. The OCT system is then prepared and calibrated according to the instructions for use (IFU) of the manufacturer. OCT is performed the day of deployment, once a week during one month, once every fortnight during one month and once a month until 24 months of follow up (expect for December 2014 due to experimental issues). One acquisition for a stent is a sequence of axial sections separated by 200 µm, which leads to around 60 images for each of the six ART stents and

around 90 images for each of the three Abbott stents. An example of the obtained images is shown in Figure 3.3. Several acquisitions are achieved for each tube and then the best one is chosen for each stent.

3.2.2 Image analysis: creation of a mask

The goal of this section is to develop a validated method to automate the detection of BRS struts from OCT images and to use this detection to track the evolution of strut intensity as the stent degrades. The method creates a mask that only retains the struts on the images. The program is used to analyze sequences of images in which the average gray scale intensity (GSI) of the struts is calculated for each image. To develop this method, we collaborated with researchers from the laboratory of applied mathematics of Ecole Polytechnique (CMAP), and more especially, with Pauline Tan. She developed the code on Matlab and we tailored the method together. The following describes its principal elements.

We first need to mention a particularity of the TIFF format used here by St. Jude Medical. This format is constituted of matrices of grayscale values associated with a color code for the display of the image. This means that the image *appears* colored – with the gold display seen in previous figures – but those colors do not correspond to something real, it only improves the visual rendering. Moreover, if one measures the intensity of a given pixel with ImageJ for instance, one would obtain gray scale intensity value. Similarly, if the image is open as a matrix of pixels and displayed thanks to Matlab it would appear "black and white" since Matlab would consider only the matrix of GSI and not the color code for display. That is why the figures of this section appear black and white, with no information lost compared to the golden images.

On the images are visible the plastic tube and the stent's struts. Both have similar intensities, bright compared to the dark background. Thus, to detect the struts, simple use of thresholding methods is not sufficient since it would not discriminate the struts from the tube. As a result, the method is held in two steps: it first aims to remove the tube and secondly to increase the contrast between the struts and the background. The whole method is summarized at the end of the subsection on Figure 3.5.

3.2.2.1 Removal of the tube

A. Detection of the outer edge

The outer edge is roughly circular but not entirely since the shadow of the catheter interrupts it. An appropriate method in this case is the geodesic active contour model[138] also called snakes. This method aims to detect the contour of an object knowing an initial guess for the sought shape. A positive potential W_i is associated with the image so that it is as small as possible along the sought contour. One then introduces an energy E, which depends on the potential W_i. The energy is defined for a given parameterized curve $\gamma(t)$, so that $E(\gamma)$ is small if $\gamma(t)$ lies in areas of small W_i. Thus, the aim is to compute the minimizer of E. E is first calculated along the parameterized curve γ_0 associated with the initial guess. The

parameterized curve γ(t) is step by step spatially modified with the goal of minimizing the calculated energy. Therefore, the curve is expected to eventually tend to the sought contour.

More explicitly, the energy *E* is defined as:

$$E(\gamma) = \int_0^1 W_i(\gamma(t)).\|\gamma'(t)\|.dt \tag{3.1}$$

E is minimized iteratively by the so called gradient descent method. γ is initialized as γ_0, *E* is calculated and at next iteration, the value of γ is updated by following the gradient direction, which is known to be the best way to decrease *E* and so to tend to its minimization. Thereby, the minimization process follows the above algorithm for a given number of iterations:

1. Initialize $\gamma \leftarrow \gamma_0$
2. Compute the gradient of *E* at γ, denote by $\nabla E(\gamma)$
3. Gradient descent: set $\gamma \leftarrow \gamma - \delta t \nabla E(\gamma)$
4. Go to 2.

The potential W_i has to be chosen so that it is as small as possible along the outer contour. As this contour is the border between a dark background and the bright tube, a potential based on the gradient of the intensity I is an appropriate choice. It thus has to be chosen as minimal when the gradient is maximal. With this aim, W_i is defined in function of the Gaussian kernel *G* of standard variation *σ*:

$$W_{i[I_{min},I_{max}]} = -aG * \left\| \overrightarrow{\nabla(\Pi_{[I_{min},I_{max}]}(I))} \right\| + b \tag{3.2}$$

Where a and b are two constants chosen so that W_i varies between 0.5 and 1; and $\Pi_{[I_{min},I_{max}]}$ the projection of I onto $[I_{min}, I_{max}]$ avoiding too big a gradient.

To reduce calculation time two detections were achieved: the first one is a coarse detection of the outer contour on a downsampled version of the image; the second one is realized on the real size image using the first detection as initial guess.

Eventually, a final roundish contour γ is obtained, which corresponds to the outer contour of the tube and extends it where it is interrupted by the shadow of the catheter.

B. Contrast correction

We noticed that the intensity depends on the distance to the catheter. To take this into account, a correction was applied to the image to facilitate further steps. Note that the correction applied here differs from the one determined experimentally in the next steps. The corrected intensity $\tilde{I}$ is given by:

$$\tilde{I}(P) = \Pi_{[0,1]}\left(\frac{1.8}{(1 - 0.05 * d_{cat}(P)/R)^{15}} I(P)\right) \tag{3.3}$$

for each pixel P of the image, where d_{cat} its distance to the catheter, I the non corrected intensity and R the stent radius estimated thanks to the outer contour detection.

C. Detection of the inner edge

To detect the inner edge of the tube, snakes method cannot be used since the struts and the tube have too similar an intensity, thus the potential based on intensity gradient will fail to detect the inner edge. Another approach was then used. First, points of the edge where there is no strut are detected and the tube's thickness is measured at those locations. Thereafter, based on the observed regularity of tube's thickness, the missing points are determined by interpolation and the total inner contour is eventually recovered.

C1. Initial detection

The centre C of the final contour γ is first determined as the barycentre of all points. For each point M of the outer contour, a stroke linking M and C is considered. We look for the point corresponding to M on the inner contour, denoted by M', which is the intersection between the inner contour and MC. The distance MM' gives the tube thickness at M. Then, the intensity is measured along the stroke MC. Since the tube's intensity is bright, the measured intensity is first high when the stroke is going through the tube. Thereafter, the intensity will eventually drop and be low when the stroke is going through the dark background. The point M'' where the maximal gradient is reached is stored. This is always true except for the points of the outer contour corresponding to the shadow of the catheter. To detect those points and eliminate them, the intensity *I(M)* is compared to a threshold value I_{shadow}. If $I(M) < I_{shadow}$, the point is rejected.

Three situations can be encountered regarding the evolution of *I* along MC and summarized in Figure 3.4:

1. The situation where there is no strut: the measured intensity exhibit a rectangular shape of the width of the tube, and M'' corresponds to M'.
2. The situation where there is a strut appearing as a white box: the measured intensity remains high and the point M' belongs to the segment MM'' with $|MM'| \sim |M'M''|$.
3. The situation where there is a strut appearing as a darker box outlined with white contours: the measured intensity will exhibit a drop when the stroke emerges the tube, and a second one when the stroke emerges the struts. As the strut even if dark is still usually brighter than the background, the second drop will be the maximal one and thus, the one corresponding to M''. Similarly to case 2, M' belongs to MM'' with $|MM'| \sim |M'M''|$.

As the tube thickness is rather constant, one can determine an estimation of the tube thickness d_{rough} and compare it to |MM''| to differentiate the points M'' corresponding to the inner contour with the points M'' corresponding to the edge of a strut. The points corresponding to the inner contour M' are thereby stored.

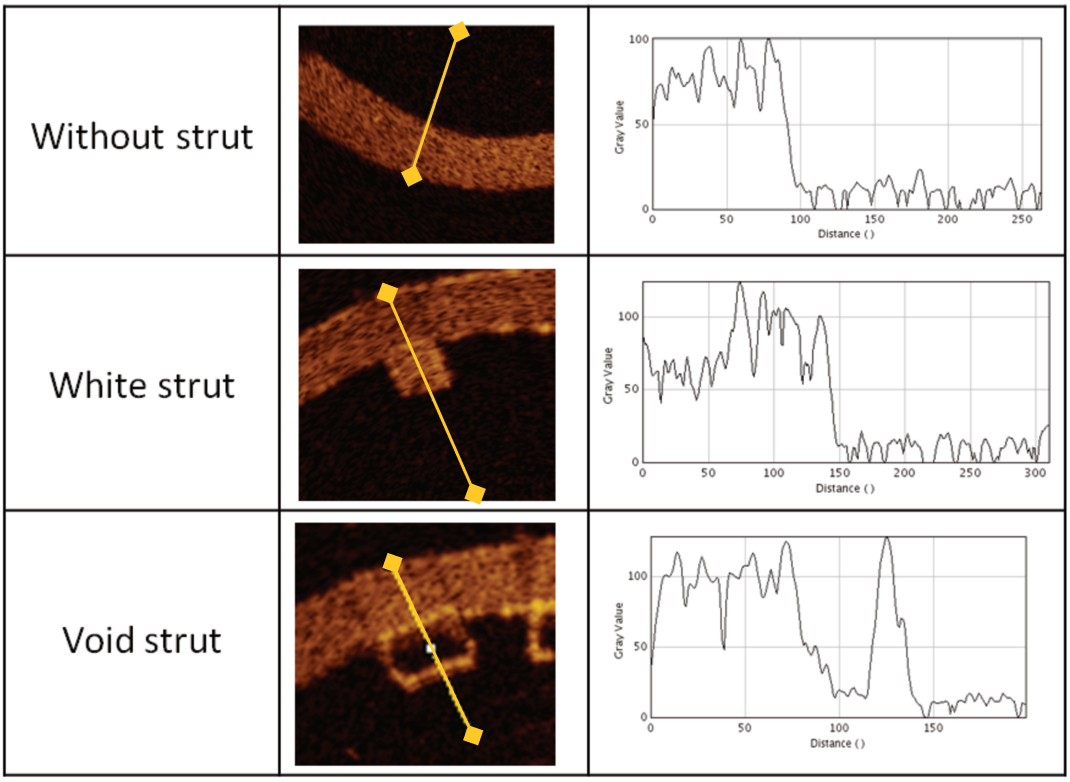

Figure 3.4: three situations for each point M of the outer contour; there is no strut (up), there is a white strut (middle) and there is a void strut (down)

C2. Rejection of outliers

The inner contour of the tube is smooth and thus two close points are not supposed to be too far from each other and the thickness of the tube measured for each of the two points is supposed to be similar. For two close points M_1' and M_2', knowing that the detection of M_1' is reliable, the detection of M_2' is rejected if $|M_1M_1' - M_2M_2'| > d_{thick}$ with d_{thick} a threshold value for the difference between the two thicknesses. Furthermore, to ensure that the determined points M' are indeed not belonging to a strut but are part of the inner contour, the maximum value I_{max} of I is calculated along M'C. If M' is not on a strut, it should be minimal because the stroke is going through the dark background – note that the points belonging to the shadow have been rejected and thus the metallic guide does not hamper the detection. Thus I_{max} is compared to I_{back1}, a threshold value that I_{max} should not exceed; if $I_{max} > I_{back1}$ the point is rejected. To do that, a first reliable point needs to be determined. A point in front of the shadow satisfying the second constraint and having a large intensity is chosen as the first reliable point.

C3. Interpolation to determine the missing points

The thickness of the tube at missing points is calculated by linear interpolation of the thicknesses of the tube at the determined points M'. To recover the whole inner contour, points are plotted so that |MM'| is equal to the estimated tube thickness.

3.2.2.2 Struts detection by coloring

As seen previously, struts are of two main different kinds: some are bright and homogeneously white, and others are void and dark inside with bright contours. Thus, a simple thresholding would not be sufficient to achieve the detection of the whole struts. Consequently, we chose here to fill the struts and strengthen the contrast between them and the background.

A. Crown of interest

The struts are situated in a crown between two roundish shapes: the inner contour of the tube and a circular shape with the same centre and a radius reduced by e_{strut}, the estimated thickness of the struts. To facilitate the detection, all the points located outside the inner contour and inside an inner circle obtained contracting the inner contour by e_{strut} are colored in black.

B. Filling the dark struts

For each point M' of the inner contour, the intensity along M'C is calculated. If M' is situated outside a strut, this intensity is low and inferior to I_{back2}. On the contrary if M' is situated inside a strut, this intensity will be superior to I_{back2} and for these points the intensity of associated M'' (the last point on M'C whose intensity is superior to I_{back2}) is stored.

For all the points situated inside struts, a stroke linking M' and M'' is drawn and for each point of this segment the measured intensity is replaced by an average value between a constant I_{color}, the intensity of the point, and the stored intensity of M''. This empirically chosen method aims to brighten the intensity inside the struts and so distinguish the dark pixels inside the struts from the dark background.

C. Between the struts

It sometimes happens that the inner contour is slightly inside the tube and thus a bright line can remain in the crown. To tackle this issue, a black stroke linking M' and C is drawn for each point M' known from previous step to be outside the struts.

Furthermore, if the point M' is next to a strut, several black strokes in different directions are drawn. Using different directions allows to better following the shape of the strut. To avoid coloring the struts, the directions are selected in order not to cross a strut, using the derivative of the intensity along the stroke, which should not be higher than $T_{derivative}$.

D. Increasing the average contrast

Now that the black struts are filled and that the contrast between struts and background is increased, the Rudin-Osher-Fatemi (ROF) method is applied to smooth the image; this method of regularization is chosen because it well preserves the edges[139]. Eventually the intensity is thresholded thanks to a threshold I_{ROF}.

E. Final mask and intensity

From the resulting image, a mask can be obtained which retains only the struts and is black outside them. This mask is applied on the original image, and thus the average intensity of the struts is calculated and stored.

3.2.2.3 Choice of the parameters

The program is tested on a set of images of various types and quality to verify its robustness and efficacy. The parameters are tuned with this aim, considering the following principles:

1. The detection of the outer contour needs to be very robust since the whole method lies on this step. Thereby, the goal is to have a satisfactory detection most of the time, even if it is not very precise.
2. Similarly, the main objective for the detection of the inner contour is the robustness, since any imprecision will be corrected by the coloring.
3. On the contrary, the struts' detection needs to be as accurate as possible; and this step is very sensitive to the parameters' choice. In particular, the detection of two close struts is challenging for our method. Indeed, we observed that either close struts are not separated, or close struts are well separated but some big struts are then divided in several parts. The first case implies that part of the background will be detected as belonging to a strut, which would have a non negligible impact on the average measured intensity. Under detecting some struts would have less impact on the results. Therefore the parameters were tuned to rather under detect some struts but separate as well as possible two close struts.

The final set of parameters is given in Table 3.1.

Table 3.1: final table of the empirical values used in the program

Inner contour detection		Outer contour detection	
Parameter	Value	Parameter	Values
d_{rough}	200 px	I_{back2}	0.25
I_{shadow}	0.2	I_{color}	1.75
d_{thick}	2 to 12 px	$T_{derivative}$	0.0545
I_{back1}	0.4	I_{ROF}	0.35

3.2.2.4 Analysis of image sequences and exclusion criteria

The method described above is used to perform an automated analysis of sequences of OCT images. Some images are excluded during the analysis if they meet the following specific exclusion criteria: 1) the detected external edge of the tube is too close to the edge of the image – because this leads to major errors during the mask creation and is also associated with a catheter that is too close to the struts and that thus gives aberrant detections; 2) images are excluded when the snake is too contracted and so no longer corresponds to the external edge of the tube. This rare error appears for very noisy images.

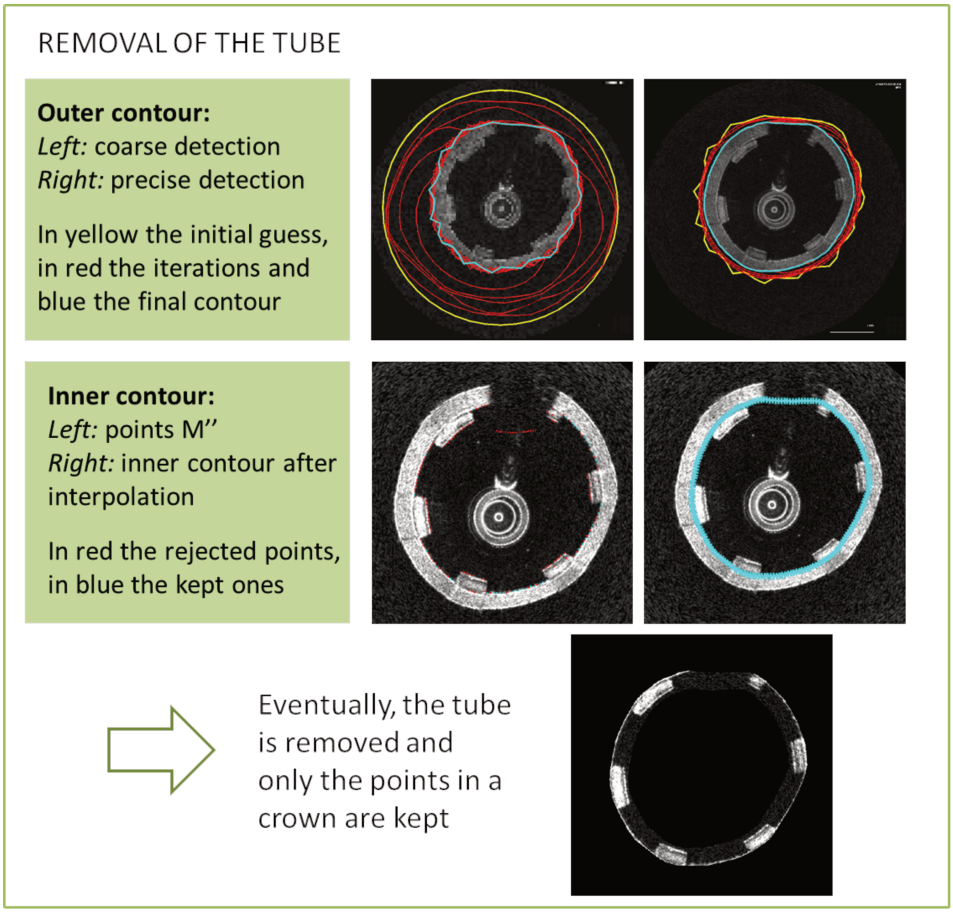

Figure 3.5: Summary of the automated method to detect BRS struts from OCT images

In addition to the criteria above which lead to systematic exclusion of images from the analysis, other images where potential errors are suspected are stored but set aside for subsequent evaluation and decision on whether or not they should be excluded. First, images are set aside if the distance between the catheter and the internal wall of the tube is smaller than 254 pixels, because this often hampers the detection. Second, images are set aside if the detected struts are "ghost struts", because this often occurs when the noise level in the image is very high leading to some void struts being detected by error. "Ghost struts" are defined by calculating the derivative of the GSI on a line connecting the catheter to the struts; the derivative is expected to exhibit a peak at some point – corresponding to the internal edge of the strut – and the GSI is expected to be above a threshold value at this point. If not, the image is set aside.

Ultimately, a final check on all image sequences is performed. Images on which discontinued struts (during the degradation process) overlap do not correspond to the model we have chosen and are thus difficult to analyze: some need to be excluded at this step; as well as images that are too noisy and images where the metallic guide is too close to the struts which hampers the detection. On average, 88.8 % of the automated detections realized on ~13,760 total images proved to be of very good quality.

3.2.3 Validation of the automated strut detection by comparison with manual analysis on selected slides

To validate the method of automated detection of stent struts, this method is compared to manual contouring of the struts in selected images. At five time points – 15 days, two, four, six and eleven months – for the three stents of one randomly chosen tube, three images are selected (the tenth image, the middle image of the image sequence, and the image situated ten slides before the end of the sequence). These slides are thus arbitrarily chosen to avoid any selection bias. In the rare case where a major artifact is observed for a particular image, the image immediately before or after it is chosen instead. Using the image analysis software ImageJ, struts are manually contoured and their GSI measured. The results are compared qualitatively by verifying that each strut is well spotted by the program and quantitatively by comparing the GSI measured using the manual and automated methods.

3.2.4 Accounting for the distance between struts and catheter

Upon imaging an axial section of the tube alone between two stents, we observed that the GSI varies with the distance between the catheter and the tube wall despite the fact that the tubing is homogeneous and its GSI is expected to be constant. An example of this dependence of the tube wall GSI on the distance from the catheter can be clearly seen in Figure 3.6a: the smaller the distance, the brighter the material. This effect is attributable to the amount of water the infrared light has to cross before reaching the object of interest, which leads to attenuation of the signal. Nevertheless, this phenomenon has to be taken into account for an accurate quantitative analysis of the GSI of a degrading stent. In order to

establish a correlation between GSI and the distance to the catheter d_C, we measured the GSI for square regions of interest (ROIs) of the tube alone (see the example in Figure 3.6b) and plotted the measured values as a function of d_C. We used the tube for this calibration because unlike the stent, the tube's GSI is expected to be spatially and temporally constant; thus, the observed variations of GSI are expected to be only due to variations in d_C. Approximately 170 measurements of the tube GSI as a function of d_C were used to determine this correlation. This correlation was eventually applied to the sequences of masks to correct the images. Knowing that the catheter is always positioned at the center of the image, the obtained correction is applied radially from the center. The corrected GSI is calculated for each image analyzed.

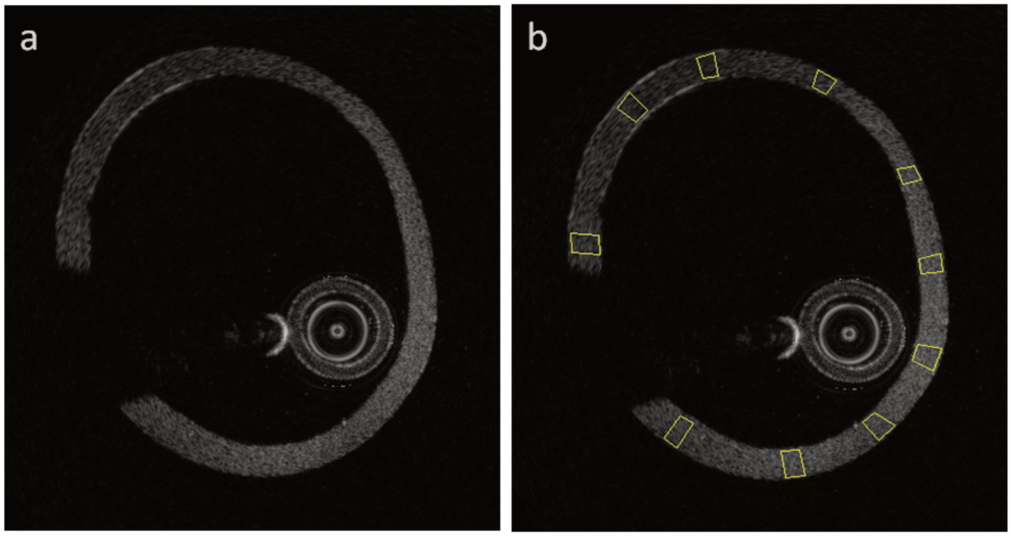

Figure 3.6: a: The brightness of the plastic tube depends on the distance to the catheter; b: Squares are drawn within the thickness of the tube, and analyzed thanks to ImageJ.

3.3 Results

3.3.1 Validation of the automated analysis method: comparison with manual analysis

Figure 3.7 depicts examples of the automated strut detection for ART1 (Figure 3.7a), ART2 (Figure 3.7b) and Abbott BVS (Figure 3.7c). The method proved capable of accurately identifying the struts even in seemingly more complicated cases such as when the tube is not perfectly circular (Figure 3.7a), when adjacent struts are very close together (Figure 3.7c), or when the struts do not have a square shape (Figure 3.7a). To validate the automated method, the results are compared to the manual contouring of struts using ImageJ. This comparison demonstrated that 139, 119, and 159 struts were accurately detected for the cases of the ART1, ART2, and Abbott BVS, respectively. On the other hand, 1, 3, and 6 errors were encountered in the respective cases, and these errors occurred primarily when two adjacent struts were located too close to one another and were thus detected as one. These results indicate that the automated strut detection method is capable of accurately identifying stent

struts in the vast majority of the cases and thus represents a reliable method for subsequent image analysis.

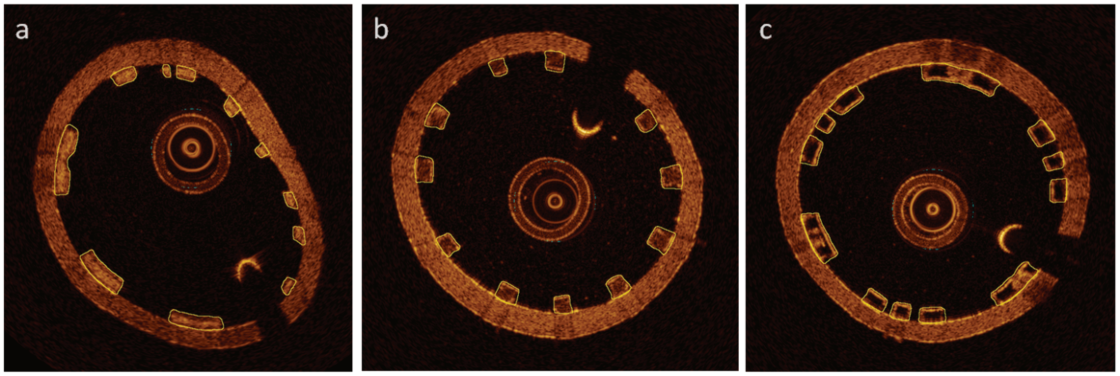

Figure 3.7: Examples of automated detection for ART1 (a), ART2 (b) and Abbott (c).

To further quantify the automated method's performance, we computed the difference in the measured GSI between the automated and manual detection (Figure 3.8). As shown in Figure 3.8a, this difference in the case of ART1 is below 5 % at four of the five time points tested and is between 5 and 10 % for the fifth time point. For the Abbott BVS, the difference in GSI is between 5 and 10 % for all time points; however, this does not necessarily indicate that the analysis is less accurate for the BVS than for ART stents. As can be seen from the comparison in absolute GSI values (Figure 3.8b), the GSI difference falls between 1 and 5 units for all three stents. This translates into a higher percentage difference in the case of the BVS because the average values of GSI for the BVS are considerably lower than those for the two ART stents. Furthermore, as will be seen later, the variation in GSI between the beginning and the end of degradation can reach 30 to 40 units; thus, an average GSI difference below 5 units between the automated and the manual analysis is considered acceptable for accurately following stent degradation. As an additional manner to visualize the comparison between the automated and manual analyses, Figure 3.9 directly compares the results of the automated analysis to those of the manual analysis for ART1 (Figure 3.9a), ART2 (Figure 3.9b) and Abbott BVS (Figure 3.9c) and clearly shows the very good correlation between the two approaches.

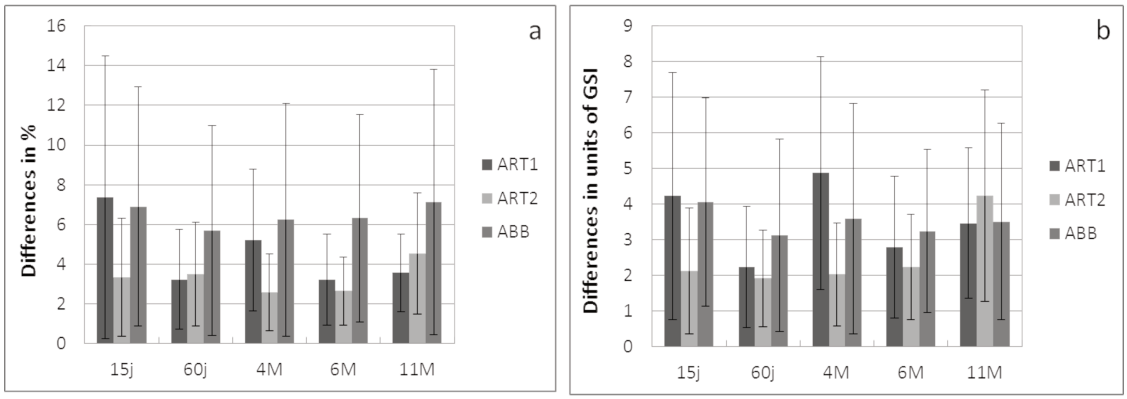

Figure 3.8: Differences between manual and automated analysis in percentage (a) and in units of GSI (b).

Now that the validation of the automated analysis is complete, it can be used for all images.

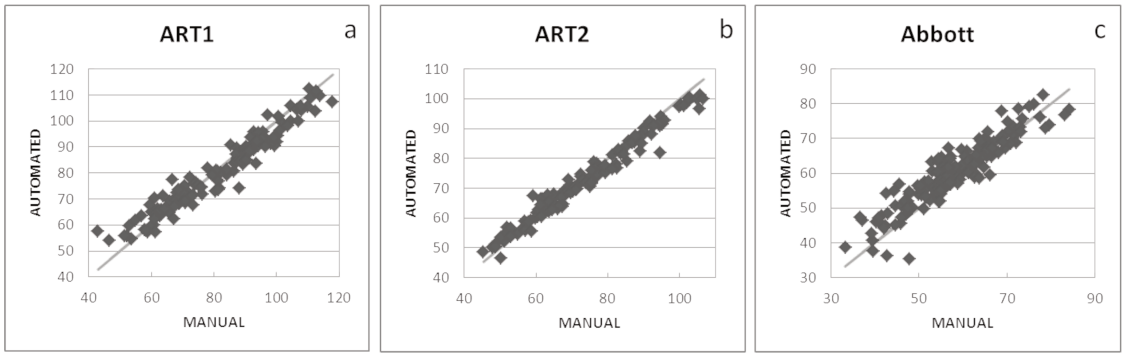

Figure 3.9: Automated versus manual GSI for the struts of ART1 (a), ART2 (b) and Abbott (c).

3.3.2 Correlation between GSI and distance between object and catheter

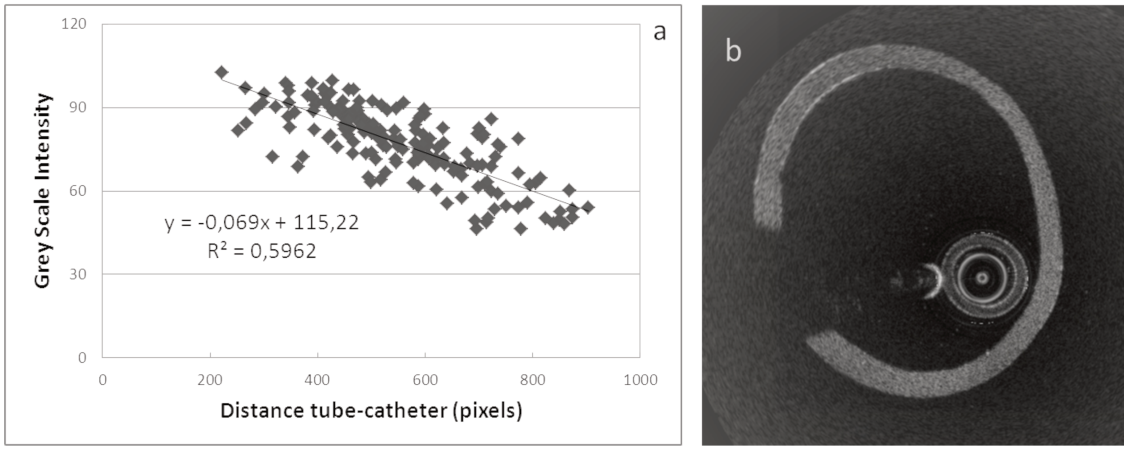

Figure 3.10: a: Correlation between GSI and d_c; b: Example of a rectified image.

Figure 3.10a depicts the measured GSI of ROIs of the tube as a function of the distance d_C between each ROI and the OCT catheter. A general trend of linear correlation is observed as expected, with a coefficient of correlation r^2=0.6. Thus can be written:

$$GSI_{measured} = -0{,}069 * d_C + GSI_0 \quad (3.4)$$

where GSI_0 is the theoretical GSI value that would be measured at a distance infinitely close to the catheter. Thus, to account for the influence of the distance of an object to the catheter – or the amount of water the infrared light needs to cross before reaching the object – we define a corrected GSI as:

$$GSI_{corrected} = GSI_0 = GSI_{measured} + 0.069 * d_C \quad (3.5)$$

This correlation can be applied radially from the center of the image to correct the image intensity. An example of a corrected image using this procedure is shown in Figure 3.10b. For each image of the sequences obtained experimentally, the average GSI and the average corrected GSI are calculated.

Figure 3.11: Evolution of the stents with degradation. ART1, ART2 and Abbott are the first, second and third column respectively; at 15days (a), 2months (b), 3months (c), 6months (d), and 11months (e) of degradation.

3.3.3 Analysis of in vitro stent degradation

3.3.3.1 Qualitative evaluation of stent degradation

As can be clearly seen in Figure 3.11 for ART1 and ART2, strut appearance varies with degradation state. The struts are initially dark, because the material is homogeneous; the more homogeneous a material, the darker it appears on OCT images. As the stent degrades, which corresponds to the breaking of polymeric polylactic acid chains and hence to an increase in the heterogeneity of the material, the struts generally become progressively brighter.

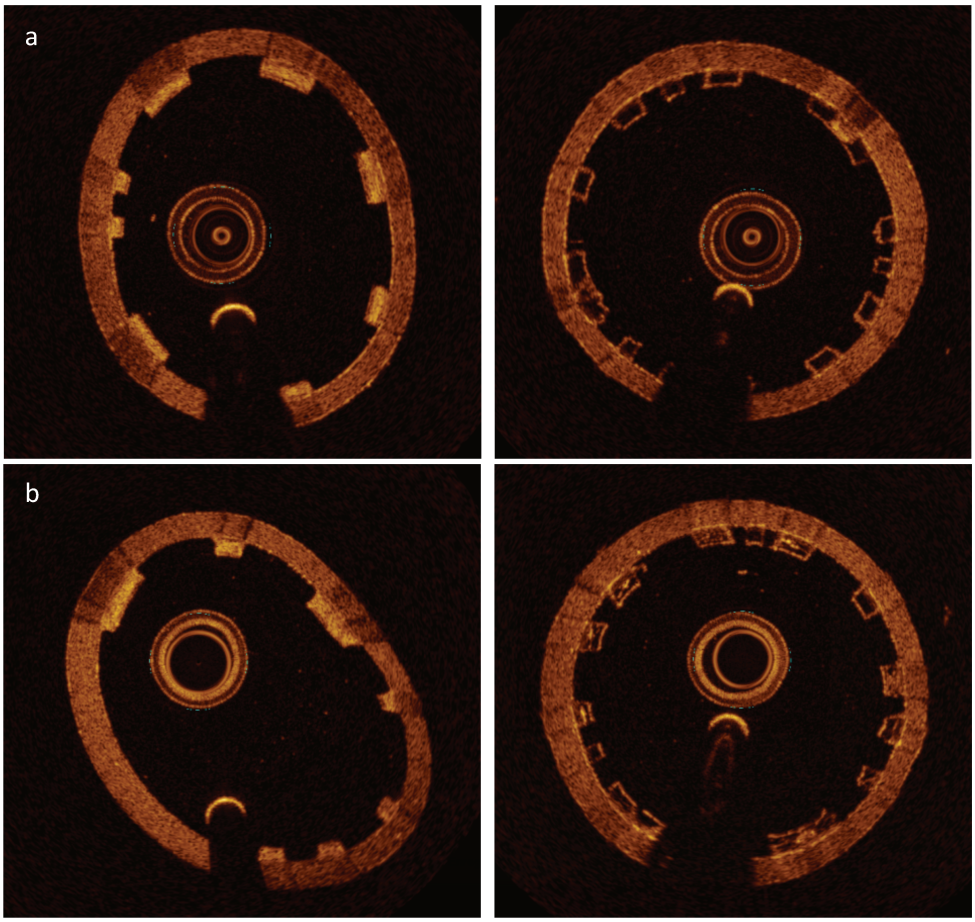

Figure 3.12: Evolution of stents with degradation at latter time points; at 18months (a) and two years (b) for ART1 (first column) and Abbott (second column).

Previous studies have provided a qualitative classification of the variations in strut intensity on OCT images during stent degradation[137]. These studies have reported passage through four distinct stages as the struts degrade: a preserved box, a partially preserved box, a dissolved black box, and finally a dissolved white box. The first two stages (the preserved box and the partially preserved box) can be recognized on the images. Indeed, the first two months of ART stent degradation appear to correspond to the preserved box stage, and a characteristic sandwich appearance similar to the partially preserved box can be recognized at three months. From that point, the ART stents struts appear whiter and whiter. Thus, the

two last stages of the classification, namely dissolved black box and the dissolved white box, do not seem to be relevant to describe the stents of our *in vitro* study. Rather, an alternative third stage that better describes the evolution of strut appearance would be simply a "white box". From one year onward, it is difficult to visually detect further evolution of strut appearance. During a first phase, ART stent degradation primarily takes the form of a modification of strut intensity. In a subsequent phase, the stents begin to exhibit strut discontinuities as can be seen in the example given in Figure 3.13. Note that the overlapping struts may be an artifact due to the physical contact between the metallic guide wire and the degrading stent. Struts discontinuities first occur between 9 and 17 months for ART1 and between 10 and 15 months for ART2, as detailed in Table 3.2. At the point of extensive strut discontinuities, a stent loses its integrity and is dissolved into the fluid within the glass tube. By 18 months, five of the six ART stents are observed to have completely lost their integrity (see Table 3.2). In the case of the Abbott BVS, no modification of strut appearance is detectable before two years (Figure 3.11). At two years, a clear increase in strut intensity is observed (Figure 3.12). This also corresponds to the time when the first struts discontinuities are detected for the BVS (Table 3.2 and Figure 3.13).

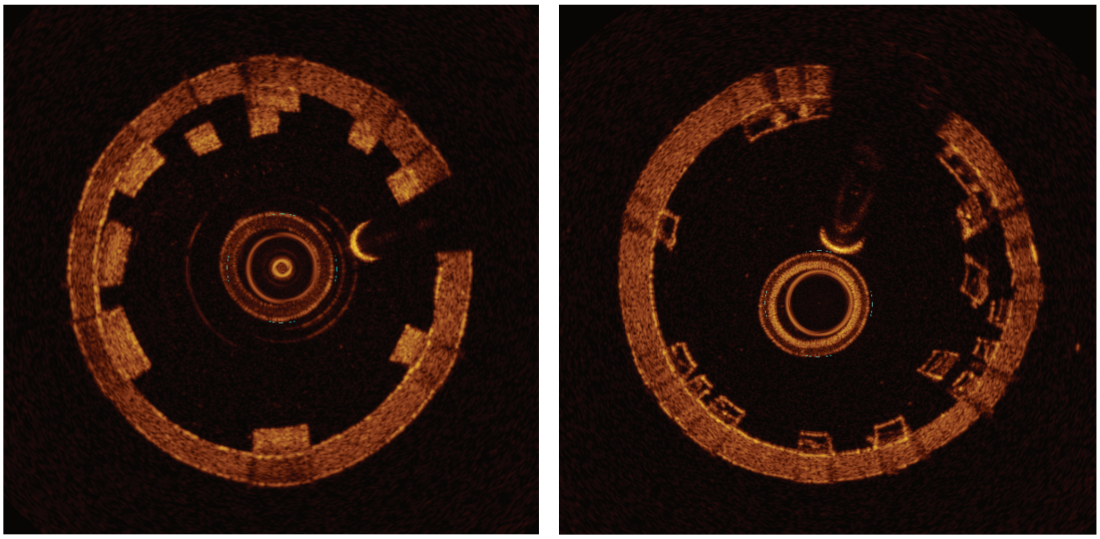

Figure 3.13: examples of struts discontinuities for ART stents (left) and for Abbott BVS (right). Note that the overlapping struts may be an artifact due to the physical contact between the metallic guide wire and the degrading stent.

Table 3.2: Times at which struts discontinuities where first seen and when the stent completely loses its integrity. S stands for sample and M for month.

	ART1			ART2			Abbott		
	S1	S2	S3	S1	S2	S3	S1	S2	S3
Struts discontinuities	9 M	17 M	12 M	12 M	10 M	15 M	-	23 M	24 M
Loss of the stent's integrity	13 M	18 M	-	18 M	18 M	18 M	-	-	-

3.3.3.2 Quantitative evolution of the GSI with degradation

The previous section provided a qualitative description of degradation characteristics and dynamics for the different stents used in the present study. In this section, we provide a more quantitative description of these processes. Figure 3.14Figure 3.14 illustrates the evolution of the GSI with time, both with and without the correction for strut-catheter distance described previously. Consistent with the qualitative observations described above, the quantitative analysis demonstrates that ART1 and ART2 exhibit largely similar behavior while the Abbott BVS behaves very differently. More specifically, for both types of ART stents, the degradation can be divided into the following three phases: 1) A first phase which lasts 1-1.5 months and where the GSI initially decreases (by ~6 GSI units for both ART1 and ART2). 2) A second phase where the GSI first increases quickly during two months (by ~30 GSI units for ART1 and ~20 for ART2) and then appears to decrease slightly for ART1 and to remain constant for ART2 before increasing again. 3) A third phase defined from one year of degradation until the loss of integrity of the stent during which the GSI increases very slowly and seems to tend to a plateau value.

In the case of the Abbott BVS, an initial drop phase can also be identified (a difference of ~12 GSI units between the maximal and the minimal GSI values during the first year). The GSI then starts to increase after 22 months of *in vitro* experiments, which corresponds to a whitening of the struts as can be visually observed in Figure 3.12. Thus, the Abbott stent appears to undergo the same first two phases of degradation as the ART stents showed but with a significantly longer time scale. These findings are consistent with the fact that Abbott stents are known to have a longer degradation period than ART stents.

Studying the kinetics of PLA degradation, it has been theoretically shown that chemical properties such as number-average molecular weight M_n follow an exponential decay with degradation[49,74]. The evolution of M_n with degradation thus appears to follow the equation:

$$M_n = M_{n0} \times e^{-k_h t} \tag{3.6}$$

where M_{n0} is the initial number-average molecular weight and k_h is a hydrolysis rate constant that depends on temperature, load, and pH. This equation has been validated by experimental measurements of M_n during degradation. Plotting $\ln(M_n/M_{n0})$ versus time allows the determination of the rate constant k_h for a given biodegradable polymer[29,49,126]. Since other properties such as the fracture strength of the polymer have been shown to evolve in a similar way to degradation[49], we assume that the second step of degradation, i.e. the increase in GSI which occurs rapidly at first and subsequently more slowly to attain a plateau, can also be described using the same type of exponential behavior. We thus write:

$$J(t) = J_0 + (J_m - J_0)(1 - e^{-k*(t-t_0)}) \tag{3.7}$$

where $J(t)$ is the theoretical GSI, J_0 is the minimum value of $J(t)$ reached at time t_0 which corresponds to the time at which the second phase begins, and J_m is the GSI value corresponding to the plateau.

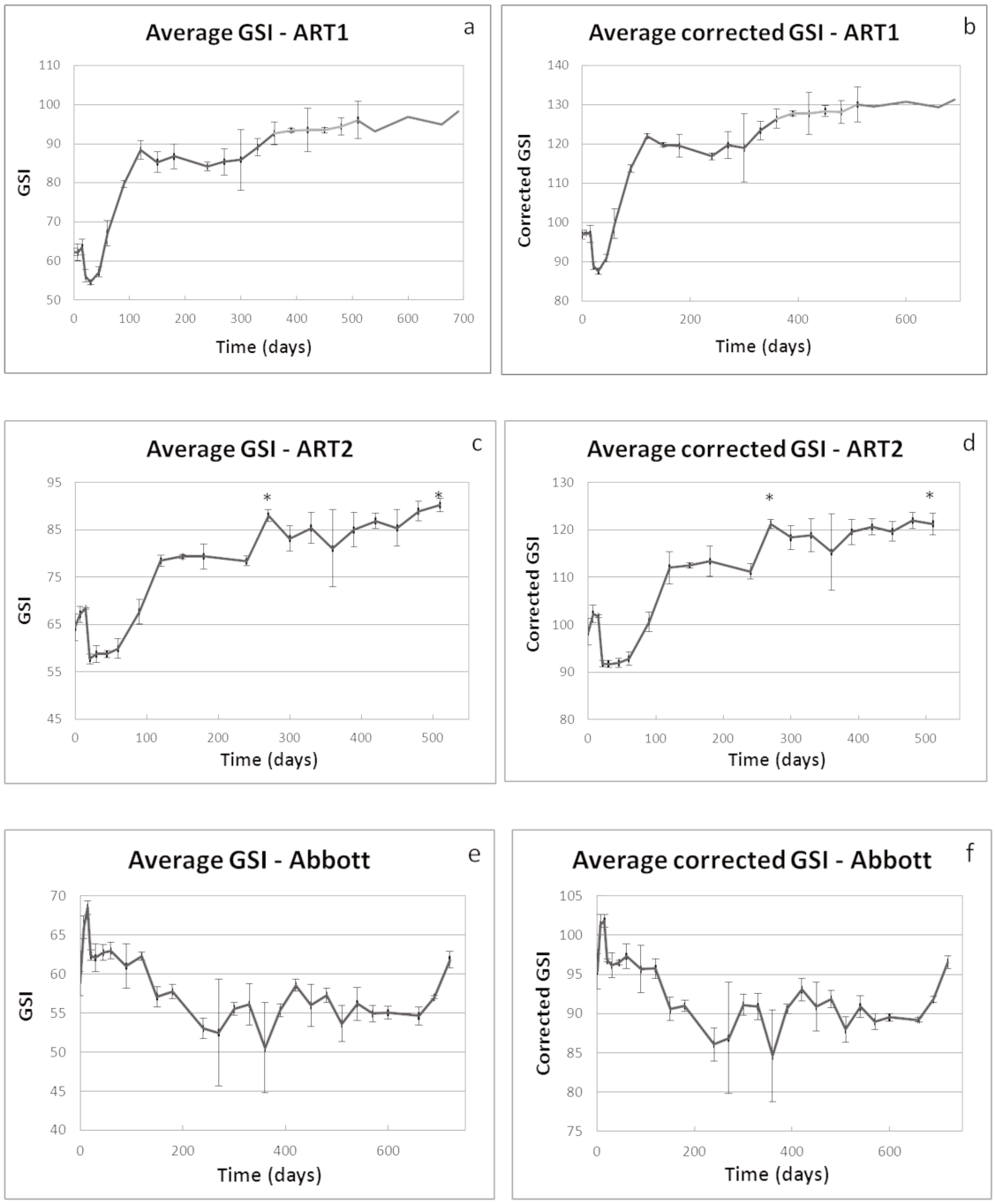

Figure 3.14: Evolution of the GSI and the corrected GSI for ART1 (a, b), ART2 (c, d) and Abbott (e, f). The dark grey corresponds to time points where the three samples of a given stent were intact, the light grey when two into three were intact, and the middle grey one into three persists. For time points where an asterisk is visible, one of the samples was not assessable because of experimental issues.

A least squares fit of our experimental measurements using this theoretical model of the GSI $J(t)$ is achieved, leaving J_0, J_m and k as adjustable parameters. The results are shown in the left figures of Figure 3.15 and Figure 3.16 for ART1 and ART2 using the data acquired until 18 and 17 months of degradation (since hereafter there is only one ART stent left into the six). As the degradation is not as advanced for the Abbott stent and as its second phase of

degradation is not complete, it is not possible to apply this method to BVS for now. This fitting allows us to determine a value for k of 0.0165 for ART1 and 0.0112 for ART2, with very good coefficients of determination r^2 of 0.921 for ART1 and 0.914 for ART2. The results are largely similar when the fitting is performed using the corrected GSI (Figure 3.15 and Figure 3.16, right figures), with k equal to 0.0159 for ART1 and 0.0095 for ART2 with r^2 of 0.915 for ART1 and 0.937 for ART2.

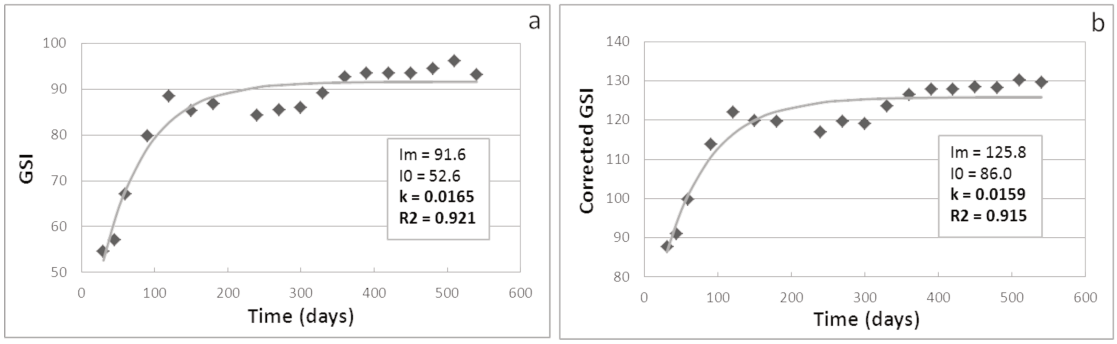

Figure 3.15: Fitting of the experimental data without (figure a) and with (figure b) the correction with the distance to the catheter, with the fitting by the theoretical model of J(t) for ART1 at 18 months.

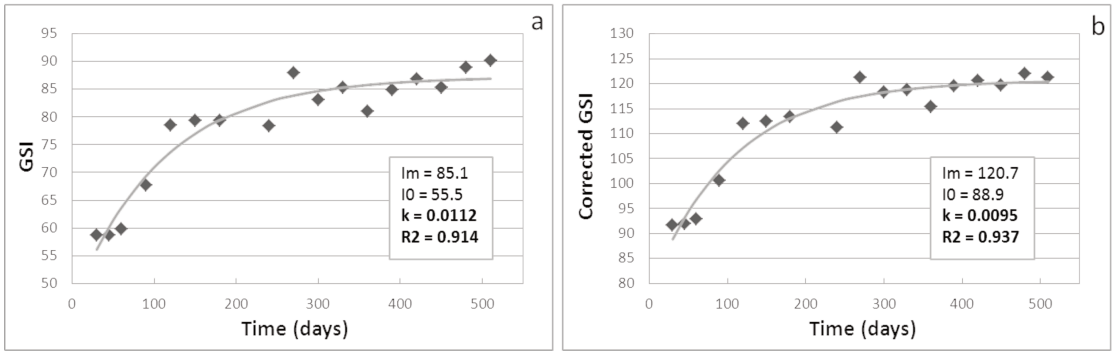

Figure 3.16: Fitting of the experimental data without (a) and with (b) the correction for the distance to the catheter with the fitting the theoretical model of J(t) for ART2 at 17 months.

3.4 Discussion

In this work, OCT was used to quantitatively follow and compare the degradation of three BRS: two designs of ART stents and the version 1.1 of Abbott BVS. Three samples of each type of stent were allowed to degrade in physiological serum at 37°C over a period of 24 months. At regular time intervals, OCT was performed and sequences of 60 to 90 images for the ART and Abbott stents were acquired. A minimum of 16 acquisitions were realized for the stent that degraded the fastest, and 28 acquisitions were performed for stents whose integrity remained intact at the two-year time point. To be able to treat and quantitatively analyze this large volume of data, a method to automatically detect the stent struts on OCT images was

developed. For each analyzed image, this method provided as output a white mask applied on the initial image, leaving only the struts whose average intensity could then be readily quantified.

Before using the automated strut identification and analysis method on the stent imaging data, we validated it against manual contouring of stent struts on a limited number of images. The validation produced very good results in terms of identifying the struts as well as accurately detecting their contours. During the process of image analysis, we discovered that the distance between an object of interest and the OCT catheter, which translates to the amount of water the light has to traverse, has a non-negligible influence on the resulting intensity. Accurate quantitative measurement of stent strut GSI required devising a correction for this artifact. To this end, we determined the dependence of the GSI on the distance between the object of interest and the OCT catheter which allowed us to obtain the needed correction. This correction was subsequently applied to the masks obtained with the automated method, and both the GSI and the corrected GSI were determined for each image. This allowed us to quantitatively follow and compare the degradation dynamics of the three different stents studied.

Qualitatively speaking, ART stent struts exhibited significant evolution in appearance on the OCT images during the first year of degradation. The struts could be classified into three stages of degradation: initially as dark boxes during the first two months of degradation, then as sandwich boxes that can be clearly seen at three months of degradation and remain slightly apparent at six months of degradation, and finally as bright white boxes. Abbott BVS showed no visual modification of struts appearance until the two-year time point at which a clear brightening of the struts occurred. Ormiston *et al.*[137] proposed that the *in vivo* degradation of BRS struts can be described qualitatively in terms of four stages: a black box, an open box, a dissolved black box, and a dissolved white box. Comparing this qualitative classification with what we observed, it is clear that Ormiston *et al.'s* black box corresponds to our *in vitro* dark box, and the open box very likely corresponds to our sandwich box. Thus, the first two stages of degradation appear to be similar for *in vitro* and *in vivo* degradation of BRS. Moreover, this type of classification has been used to track the *in vivo* degradation of ART stents in a porcine model [unpublished data], and it has been shown that after one month, 80 % of the struts were categorized as black boxes, whereas the open box configuration reaches a peak at three months accounting for around 70 % of the struts and then decreases to ~50 % of the struts at six months; this is thus very similar to what we observed *in vitro.* On the other hand, the final two stages, i.e. the dissolved black box and the dissolved white box, do not seem to be observed during the course of *in vitro* degradation of the stent, which is better described via a single third stage, a white box. This difference may be attributable to the fact that *in vivo* degradation of the struts is additionally associated with an infiltration of the degrading material by cells and connective tissue. In studies comparing histological features and OCT appearance[61], the last two stages of the classification seem to correspond to stages of integration of the struts in the arterial wall rather than to modifications due to degradation. For instance, Onuma *et al.*[61] studied the *in vitro* degradation of the first BVS design 1.0 in a porcine model and reported that at three years of degradation, the third stage (i.e. the dissolved black box) appears to be associated with the

formation of dense connective tissue at the location of the struts. Moreover, they demonstrated that although the struts were mainly classified as preserved boxes at two years, histology studies revealed the presence of proteoglycan with neither collagen nor cells at the location of the struts. Chemical studies measured a decrease of 98 % in the number-average molecular weight M_n at this time point. Thus, the OCT classification of the struts in four stages appears to be insufficient to fully describe and quantify the amount of degradation of the struts. This underscores the need for a quantitative study of the evolution of the stent strut GSI in order to better describe the evolution of the properties of a degrading BRS.

Regarding ART stent GSI, the degradation can be subdivided into three phases: an initial drop in GSI during approximately the first month, a phase of GSI increase that is initially rapid but then slows down until the third plateau phase is attained. Abbott stents appear to exhibit the same first two trends, i.e. an initial decrease in GSI followed by a sharp increase in intensity; however, this occurs at much longer time scales than the ART stents. For instance, the second phase does not begin until ~22 months post deployment. This is consistent with the fact that ART stents are designed to degrade more rapidly than the Abbott BVS.

We note that during the second phase of degradation of the ART1 stents, the GSI actually decreases slightly after a fast increase before it increases again. For the ART2 stents, this feature is less pronounced, but a period of GSI stagnation can be identified before the GSI begins to increase again. Several hypotheses can be advanced regarding this phenomenon: either it represents an additional phase of the degradation process that needs to be taken into account or it is an artifact of experimental measurements, as it is not seen in the case of the ART2 stents. Because this variation in GSI is of the same order of magnitude as the standard deviation of the measurements, we decided not to consider it as a separate degradation phase; however, this issues merits additional study.

For biodegradable polymers, various chemical properties including the number-average molecular weight commonly decrease exponentially with degradation. Other properties, most notably mechanical strength, have also been shown to follow the same trend. In light of those observations and given the second phase of the evolution of the GSI which increases to reach a plateau value, we fitted our experimental data to a theoretical evolution of the intensity given by equation (3.7). The coefficients of determination of the fits were always above 0.9, suggesting that the shape of the assumed profile was realistic. Moreover, the rate constant of the degradation derived from these fits (0.0165 and 0.0159 for ART1; 0.0112 and 0.0095 for ART2 – for the GSI and the corrected GSI respectively) are of the same order of magnitude as those that have been reported from experimental measurements of the evolution of ART stent number-average molecular weight (0.01 to 0.017; unpublished data). As a result, the evolution of the GSI with time appears to represent a useful surrogate for stent degradation process, allowing one to determine the rate of degradation of a given stent, in a non destructive manner contrary to chemical and mechanical tests. This finding also raises the intriguing possibility of using stent strut GSI based on OCT measurements to determine stent degradation dynamics *in vivo*. OCT could then be used to compare different designs of stents in clinical studies or determine the influence of parameters such as patients'

comorbidities on the degradation of a BRS. Further studies are needed to validate the current technique's ability to quantitatively track stent degradation *in vivo,* and especially to understand how the infiltration of proteins and cells affects the GSI values.

The present study has a number of limitations. We observed that the acquired OCT images were not always of uniformly high quality. This is thought to be due to various reasons. Firstly, it is very difficult to maintain the catheter centered along the length of the tube and to prevent it from touching the edges at some points. Not surprisingly, the difficulty in centering the catheter increases with an increase in stent length; thus, the acquisition was more difficult for the Abbott stents than for the ART stents. Secondly, some images were quite noisy, which obviously induces errors in strut detection. Finally, some images, despite their good quality, proved to be difficult to analyze using the automated method developed here. Examples include when the metallic guide is too close to the struts or if it casts a large shadow which complicates detection of the tube wall. We also encountered situations where two struts were very close together, and that led to some complications. Overlapping struts as well as struts detached from the tube wall can also lead to aberrant detections. Nevertheless, the effect of these various issues remains limited, and the majority of the images acquired could be analyzed using the automated method.

Another issue tackled in the present effort is to obtain a correction for the variation of the GSI with the distance to the catheter. A limitation here is that the coefficient of determination for the linear fit was only ~0.7. In fact, although the intensity of the tube wall was observed to generally decrease with increasing distance to the catheter, there were instances where two regions of interest of the tube wall had different GSI levels even though they were at an equal distance from the catheter. The source of this behavior is not known, but it may be due to defects in the catheter or to inhomogeneities in the tube wall.

Finally, the automated method described here has been developed to analyze *in vitro* images where the tube could be used as a positioning landmark. *In vivo* images exhibit different features and thus other appropriate landmarks would need to be established in order to perform the automated detection of stent struts. It is also expected that in the *in vivo* case, in addition to the distance-to-catheter correction, one would need to also correct for the attenuation of the signal due to any neointimal hyperplasia that develops over the stent struts.

CHAPTER 4

Arterial Lumen Adaptation to Stenting-Induced Modification of the Mechanical Environment: Comparison between BRS and BMS

4.1 Introduction

Stent deployment is the most common treatment for advanced atherosclerosis[59]. As seen previously, BRS are a potentially revolutionary concept in the field of interventional cardiology as they hold the tantalizing promise of providing a scaffold to the artery for only the time needed and then disappearing to leave behind a healed and compliant arterial wall[29]. Arterial Remodeling Technologies (ART) has developed a BRS made of poly-D,L-lactic acid (PDLLA), the ART Pure Bioresorbable Scaffold (ART PBS). In a six-month follow up study, Durand *et al*.[30] showed that ART PBS is able to provide as effective a scaffold for a swine coronary artery during the first three months post stenting as a control BMS (the Multilink Vision of Abbott). No difference was noted in the occurrence of adverse events between the two types of stents. However, at a later time, the BRS dismantles, thus "freeing" the vessel and allowing a positive gain in lumen diameter (termed "positive remodeling"), whereas this does not happen in the case of the BMS where the artery remains permanently caged.

Despite these very promising initial results, the effect of a BRS on the arterial wall in terms of mechanical stresses and the evolution of these stresses during the degradation period remain largely unknown. It is well established that arteries adapt structurally and geometrically to maintain mechanical homeostasis. During various physiological and pathological scenarios, arteries experience variations in their mechanical environment, and these variations may involve axial stresses, shear stresses, hoop stresses, or a combination of these stress components[102]. Axial stress levels in arteries change dramatically during growth, leading to an increase in vessel length. As for the effects of shear stress, Langille *et al*.[123] conducted pioneering *in vivo* experiments in which they reduced blood flow in the common carotid

arteries of rabbits by ligating the external carotid artery. They observed that this reduction of blood flow, and hence of arterial wall shear stress, was associated with a marked decrease in lumen diameter, which has the effect of increasing wall shear stress. In these studies, the diameter of the control contralateral carotid arteries did not change. Indeed, the results of these and other studies suggest that arteries adapt their lumen diameter to maintain a constant wall shear stress[102]. In addition to axial and shear stresses, hoop stresses also drive arterial wall remodeling. For instance, induced hypertension, which leads to an abnormally high hoop stress, drives the arterial wall to thicken with the aim of decreasing the hoop stress towards a more physiological stress value[103,140]. The results of the various studies cited above demonstrate that changes in the mechanical stress environment experienced by the artery lead to a modification of the vessel architecture in order to maintain and restore mechanical homeostasis.

Stent deployment represents a massive and long-term modification of the mechanical stress field experienced by the artery. In this context, one may wonder if the stented vessel remains capable of modifying its geometry and architecture to adapt to this very different mechanical environment, if it is able to reach a homeostatic equilibrium even if stented, and if the artery reacts differently to a BMS than to a BRS.

Optical coherence tomography (OCT) technique is an endovascular imaging technique that allows one to follow the evolution of the arterial lumen diameter during the months following a stenting procedure. In the present work, *in vivo* OCT measurements were performed on miniswine to determine arterial luminal diameter at various points following deployment of either a BMS or a BRS. The OCT measurements were subsequently used to compare the time evolution of shear stress experienced by the arterial wall for BMS and BRS. The initial shear stress estimates were based on the idealized assumption of fully developed steady flow (Poiseuille flow) within the artery. To account for the effects of flow pulsatility, computational fluid dynamic studies were conducted using a finite element code. The results demonstrate significant differences in wall shear stress evolution between BRS and BMS.

4.2 Materials and methods

To understand the impact of a stent on the arterial mechanical environment, we have relied on animal data provided through a collaboration with Arterial Remodeling Technologies (ART®), a BRS startup company based in Paris, France. The ART study focused on tracking the impact of BMS and BRS implanted in miniswine over a period of one year. Among other techniques used in this study, OCT imaging was performed regularly. The imaging data provided information on the evolution of lumen diameter for both BMS and BRS, and this was used in our analysis to estimate the evolution of wall shear stress.

4.2.1 Animal experiments

Animal protocols were managed by the Institutional Animal Care and Use Committee of AccelLAB (laboratory in Montreal, Canada where the experiments were conducted) in accordance with the guidelines and regulations of the Canadian Council on Animal Law Regulation. Fifty healthy Yucatan female or castrated miniswine between the ages of 30 and 50 weeks and weighing 25-50 kg were used in the study. Each animal randomly received two or three stents in their coronary arteries, implanted via femoral access. In all, 79 ART® BRS (3.0x11 mm) and 61 BMS (Multilink Vision®, Abbott®, Santa Clara, USA, 3.0x12 mm) were implanted. OCT was performed on three animals at each time point (1 month, 3 months, 6 months, 9 months, 12 months). One animal died during the course of the study.

4.2.2 OCT imaging

OCT imaging used the C7-XR™ OCT intravascular imaging system (St. Jude Medical, St. Paul, MN, USA) and OCT image analysis used the ILUMEN software. For each stented section, a sequence of axial sections spaced 1 mm apart was analyzed. In addition, control images were acquired in the unstented portion of the artery at locations 1 mm from the proximal and distal ends. For each section, the vessel lumen area was measured for both the stented and the unstented portions (Figure 4.1). Lumen surfaces were automatically detected by the software, with only a few manual modifications necessary. For the unstented portion, the average value of the proximal and distal sections was used as the reference value. Vessel diameters were not directly measured but were rather computed from the measured area values.

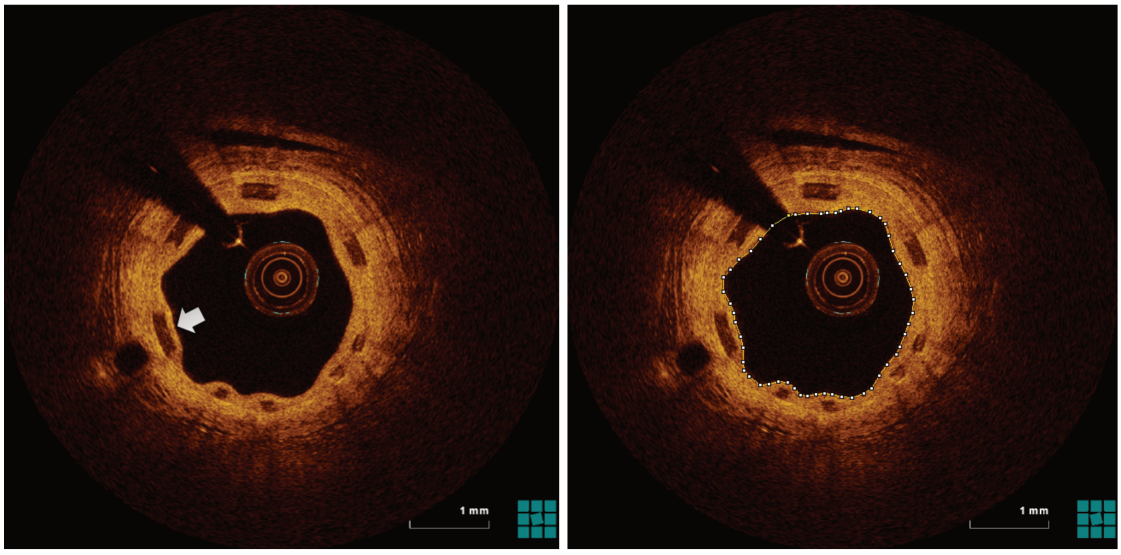

Figure 4.1: example of an image obtained *in vivo* thanks to OCT. On the left panel, the arrow indicates a stent's strut embedded in the arterial wall. On the right panel determination of the lumen is shown.

4.2.3 Modeling

4.2.3.1 Analytical formulation

Considering fully developed, laminar, and steady flow in a cylindrical artery, the velocity distribution in the artery can be analytically determined and takes on the well known parabolic (Poiseuille) profile given by:

$$v_z(r) = \frac{K}{4\mu_d}(R^2 - r^2) \tag{4.1}$$

With:

$$K = \frac{dP}{dz} \tag{4.2}$$

Where $v_z(r)$ is the fluid velocity in the axial direction z, μ_d the dynamic viscosity, R the radius of the lumen, P the pressure and K a constant. From this profile one can deduce the expression of the cycle average volumetric flow rate Q:

$$Q = \iint_{r,\theta} r \times v(r) dr\, d\theta = 2\pi \int_0^R \frac{K}{4\eta}(R^2 - r^2) r dr = \frac{K\pi R^4}{8\mu_d} \tag{4.3}$$

One can also deduce the shear stress at the arterial wall τ_w:

$$\tau_w = -\mu_d \frac{\partial v_z}{\partial r}\Big|_{r=R} = \frac{KR}{2} \tag{4.4}$$

Combining this equation with the expression of Q allows to define τ_w as:

$$\tau_w = \frac{32\mu_d Q}{\pi \times \emptyset_{lumen}{}^3} \tag{4.5}$$

where $\emptyset_{lumen}$ is the diameter of the arterial lumen. If we assume that the average flow rate Q is constant along the studied portion of the artery and is identical for all the animals, then the wall shear stress is determined solely by the vessel diameter which is measured by OCT. Thus, plotting the evolution of the OCT-measured $1/\emptyset_{lumen}{}^3$ over time for both the BMS and BRS cases provides the corresponding evolution of wall shear stress.

4.2.3.2 Numerical model

The analysis above suggests that the wall shear stress is directly proportional to the quantity $1/\emptyset_{lumen}{}^3$; however, the analysis was based on the assumption of steady flow. Blood flow in coronary arteries is obviously pulsatile. To determine if the same relationship between vessel diameter and wall shear stress holds for the case of pulsatile flow, we performed computational fluid dynamic simulations using the commercial finite element multiphysics code COMSOL 4.3b.

In the simulations, blood is modeled as a Newtonian fluid. This assumption is valid whenever the shear rate is larger than 100 s^{-1} [141], which is expected to generally be the case for coronary arteries[142]. The density of blood is set to 1060 $kg.m^{-3}$ and the kinematic viscosity to $3.5\ 10^{-3}$ Pa-s. The artery is assumed to be a rigid wall cylinder with a diameter of 2 mm, representative of a coronary artery, and a length of 10 cm. This length needed to be sufficiently large to ensure that the flow becomes fully developed. For steady flow, the flow entrance (or developing) length can be approximated by $L_e \sim 0.05 \times R_e \times \emptyset_{lumen}$ [143], where Re is the flow Reynolds number. For a typical average velocity in a 2 mm-diameter coronary artery of 30 cm/s, R_e~180, and L_e~1.8 cm; therefore, the assumed vessel length of 10 cm is sufficient to lead to fully developed flow.

For the steady flow simulations, the boundary conditions were as follows: zero pressure at the outlet, no slip (zero velocity) at the vessel walls, and at the inlet, a velocity defined as followed:

$$v_R = \frac{Q_0}{\pi R^2} \tag{4.6}$$

Where Q_0 is the volumetric flow rate calculated for a standard coronary artery, that is to say an average velocity of 30 m/s and an average radius of 1 mm. This allows us to study the relationship between τ_w and *R*, for a constant volumetric flow rate as defined in equation (4.5).

For the pulsatile flow simulations, the pulsatility was assumed to be purely sinusoidal with no flow reversal so that the inlet boundary condition took the form:

$$v_R(t) = \frac{Q_0}{\pi R^2}(1 + \cos(\omega t)) \tag{4.7}$$

where ω denotes the angular frequency of flow pulsation, which is taken to have a value of 2π (corresponding to a cardiac frequency of 1 Hz), which corresponds to a Womersley number of 1.4. All other boundary conditions were identical to the steady flow case.
The wall shear stress was evaluated as follows:

$$\tau_w = -\mu \frac{\partial v_z}{\partial r}\bigg|_{r=R} \tag{4.8}$$

For steady flow, the wall shear stress is constant. For the pulsatile flow simulations, we computed the maximum value of wall shear stress during the cardiac cycle. In all cases, wall shear stress was evaluated at an axial position 5 mm from the downstream end in order to ensure that fully developed flow is reached.

4.2.3.3 Statistical analysis

The statistical analysis was performed using a Student t-test. Results are statistically significant for $p<0.05$ and hereafter marked with an asterisk.

4.3 Results

4.3.1 OCT images: evolution of lumen diameter

From the series of OCT images, we are able to determine the evolution of arterial lumen area (Figure 4.1) from which lumen diameter is deduced under the assumption of a circular vessel cross-section. To understand the impact of a stent compared to a normally evolving unstented artery, the diameter is determined for both the stented and the unstented portions of the artery and for both BMS and BRS. The evolution of lumen diameter with time is depicted in Figure 4.2.

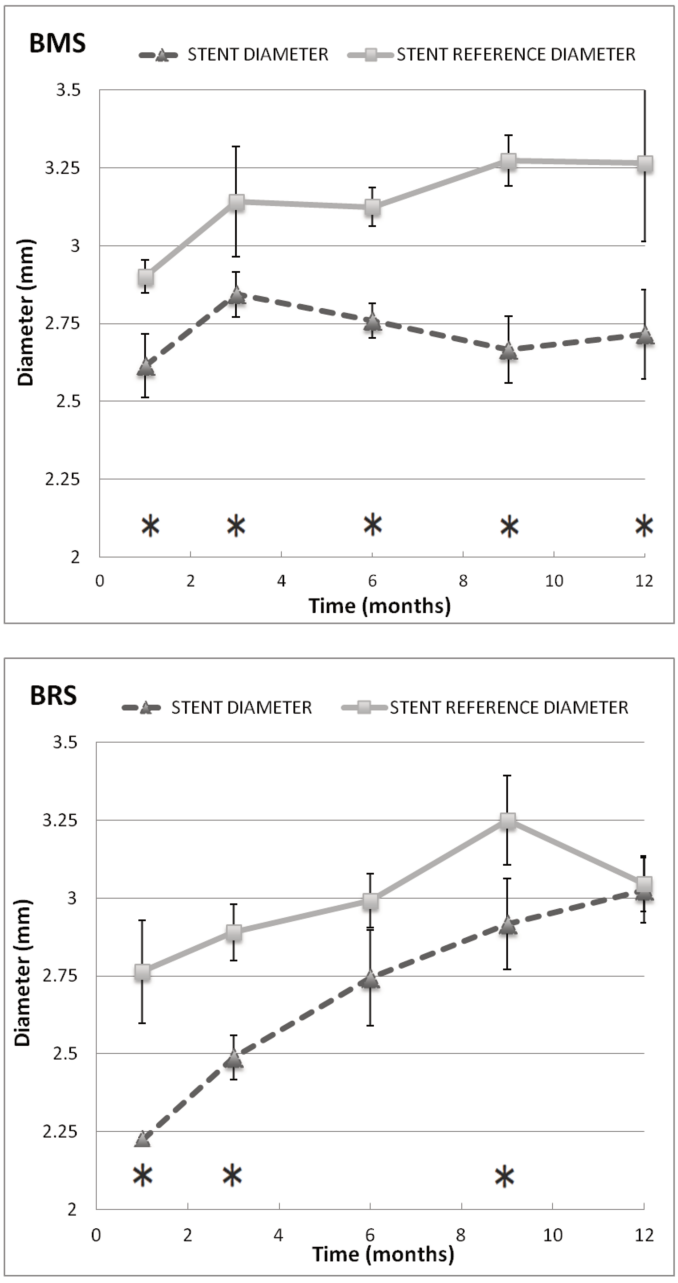

Figure 4.2: Evolution of the OCT-measured lumen diameter for BMS (top panel) and BRS (low panel). The "reference diameter" denotes the average diameter of sections upstream and downstream of the stented portion. * denotes a statistically significant difference ($p<0.05$).

At the beginning of the study, the lumen diameter of the stented section is smaller than that of the unstented part of the artery for both BRS and BMS, presumably due to neointimal hyperplasia induced by the arterial injury caused by the deployment of the stent, the resulting inflammation, and the induced stresses. One can note that the lumen diameter of the stented section is initially smaller for BRS than for BMS (2.2±0.009 mm vs. 2.6±0.1 mm at one month; $p<0.05$). This is likely attributable to the fact that the struts of BRS are thicker than those of BMS (170 µm vs. 81 µm). Figure 2 also shows that the unstented lumen diameter increases with time for both stent types, which is attributable to the growth of the animals. However, whereas the stented lumen diameter remains virtually constant with time for BMS, BRS stented lumen diameter exhibits a clear increase with time, until it reaches the value of the unstented portion of the artery at 12 months.

4.3.2 Numerical model: mesh independence

We performed mesh independence studies for $R = 1\,mm$ and ultimately use the mesh for which the difference in wall shear stress relative to a finer mesh was below 0.1 %.

4.3.3 Numerical model: evolution of the wall shear stress with vessel radius

The COMSOL computational fluid dynamic model is used to compute the velocity profile and shear stress at the arterial wall for both steady (Poiseuille) flow and sinusoidal pulsatile flow, and the dependence of the wall shear stress on lumen diameter is investigated. As shown in Figure 4.3, the computed velocity profile for steady flow is parabolic and matches very closely the analytical Poiseuille solution. Figure 4.5a demonstrates that the computed wall steady flow shear stress is directly proportional to $1/Ø^3$, indicating that the computational results are capable of reproducing the analytical Poiseuille solution for wall shear stress.

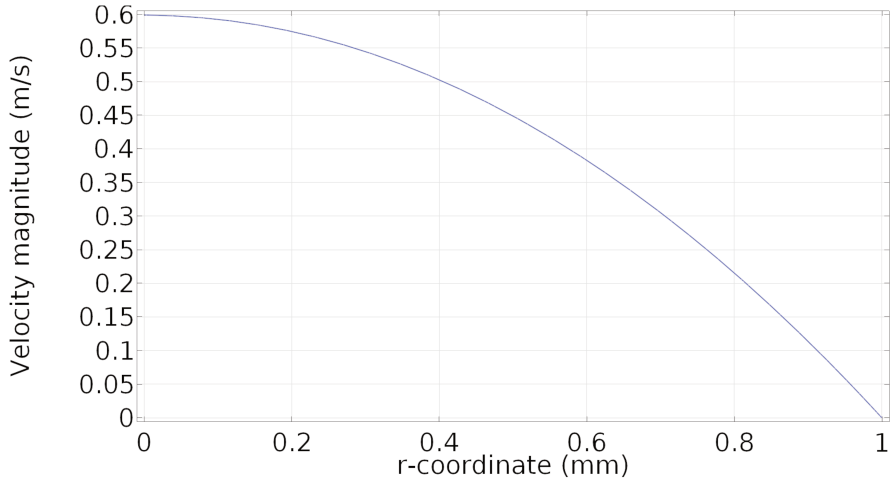

Figure 4.3: computed velocity profile at fully developed flow for steady flow

Now that the computational model has been validated against the analytical Poiseuille solution, it was used for the case of pulsatile flow.

Figure 4.4a and Figure 4.4b respectively depict the computed velocity profiles within the vessel for a line situated within the entrance length (2 mm downstream of the inlet) and for a line situated within the fully developed flow region (2 mm upstream of the outlet). Within the entrance length, the velocity increases as one moves away from the wall, reaches a maximum, and then slowly decreases towards the center of the vessel. This type of profile is consistent with Womersley flow analysis[144].

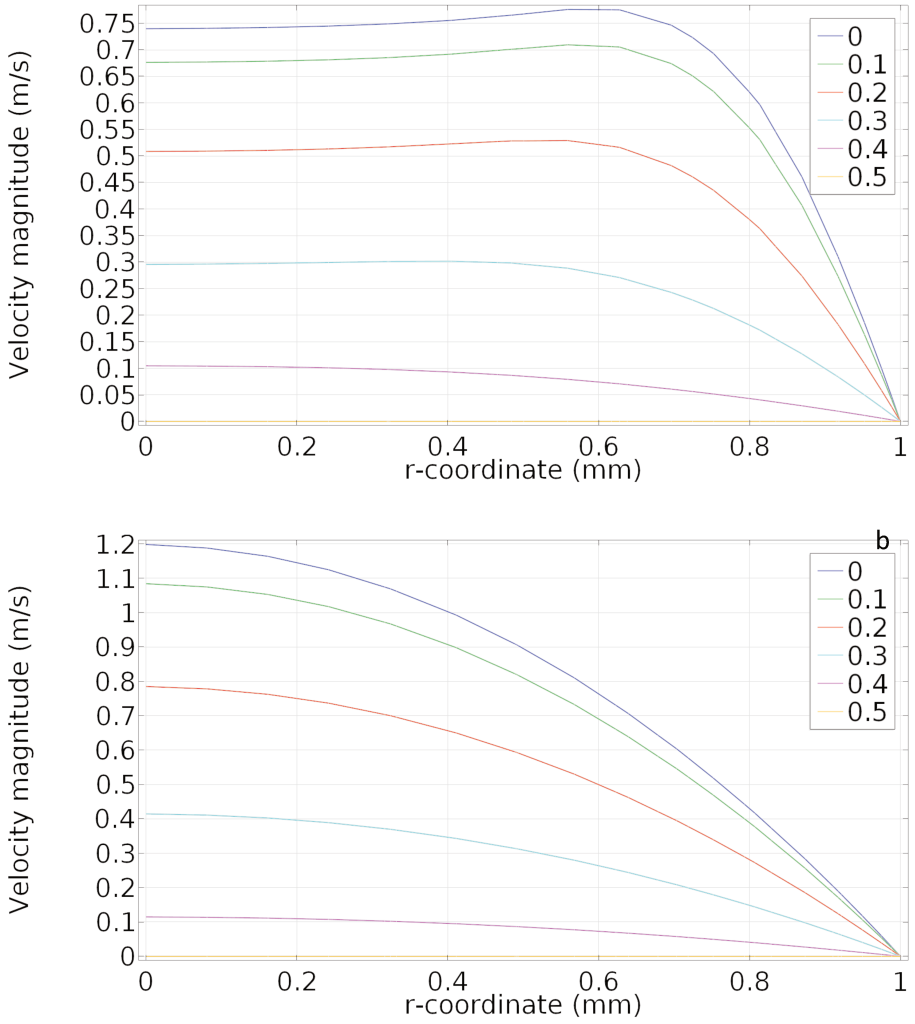

Figure 4.4: computed velocity profiles within the vessel for a line situated within the entrance length (2 mm downstream of the inlet) (a) and for a line situated within the fully developed flow region (2 mm upstream of the outlet) (b)

For fully developed flow, on the other hand, the velocity profiles exhibit parabolic shape at each time step. In terms of wall shear stress, Figure 4.5b demonstrates that the maximum wall shear stress during the cardiac cycle is directly proportional to $1/Ø^3$. Therefore, even if flow pulsatility is taken into account, the simple quantity $1/Ø^3$ appears relevant as an

indication of the wall shear stress within the vessel. Hence, the OCT measurements of the temporal evolution of arterial diameter *in vivo* following BMS and BRS deployment can be used to assess the evolution of wall shear stress within the artery.

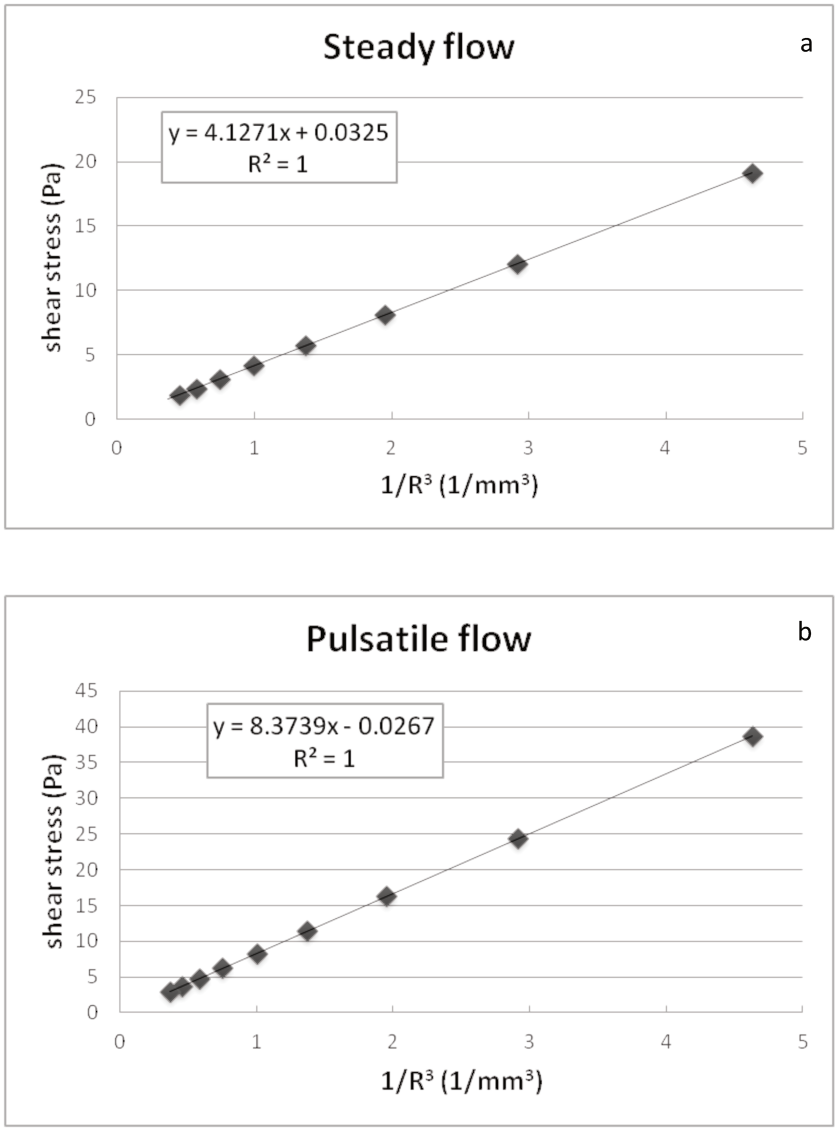

Figure 4.5: Computed shear stress as a function of $1/R^3$, which is proportional to the wall shear stress for steady flow (a) and sinusoidal pulsatile flow (b).

4.3.4 Evolution of arterial wall shear stress with following BMS and BRS deployment

Based on the above results, we assume that the evolution of the quantity $1/\emptyset^3$ in an artery as measured by OCT can be used to approximate the evolution of wall shear stress. Figure 4.6 depicts the evolution of $1/\emptyset^3$, and hence of wall shear stress, based on the OCT measurements (cf: Figure 4.2) for both BMS (a) and BRS (b) for stented and reference parts of the vessel. In the case of BMS, the wall shear stress remains virtually constant throughout the study because the artery remains caged and is unable to adapt its luminal diameter. There is

thus a constant gap between the shear stress experienced by the stented and unstented portions of the vessel. For BRS, the wall shear stress is initially higher than the BMS value. This is likely attributable to the higher degree of neointimal hyperplasia observed for BRS (probably due to the thicker BRS struts, as noted previously). Interestingly, however, the wall shear stress of the stented portion decreases in the following months and appears to tend to a plateau value ~30 % of the initial shear stress. Besides, the gap between stented and unstented parts progressively decreases and disappears at 12 months. Thus, the shear stress decreases to tend to a plateau value which corresponds to the stresses experienced by the unstented part of the artery. These results are strongly suggestive of the occurrence of a shear stress-driven arterial adaptation in the case of BRS, while such adaptation is impossible for BMS in which the wall remains caged by the stent.

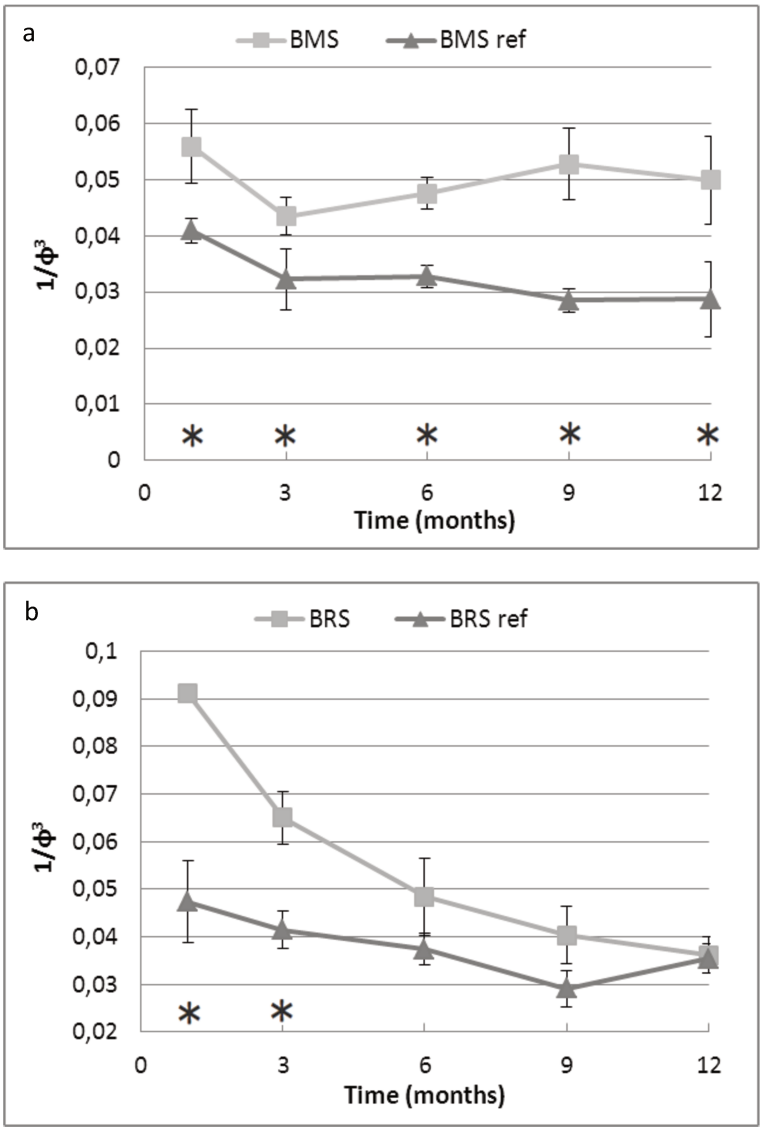

Figure 4.6: evolution of $1/Ø^3$ for BMS (a) and for BRS (b). The darker line and the lighter line represent the evolution of $1/Ø^3$ for the reference and the stented arterial section respectively. * denotes a statistically significant difference ($p<0.05$).

4.4 Discussion

During physiological and pathological processes, arteries are subjected to significant variations in their mechanical environment. In order to adapt to these changes and maintain homeostatic values of the applied stresses, most notably the wall shear stress and the mural hoop stress, vessels are able to modify their lumen diameter and their wall thickness[102,103,123]. When a stent is inserted into an artery, it not only changes the biomechanical stresses within the vessel but also cages the artery and thus hinders the arterial remodeling process. We wanted to compare the impact of BRS and BMS on the perturbations of the shear stress and on the biological remodeling *in vivo.* To this end, we used the results of collaborators who conducted *in vivo* OCT measurements on stents implanted in miniswine. We studied both the stented and unstented portions of the artery in order to isolate the impact of the device from the effects of the normal evolution of a vessel. From the values of lumen diameter determined by OCT, we deduced the wall shear stress by simply assuming the validity of a Poiseuille model. Using computational fluid dynamic simulations, we showed that the conclusions drawn based on Poiseuille flow remain valid even in the case of pulsatile flow because the dependence of wall shear stress on wall shear stress is similar in both cases.

The OCT measurements revealed that for both BMS and BRS, the arterial lumen diameter is smaller in the stented portion than in the unstented portion of the vessel during the first months, presumably due to the neointimal hyperplasia induced by stent implantation. Subsequently, the lumen diameter of the unstented portion increases in all vessels due to animal growth. In the stented portion, the arterial lumen diameter increases in the case of BRS but remains constant in the case of BMS. Thus, the degradation of the BRS and the dismantling of its structural elements allow arterial remodeling and changes in lumen diameter, whereas the BMS cages the artery and prevents this remodeling. These results confirm previous findings by Durand *et al.*[30].

Assuming a constant flow rate through the artery, the increase in arterial lumen diameter observed as a BRS degrades would be expected to be associated with a decrease in wall shear stress. We observed that the deduced wall shear stress decreased progressively until reaching a near-constant value ~9 months after BRS deployment. This value is thought to represent the homeostatic shear stress reached following the biological remodeling of the arterial wall, since it corresponds to the shear stress experienced by the unstented part of the vessel. Thus, although the wall shear stress was non-physiological shortly following BRS deployment, and was significantly higher than that for BMS, the artery was able to undergo the necessary remodeling in order to restore a physiological constant value, and this adaptation to the modified mechanical environment was allowed because of the dismantling of the stent. On the contrary, a BMS cages the vessel and prevents it from adapting to the new mechanical environment induced by the deployment of the stent. It should also be noted that a BRS allows the stented arterial lumen to have the same diameter as the unstented portion of the artery thereby eliminating the compliance mismatch between the stented and unstented portions of the vessel. This is thought to lead to a more physiologically favorable situation than the case of BMS where the gap between the stented and unstented portions is further exacerbated by the growth of the animal.

The notion that the arterial lumen adapts to maintain a homeostatic wall shear stress value is not new. Thoma was the first to report that a modification of arterial volume flow rate was associated with a predictable modification of the lumen diameter and that arterial lumens tended to be larger in regions of higher flow[145]. In 1926, Murray considered the size of the vessel as an optimization problem between two phenomena: the workload on the heart which would require the vessels to be as large as possible, and the metabolic burden to produce large amounts of blood which would require vessels to be as small as possible[146]. Theoretically solving this optimization problem led to a solution in which the cube of the lumen diameter is proportional to the volume flow rate. In 1977, Zamir *et al.*[147] noted that "Murray's law" could be interpreted as a constancy of wall shear stress. This adaptation to shear stress has subsequently been experimentally observed by Langille *et al.*[123] whose pioneering work tried to explain how an artery is able to adapt to changes in shear stress and showed that this adaptation required the presence of an intact endothelium. They also observed that the response of the artery to a decrease in wall shear stress occurs in two distinct phases: an initial short term phase where the lumen diameter decreases and the response can be reversed by the application of papaverine, a smooth muscle cell relaxant; and a longer term irreversible remodeling leading to a diameter reduction that is insensitive to the application of papaverine. In this context, our work aims to study this arterial wall adaptation to changes in shear stress in the particular case of a stenting procedure and to compare a biodegradable stent with a metallic stent. We observed that whereas the BMS cages the artery and prevents it from remodeling, the BRS allows the lumen diameter to change, reversing the initial increase in wall shear stress induced by neointimal hyperplasia and restoring a constant and homeostatic value of wall shear stress between the unstented and stented parts of the artery. Thus, in the case of stenting, the arterial remodeling in response to changes in wall shear stress as previously studied by other authors is enabled only by BRS.

The present study has several limitations that should be noted. First, it remains unknown if the results found here for miniswine would be the same in humans. Pigs have been shown to be an appropriate animal model to study angioplasty and stenting procedures[117]. Thus, it is reasonable to expect that the present results would be applicable to the human case. It should also be noted that the miniswine used were healthy animals and that the response of a diseased vessel to the deployment of a stent may differ from that of a healthy vessel. Future studies on diseased animals would help in this regard. Finally, both our analyses and computational simulations assumed the artery to be straight and rigid and considered blood as a purely Newtonian fluid. It would be interesting to study the sensitivity of the results to these assumptions.

The ability of an artery to adapt to the changes in its mechanical environment induced by the deployment of a stent is a critical consideration in determining the risk of post-stenting complications including restenosis, in-stent perturbations of the local flow field, and thrombosis. BRS appear to represent a major advance in this regard. BRS provide an effective scaffold for the artery during the first months after the procedure and their subsequent dismantling upon degradation allows the vessel to remodel and adapt its geometry to the

new biomechanical environment and thus to eventually restore physiological values of the applied stresses.

CHAPTER 5

Conclusions and Recommendations for Future Work

In the first chapter we introduced four questions that we intended to answer in the following chapters.

How does a stent degrade? How does the arterial wall thickness vary in reaction to a stenting procedure?

To answer these questions, we presented in chapter 2 the development of theoretical laws of behavior regarding:

1. the evolution of the stent mechanical properties with degradation: the degradation is primarily hydrolysis driven and is accelerated by the experienced stresses – a combination of the residual stresses due to the plastic deformation occurring during deployment and the stresses induced by the arterial wall pushing the stent inwards. The proposed equation for the evolution of the mechanical properties of the stent is based on experimental evidence for the contribution of hydrolysis, and on a simple modeling for the contribution of the load, in the absence of more detailed experimental data.
2. the evolution of arterial wall thickness in reaction to a stenting procedure: three contributions are taken into account; the proliferation of smooth muscle cells in the absence of endothelial cells, the proliferation of cells submitted to inflammation processes, and the thickening of the wall aiming to restore homeostatic values of the experienced hoop stresses.

Thereafter, we implemented these laws in a computational model thanks to the finite element software COMSOL 5.1. In a first step, the stent undergoes a pressure-driven deployment that simulates the inflation of a balloon and allows modeling the dogboning and the foreshortening of the stent as observed *in vivo*. The final state of stresses and deformed geometries of both stent and artery are used as initial state for the second step of the modeling implementing the intricate degradation and remodeling, thanks to an implicit method which updates the values of the stent mechanical properties and the arterial wall thickness according to the computed and stored stresses of the previous time step.

As has been previously highlighted by other authors[35,55], the degradation of the stent accelerated by the load is heterogeneous. This allows one to predict the places where the stent is more prone to dismantle during the degradation process. As far as we know, until now the degradation of a polymeric stent has been modeled only under *in vivo* compatible load and not using a dynamic coupling between the stent and the artery. Besides, previous works have considered either a hydrolysis-driven degradation[49] or a load-driven degradation[54,55] but not the combination of the two. Thus, our model may add new insight into the accurate prediction of the stent dismantling and the late recoil of the stent due to degradation.

To our knowledge, our study is the first to consider the arterial response to stent degradation. For a given set of parameters, our model is able to predict the increase and subsequent decrease of the arterial wall thickness, which is qualitatively observed *in vivo*[30]. However, the model exhibits strong influence on the chosen parameters and on the weight given to the different contributions. The literature experiments from which values were extracted seem insufficient to accurately determine all the model parameters. The model would therefore benefit from tailored experiments.

Could OCT be an interesting technique to quantitatively follow stent degradation and would it be useful to determine some parameters for more accurate computational models?

As seen in chapter 2, theoretical and computational model are based upon sets of parameters that need to be determined. Regarding stent degradation, different methods to follow the degradation of a polymeric material can be considered. Optical coherence tomography is a method of growing interest especially since it can be used *in vivo*. Moreover, stents struts appearance has been shown to qualitatively vary with degradation[137]. We developed an automated method to detect stent struts on OCT images and quantitatively follow their gray scale intensity during several months of degradation. We showed that the GSI can be described using the same type of exponential behavior than the one which describes others properties of the polymer such as the number average molecular weight[49]. Fitting the experimental data with a shape of this kind we determined the rate of hydrolysis of ART stents, with very good agreement with the ones determined from chemical analysis. As a result, the evolution of the GSI with time appears to represent a useful surrogate for stent degradation process, allowing one to determine the rate of degradation of a given stent; but adding two breaking through advantages compared to conventional techniques:

- it is a non destructive technique for *in vitro* experiments;
- it can be used *in vivo* in patients.

Therefore, OCT has the potential to be a versatile technique to study stent degradation.

Is an artery still able to adapt its lumen diameter to modified shear stress even if stented?

A well known phenomenon occurring the weeks following the stenting procedure is neointimal hyperplasia. To study this phenomenon, we modeled the evolution of arterial wall thickness in response to various factors, especially the perturbation of its mechanical

homeostasis regarding the experienced hoop stress. However, the flow field is also modified after the stenting procedure, and arteries are known to adapt their lumen diameter to a modification of the experienced shear stress[102,123]. To understand if a stented vessel is still able to remodel in response to modified blood flow field even if caged by a stent, we studied the evolution of the lumen diameter measured on OCT images and the evolution of the corresponding shear stress, estimated from the value of the lumen diameter thanks to Poiseuille modeling after having shown thanks to numerical simulations that the conclusions drawn based on Poiseuille flow remain valid even in the case of pulsatile flow because the dependence of wall shear stress is similar in both cases. We observed that whereas the bare metal stent caged the artery and prevented it from remodeling, the bioresorbable stent allowed the lumen diameter to vary leading to a decrease in shear stress and restoring a similar value for shear stress between the unstented and stented parts of the artery.

5.1 Recommendations for future work

5.1.1 Stent and artery geometries and mechanical properties

In a first study, we chose to use one of the earliest stent design, called the Palmaz Schatz design. The ART first stent design was very similar to this stent. However, open cell designs rather than closed cell designs have become more heavily used in recent years. Thus, our computational model can be adapted to these new geometries and more generally, it can be used to understand the importance of various aspects of stent design on the heterogeneous degradation and on the arterial remodeling. A three-layer model could be considered for the arterial wall, with a separate plaque.

Regarding mechanical properties, even if a simple law such as the neo-Hookean formulation appear to be a reasonable choice for a first approach, more complex laws such as the Knowles model[53] or the Mooney Rivlin law[49] could be implemented in further studies to describe more accurately the non- linear elastic behavior of polylactic acid. Furthermore, the viscoelasticity of PLA has been demonstrated and could also be taken into account[118,119]. For the artery, an anisotropic model similar to the one developed by Holzapfel[11] could be implemented to study the influence of the orientation of collagen fibers.

5.1.2 Degradation and arterial remodeling

Initially, stent degradation is associated with a decay in the stent's mechanical properties. The integrity of the stent is intact, but the stent gets progressively weaker. During this period, the artery is scaffolded, and this allows the healing of the wound due to the stent deployment and the compression of the plaque. The stent degradation and decreases in radial strength also allow progressive transfer of the stresses from the stent to the vessel. Because of the absence of endothelial cells, inflammation and stresses, the arterial wall thickens during this period. We focus on those phenomena in our computational model and

consider the wall thickening as occurring at the outside layer of the artery, as would happen in hypertension[103]. Modeling the embedment of the stent in the arterial wall, and thus considering the wall thickening to occur inside the wall and around the struts as well as outside would be an interesting addition expected to yield more accurate models.

It may also be possible to model the wall thickening as depending upon the local stress field and not on an average value of the stress field, as done in this work. As a proof of concept of the feasibility of this approach, we consider a quarter of a 2D model of a 2 mm-diameter silicone tube with a 1 mm-thick wall containing a defect at the outer edge, inflate it at a constant pressure of 5 GPa, and then impose on the outer wall a variation of the wall thickness defined as proportional to the difference between the local von Mises stresses and a constant. We see in Figure 5.1 that this eventually leads to a filling of the defect and a homogenization of the stresses in this given example. As a result, one could consider a wall thickening varying locally. However, one would need a finer mesh for the arterial wall and thus could expect computational times to increase with such a model.

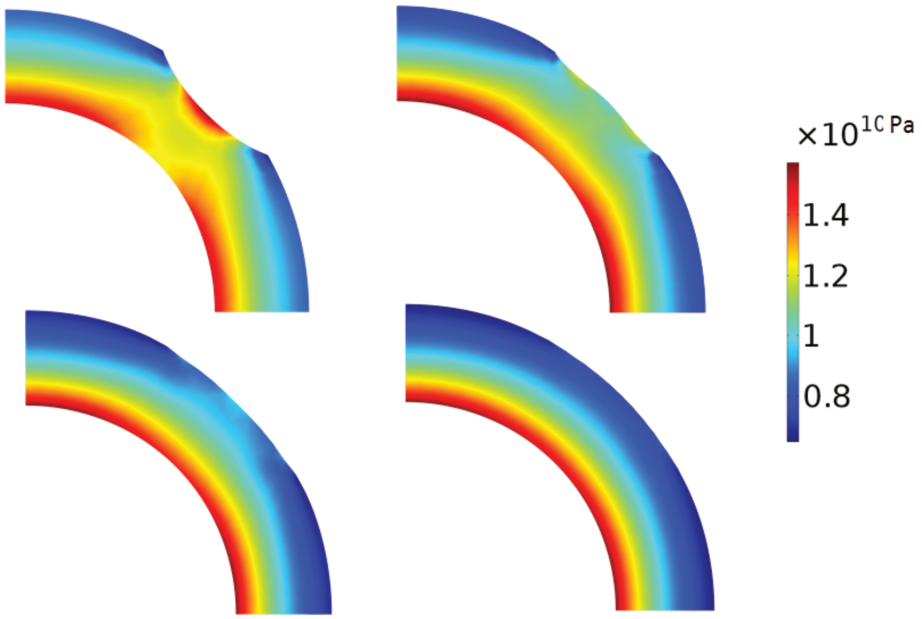

Figure 5.1: von Mises stresses in the quarter of a silicone tube with a defect at the outer edge; with a varying wall thickness proportionally to the difference between the experienced local stresses and a constant stress

In a second step, the stent dismantles, meaning that the struts break at the weakest zones. From that point, the pieces of the stent remaining embedded in the arterial wall will prevent the wall from collapsing, but will also allow potential positive remodeling[30,31]. As observed in chapter 4, whereas a bare metal stent cages the artery and prevents it from remodeling, BRS stented arteries exhibit late lumen gain, until removing the compliance mismatch in diameters between the stented and the unstented parts of the vessel. This also leads to a decrease in the estimated shear stress experienced by the artery until reaching a seemingly homeostatic value. Thereafter, the dismantling of the stent will be a crucial phenomenon that

needs to be taken into account in further studies, as well as the associated arterial remodeling. The evolution of the radius *R(t)* of the arterial lumen before the dismantling could be described as:

$$R(t) = R_0 - [w_{int}(t) - w_0] \quad (5.1)$$

where $w_{int}(t)$ *is* the wall thickness occurring at the inside wall and R_0 and w_0 are the initial radius and wall thickness, respectively; and the evolution of the late lumen gain could be described with equations of the following form:

$$R(t) = R_0 - [w_{int}(t) - w_0] + r(t) \quad (5.2)$$

$$\frac{dR}{dt} = -\frac{dw_{int}}{dt} + \frac{dr}{dt} = -\frac{dw_{int}}{dt} + A_{dism}.(\tau_{wall}(t) - \tau_{wall_0}) \quad (5.3)$$

where *r(t) is* the evolution of the late lumen gain, A_{dism} a constant, $\tau_{wall}(t)$ and τ_{wall0} the shear stress and the homeostatic value of the shear stress, respectively.

5.1.3 Parameters of the stent degradation

As mentioned previously, we used a simple linear dependence upon load to model the contribution of the load to the degradation of the polymer. This was chosen in the absence of more detailed experimental data. To investigate this more precisely, one could consider experiments in which samples of PLA fibers would be left to degrade in a saline solution at 37°C and followed by OCT imaging and quantification of the GSI as detailed in chapter 3, with samples unloaded and samples loaded with different forces. As the method is non-destructive and thus does not necessitate an excessively large number of samples, one can think of testing many values for the load, more than the one or two values usually tested in the literature[50,52,53]. Thus, the function k_{load} defined in chapter 2 could be fully determined.
Besides, as proposed in chapter 3, further studies are needed to validate the OCT technique's ability to quantitatively track stent degradation *in vivo,* and especially to understand how the infiltration of proteins and cells affects the strut grayscale intensity values. If the technique is validated, it could then be used to compare the degradation kinetics of a given stent *in vivo* and *in vitro*, and investigate the influence of patients' characteristics such as diabetes, hypertension, curved lesions, etc. on the rate of degradation of the stent.

5.1.4 Parameters of the arterial remodeling

The model would benefit from more detailed experiments regarding the influence of the three contributions proposed here as the key factors for the development of neointimal hyperplasia, and the relative weights of those factors. Indeed, the results show strong dependence upon the values of the different parameters, and the literature experiments from which values were extracted seem insufficient to accurately determine them. It would for instance be interesting to conduct tailored experiments in a given animal model, with a given polymeric material, to make the three contributions vary one at a time.

Bibliography

1. World Health Organization. The top 10 causes of death. (2014). Available at: http://www.who.int/mediacentre/factsheets/fs310/en/. (Accessed: 1st June 2016)
2. Ross, R. Rous-Whipple Award Lecture. Atherosclerosis: a defense mechanism gone awry. *Am. J. Pathol.* **143,** 987–1002 (1993).
3. Hoehn, K. & Marieb, E. N. Human anatomy and physiology. (2010).
4. Barquera, S. *et al.* Global Overview of the Epidemiology of Atherosclerotic Cardiovascular Disease. *Arch. Med. Res.* **46,** 328–338 (2015).
5. World Health Organization. Health statistics and information systems. Available at: http://www.who.int/healthinfo/global_burden_disease/metrics_daly/en/. (Accessed: 1st June 2016)
6. Wong, N. D. Epidemiological studies of CHD and the evolution of preventive cardiology. *Nat. Rev. Cardiol.* **11,** 276–89 (2014).
7. Collège national des enseignants de cardiologie – Société française de. *Cardiologie*. (Elsevier - Masson, 2015).
8. Levenson, J. W., Ms, P. J. S. & Gaziano, J. M. Reducing the Global Burden of Cardiovascular Disease: The Role of Risk Factors. 1–3 (2007). doi:10.1111/j.1520
9. National Heart Lung and Blood Institute. What Is Atherosclerosis? (2016). Available at: http://www.nhlbi.nih.gov/health/health-topics/topics/atherosclerosis. (Accessed: 1st June 2016)
10. Falk, E., Shah, P. K. & Fuster, V. Coronary plaque disruption. *Circulation* **92,** 657–671 (1995).
11. Holzapfel, G. a, Gasser, T. C. & Ogden, R. W. A new constitutive framework for arterial wall mechanics and a comperative study of material models. *J. Elast.* **61,** 1–48 (2000).
12. Félétou, M. Multiple functions of the endothelial cells. (2011).
13. Libby, P., Ridker, P. M. & Hansson, G. K. Progress and challenges in translating the biology of atherosclerosis. *Nature* **473,** 317–25 (2011).

14. Yurdagul, A., Finney, A. C., Woolard, M. D. & Orr, A. W. The arterial microenvironment: the where and why of atherosclerosis. *Biochem. J.* **473,** 1281–1295 (2016).

15. The Editors of Encyclopædia Britannica. Atherosclerosis - pathology. Available at: https://global.britannica.com/science/atherosclerosis. (Accessed: 1st June 2016)

16. Hahn, C. & Schwartz, M. A. NIH Public Access. **10,** 53–62 (2009).

17. Serruys, P. W. *et al.* Incidence of restenosis after successful coronary angioplasty: a time-related phenomenon. A quantitative angiographic study in 342 consecutive patients at 1, 2, 3, and 4 months. *Circulation* **77,** 361–371 (1988).

18. Fischman, D. L. *et al.* A randomized comparison of coronary-stent placement and balloon angioplasty in the treatment of coronary artery disease. *N. Engl. J. Med.* **331,** 496–501 (1994).

19. Serruys, P. W. *et al.* A comparison of balloon-expandable-stent implantation with balloon angioplasty in patients with coronary artery disease. *N. Engl. J. Med.* **331,** 489–495 (1994).

20. Morice, M.-C. *et al.* A randomized comparison of a sirolimus-eluting stent with a standard stent for coronary revascularization. *N. Engl. J. Med.* **346,** 1773–1780 (2002).

21. Sousa, J. E. *et al.* Clinical Investigation and Reports Sustained Suppression of Neointimal Proliferation by Sirolimus-Eluting Stents One-Year Angiographic and Intravascular Ultrasound Follow-Up. *Circulation* **104,** 2007–2012 (2001).

22. Daemen, J. *et al.* Articles Early and late coronary stent thrombosis of sirolimus- eluting and paclitaxel-eluting stents in routine clinical practice: data from a large two-institutional cohort study. *Methods* 1–12 (2005).

23. Pfisterer, M. E. Editorial: Late stent thrombosis after drug-eluting stent implantation for acute myocardial infarction a new red flag is raised. *Circulation* **118,** 1117–1119 (2008).

24. Lagerqvist, B. *et al.* Long-term outcomes with drug-eluting stents versus bare-metal stents in Sweden. *N. Engl. J. Med.* **356,** 1009–1019 (2007).

25. Finn, A. V. *et al.* Pathological correlates of late drug-eluting stent thrombosis: Strut coverage as a marker of endothelialization. *Circulation* **115,** 2435–2441 (2007).

26. Joner, M. *et al.* Pathology of Drug-Eluting Stents in Humans Delayed Healing and Late Thrombotic Risk. **48,** (2006).

27. Seo, T., Schachter, L. G. & Barakat, A. I. Computational study of fluid mechanical disturbance induced by endovascular stents. *Ann. Biomed. Eng.* **33,** 444–456 (2005).

28. Gojova, A. & Barakat, A. I. Vascular endothelial wound closure under shear stress: role of membrane fluidity and flow-sensitive ion channels. *J. Appl. Physiol.* **98,** 2355–2362 (2005).

29. Onuma, Y. & Serruys, P. W. Bioresorbable scaffold: The advent of a new era in percutaneous coronary and peripheral revascularization? *Circulation* **123,** 779–797 (2011).

30. Durand, E. *et al.* Head-to-head comparison of a drug-free early programmed dismantling polylactic acid bioresorbable scaffold and a metallic stent in the porcine coronary artery six-month angiography and optical coherence tomographic follow-up study. *Circ. Cardiovasc. Interv.* **7,** 70–79 (2014).

31. Karanasos, A. *et al.* OCT assessment of the long-term vascular healing response 5 years after everolimus-eluting bioresorbable vascular scaffold. *J. Am. Coll. Cardiol.* **64,** 2343–2356 (2014).

32. Colombo, A. & Karvouni, E. Biodegradable stents 'fulfilling the mission and stepping away'. *Circulation* **102,** 371–373 (2000).

33. Tamai, H., Igaki, K., Kyo, E. & Kosuga, K. Initial and 6-Month Results of Biodegradable Poly- l -Lactic Acid Coronary Stents in Humans. (2000).

34. Nishio, S. *et al.* Long-term (>10 Years) clinical outcomes of first-in-human biodegradable poly-l-lactic acid coronary stents: Igaki-Tamai stents. *Circulation* **125,** 2343–2352 (2012).

35. Soares, J. S. & Moore Jr, J. E. Biomechanical challenges to polymeric biodegradable stents. *Ann. Biomed. Eng.* **44,** 560–579 (2016).

36. Serruys, P. W. *et al.* A bioabsorbable everolimus-eluting coronary stent system (ABSORB): 2-year outcomes and results from multiple imaging methods. *Lancet* **373,** 897–910 (2009).

37. Serruys, P. W. *et al.* Evaluation of the Second Generation of a Bioresorbable Everolimus Drug-Eluting Vascular Scaffold for Treatment of De Novo Coronary Artery Stenosis Six-Month Clinical and Imaging Outcomes. (2010). doi:10.1161/CIRCULATIONAHA.110.970772

38. Serruys, P. W. *et al.* Dynamics of vessel wall changes following the implantation of the absorb everolimus-eluting bioresorbable vascular scaffold: a multi-imaging modality study at 6, 12, 24 and 36 months. *EuroIntervention J. Eur. Collab. with Work. Gr. Interv. Cardiol. Eur. Soc. Cardiol.* **9,** 1271–1284 (2014).

39. Bourantas, C. V. *et al.* Bioresorbable scaffolds: Current evidence and ongoing clinical trials. *Curr. Cardiol. Rep.* **14,** 626–634 (2012).

40. Wiebe, J., Nef, H. M. & Hamm, C. W. Current status of bioresorbable scaffolds in the treatment of coronary artery disease. *J. Am. Coll. Cardiol.* **64,** 2541–2551 (2014).

41. Erbel, R. *et al.* Temporary scaffolding of coronary arteries with bioabsorbable magnesium stents: a prospective, non-randomised multicentre trial. *Lancet* **369,** 1869–1875 (2007).

42. Migliavacca, F. *et al.* A predictive study of the mechanical behaviour of coronary stents by computer modelling. *Med. Eng. Phys.* **27,** 13–18 (2005).

43. Carlier, G. *et al.* Realistic finite element-based stent design: The impact of balloon folding. **41,** 383–389 (2008).

44. Ju, F., Xia, Z. & Sasaki, K. On the finite element modelling of balloon-expandable stents. *J. Mech. Behav. Biomed. Mater.* **1,** 86–95 (2008).

45. Gervaso, F. *et al.* On the effects of different strategies in modelling balloon-expandable stenting by means of finite element method. *J. Biomech.* **41,** 1206–1212 (2008).

46. Bedoya, J., Meyer, C. a, Timmins, L. H., Moreno, M. R. & Moore, J. E. Effects of stent design parameters on normal artery wall mechanics. *J. Biomech. Eng.* **128,** 757–765 (2006).

47. Gu, L., Zhao, S., Muttyam, A. K. & Hammel, J. M. The relation between the arterial stress and restenosis rate after coronary stenting. *J. Med. Devices, Trans. ASME* **4,** (2010).

48. Timmins, L. H., Meyer, C. a, Moreno, M. R. & Moore, J. E. Effects of stent design and atherosclerotic plaque composition on arterial wall biomechanics. *J. Endovasc. Ther.* **15,** 643–654 (2008).

49. Vieira, A. C. *et al.* Mechanical study of PLA-PCL fibers during in vitro degradation. *J. Mech. Behav. Biomed. Mater.* **4,** 451–460 (2011).

50. Miller, N. D. & Williams, D. F. The in vivo and in vitro degradation of poly (glycolic acid) suture material as a function of applied strain. *Biomaterials* **5,** 365–368 (1984).

51. Zhong, S. P., Doherty, P. J. & Williams, D. F. The Effect of Applied Strain on the Degradation of Absorbable Suture. **14,** (1993).

52. Fan, Y., Li, P. & Yuan, X. Influence of mechanical loads on degradation of scaffolds. *IFMBE Proc.* **31 IFMBE,** 549–552 (2010).

53. Hayman, D., Bergerson, C., Miller, S., Moreno, M. & Moore, J. E. The effect of static and dynamic loading on degradation of PLLA stent fibers. *J. Biomech. Eng.* **136,** 081006 (2014).

54. Soares, J. S., Moore, J. E. J. & Rajagopal, K. R. Constitutive Framework for Biodegradable Polymers with Applications to Biodegradable Stents. *ASAIO J.* **54,** 295–301 (2008).

55. Soares, J. S., Moore, J. E. & Rajagopal, K. R. Modeling of deformation-accelerated breakdown of polylactic acid biodegradable stents. *J. Med. Device.* **4,** 41007 (2010).

56. Debusschere, N., Segers, P., Dubruel, P., Verhegghe, B. & De Beule, M. A Computational Framework to Model Degradation of Biocorrodible Metal Stents Using an Implicit Finite Element Solver. *Ann. Biomed. Eng.* **44,** 382–390 (2016).

57. Garg, S. & Serruys, P. W. Coronary stents: Current status. *J. Am. Coll. Cardiol.* **56,** S1–S42 (2010).

58. Simsek, C., Daemen, J. & Zijlstra, F. [Developments in percutaneous coronary intervention and coronary stents]. *Ned. Tijdschr. Tandheelkd.* **121,** 375–379 (2013).

59. Garg, S. & Serruys, P. W. Coronary stents: Looking forward. *J. Am. Coll. Cardiol.* **56,** S43–S78 (2010).

60. Rolland, P. H. *et al.* Compliance matching stent placement in the carotid artery of the swine promotes optimal blood flow and attenuates restenosis. *Eur. J. Vasc. Endovasc. Surg.* **28,** 431–438 (2004).

61. Onuma, Y. *et al.* Intracoronary optical coherence tomography and histology at 1 month and 2, 3, and 4 years after implantation of everolimus-eluting bioresorbable vascular scaffolds in a porcine coronary artery model an attempt to decipher the human optical coherence tomog. *Circulation* **122,** 2288–2300 (2010).

62. Ormiston, J. A. *et al.* First serial assessment at 6 months and 2 years of the second generation of ABSORB everolimus-eluting bioresorbable vascular scaffold a multi-imaging modality study. *Circ. Cardiovasc. Interv.* **5,** 620–632 (2012).

63. Wan, Y. *et al.* Influence of external stress on the in vitro degradation behavior of C 3D/PLA composites. *J. Mater. Sci. Lett.* **20,** 1957–1959 (2001).

64. Gilding, D. K. & Reed, A. M. Biodegradable Polymers for Use in Surgery - Polyglycolic-Poly(Actic Acid) Homopolymers and Copolymers .1. *Polymer (Guildf).* **20,** 1459–1464 (1979).

65. Lou, C. & Chen, Y. Manufacturing and Properties of PLA Absorbable Surgical Suture Abstract. **78,** 958–965 (2008).

66. Middleton, J. C. & Tipton, A. J. Synthetic biodegradable polymers as orthopedic devices. **21,** (2000).

67. Athanasiou, K. A., Agrawal, C. M., Barber, F. A. & Burkhart, S. S. Orthopaedic applications for PLA-PGA biodegradable polymers. *Arthroscopy* **14,** 726–737 (1998).

68. Smit, T. H. *et al.* Sterilization and strength of 70/30 polylactide cages: e-beam versus ethylene oxide. *Spine (Phila. Pa. 1976).* **32,** 742–747 (2007).

69. Smit, T. H., Engels, T. A. P., Wuisman, P. I. J. M. & Govaert, L. E. Time-dependent mechanical strength of 70/30 Poly (L, DL-lactide): shedding light on the premature failure of degradable spinal cages. *Spine (Phila. Pa. 1976).* **33,** 14–18 (2008).

70. Durand, E. *et al.* Adjusting a polymer formulation for an optimal bioresorbable stent: A 6-month follow-up study. *EuroIntervention* **8,** 242–249 (2012).

71. Tamada, J. a & Langer, R. Erosion kinetics of hydrolytically degradable polymers. *Proc. Natl. Acad. Sci. U. S. A.* **90,** 552–556 (1993).

72. von Burkersroda, F., Schedl, L. & Göpferich, A. Why degradable polymers undergo surface erosion or bulk erosion. *Biomaterials* **23,** 4221–4231 (2002).

73. Grizzi, I., Garreau, H., Li, S. & Vert, M. Hydrolytic degradation of devices based on poly(DL-lactic acid) size dependence. *Biomaterials* **16,** 305–311 (1995).

74. Farrar, D. F. & Gillson, R. K. Hydrolytic degradation of polyglyconate B: The relationship between degradation time, strength and molecular weight. *Biomaterials* **23,** 3905–3912 (2002).

75. Martins, P. A. L. S., Jorge, R. M. N. & Ferreira, A. J. M. A Comparative Study of Several Material Models for Prediction of Hyperelastic Properties: Application to Silicone-Rubber and Soft Tissues. 135–147 (2006).

76. Mooney, M. A theory of large elastic deformation. *J. Appl. Phys.* **11,** 582–592 (1940).

77. Rivlin, R. S. Large elastic deformations of isotropic materials. IV. Further developments of the general theory. *Philos. Trans. R. Soc. London A Math. Phys. Eng. Sci.* **241,** 379–397 (1948).

78. Rajagopal, K. R., Srinivasa, A. R. & Wineman, A. S. On the shear and bending of a degrading polymer beam. *Int. J. Plast.* **23,** 1618–1636 (2007).

79. Deng, M. *et al.* Effect of load and temperature on in vitro degradation of poly(glycolide-co-L-lactide) multifilament braids. *Biomaterials* **26,** 4327–4336 (2005).

80. Porter, R. S. & Casale, A. Recent studies of polymer reactions caused by stress. *Polym. Eng. Sci.* **25,** 129–156 (1985).

81. Garlotta, D. A Literature Review of Poly (Lactic Acid). **9,** (2002).

82. Ellis, B. & Smith, R. *Polymers: a property database*. (CRC Press, 2008).

83. Chu, C. C. Hydrolytic degradation of polyglycolic acid: tensile strength and crystallinity study. *J. Appl. Polym. Sci.* **26,** 1727–1734 (1981).

84. Bauters, C. & Isner, J. M. The biology of restenosis. *Prog. Cardiovasc. Dis.* **40,** 107–116 (1997).

85. Chaabane, C., Otsuka, F. & Virmani, R. Biological responses in stented arteries. 353–363 (2013). doi:10.1093/cvr/cvt115

86. Asahara, T. *et al.* Local delivery of vascular endothelial growth factor accelerates reendothelialization and attenuates intimal hyperplasia in balloon-injured rat carotid artery. *Circulation* **91,** 2793–2801 (1995).

87. Sprague, E. A., Tio, F., Ahmed, S. H., Granada, J. F. & Bailey, S. R. Endothelial Cell Migration , Proliferation , and Function Coronary Swine Model. 499–508 (2016). doi:10.1161/CIRCINTERVENTIONS.111.967901

88. Itoh, Y., Toriumi, H., Yamada, S., Hoshino, H. & Suzuki, N. Resident endothelial cells surrounding damaged arterial endothelium reendothelialize the lesion. *Arterioscler. Thromb. Vasc. Biol.* **30,** 1725–1732 (2010).

89. Raff, M., Alberts, B., Lewis, J., Johnson, A. & Roberts, K. Molecular Biology of the Cell 4th edition. (2002).

90. Hobson, B. & Denekamp, J. Endothelial proliferation in tumours and normal tissues: continuous labelling studies. *Br. J. Cancer* **49,** 405 (1984).

91. Sho, E. *et al.* High flow drives vascular endothelial cell proliferation during flow-induced arterial remodeling associated with the expression of vascular endothelial growth factor. *Exp. Mol. Pathol.* **75,** 1–11 (2003).

92. Geemen, D. Van *et al.* F-Actin – Anchored Focal Adhesions Distinguish Endothelial Phenotypes of Human Arteries and Veins. (2014). doi:10.1161/ATVBAHA.114.304180

93. Rogers, C., Tseng, D. Y., Squire, J. C. & Edelman, E. R. Balloon-Artery Interactions During Stent Placement A Finite Element Analysis Approach to Pressure, Compliance, and Stent Design as Contributors to Vascular Injury. *Circ. Res.* **84,** 378–383 (1999).

94. Grewe, P. H., Deneke, T. & Machraoui, A. Acute and Chronic Tissue Response to Coronary Stent Implantation: Pathologic Findings in Human Specimen. **35,** (2000).

95. Tahir, H. *et al.* Endothelial repair process and its relevance to longitudinal neointimal tissue patterns: comparing histology with in silico modelling. (2014).

96. Harnek, J., Zoucas, E., Carlemalm, E. & Cwikiel, W. Differences in endothelial injury after balloon angioplasty, insertion of balloon-expanded stents or release of self-expanding stents: an electron microscopic experimental study. *Cardiovasc. Intervent. Radiol.* **22,** 56–61 (1999).

97. Van Der Giessen, W. J. *et al.* Marked inflammatory sequelae to implantation of biodegradable and nonbiodegradable polymers in porcine coronary arteries. *Circulation* **94,** 1690–1697 (1996).

98. Kornowski, R. A. N. *et al.* In-Stent Restenosis: Contributions of Inflammatory Responses and Arterial Injury to Neointimal Hyperplasia. **31,** 224–230 (1998).

99. Yahagi, K. *et al.* Comparison of a drug-free early programmed dismantling PDLLA bioresorbable scaffold and a metallic stent in a porcine coronary artery model at 3 years follow-up. *submitted*

100. Fajadet, J. ARTDIVA differentiating features and clinical update. (TCT2014) (2014).

101. Rogers, C., Welt, F. G. P., Karnovsky, M. J. & Edelman, E. R. Monocyte recruitment and neointimal hyperplasia in rabbits Coupled inhibitory effects of heparin. *Arterioscler. Thromb. Vasc. Biol.* **16,** 1312–1318 (1996).

102. Humphrey, J. D. Vascular adaptation and mechanical homeostasis at tissue, cellular, and sub-cellular levels. *Cell Biochem. Biophys.* **50,** 53–78 (2008).

103. Matsumoto, T. & Hayashi, K. Mechanical and dimensional adaptation of rat aorta to hypertension. *J Biomech Eng* **116,** 278–283 (1994).

104. Timmins, L. H., Miller, M. W., Jr, F. J. C. & Jr, J. E. M. Increased artery wall stress post-stenting leads to greater intimal thickening. *Lab. Investig.* **91,** 955–967 (2011).

105. GU, L., ZHAO, S. & FROEMMING, S. R. Arterial Wall Mechanics and Clinical Implications After Coronary Stenting: Comparisons of Three Stent Designs. *Int. J. Appl. Mech.* **04,** 1250013 (2012).

106. Kim, D. W., Langille, B. L., Wong, M. K. K. & Gotlieb, A. I. Patterns of Endothelial Microfilament Distribution in the Rabbit Aorta In Situ. (1988).

107. Menendez-Castro, C. *et al.* Intrauterine growth restriction promotes vascular remodelling following carotid artery ligation in rats. *Clin. Sci. (Lond).* **123,** 437–44 (2012).

108. Wang, M. *et al.* Angiotensin II activates matrix metalloproteinase type II and mimics age-associated carotid arterial remodeling in young rats. *Am. J. Pathol.* **167,** 1429–1442 (2005).

109. MatWeb - Material Property Data. Overview of materials for Polylactic Acid (PLA) Biopolymer . Available at: http://www.matweb.com/search/DataSheet.aspx?MatGUID=ab96a4c0655c4018a8785ac4031b9278&ckck=1. (Accessed: 1st June 2016)

110. Södergård, A. & Stolt, M. Properties of lactic acid based polymers and their correlation with composition. *Prog. Polym. Sci.* **27,** 1123–1163 (2002).

111. Veronda, D. R. & Westmann, R. A. Mechanical characterization of skin—finite deformations. *J. Biomech.* **3,** 111IN9123–122124 (1970).

112. Dobre, A. A., Morega, A. M. & Morega, M. The investigation of flow - Structural interaction in an arterial branching by numerical simulation. *Proc. IEEE/EMBS Reg. 8 Int. Conf. Inf. Technol. Appl. Biomed. ITAB* (2010). doi:10.1109/ITAB.2010.5687648

113. Badel, P., Avril, S., Sutton, M. A. & Lessner, S. M. Numerical simulation of arterial dissection during balloon angioplasty of atherosclerotic coronary arteries. *J. Biomech.* **47,** 878–889 (2014).

114. COMSOL Multiphysics 5.1. Plastic Deformation During the Expansion of a Biomedical Stent. Available at: https://www.comsol.fr/model/download/330841/models.nsm.biomedical_stent.pdf. (Accessed: 1st June 2016)

115. Bergström, J. S. & Hayman, D. An Overview of Mechanical Properties and Material Modeling of Polylactide (PLA) for Medical Applications. *Ann. Biomed. Eng.* **44,** 330–340 (2016).

116. Soares, J. S., Rajagopal, K. R. & Moore Jr, J. E. Deformation-induced hydrolysis of a degradable polymeric cylindrical annulus. *Biomech. Model. Mechanobiol.* **9,** 177–186 (2010).

117. Schwartz, R. S. *et al.* Restenosis after balloon angioplasty. A practical proliferative model in porcine coronary arteries. *Circulation* **82,** 2190–2200 (1990).

118. Soares, J. S. Constitutive modeling for biodegradable polymers for application in endovascular stents. (Texas A&M University, 2008).

119. Söntjens, S. H. M., Engels, T. A. P., Smit, T. H. & Govaert, L. E. Time-dependent failure of amorphous poly-D, L-lactide: Influence of molecular weight. *J. Mech. Behav. Biomed. Mater.* **13,** 69–77 (2012).

120. Vieira, A. C., Guedes, R. M. & Tita, V. Constitutive modeling of biodegradable polymers: Hydrolytic degradation and time-dependent behavior. *Int. J. Solids Struct.* **51,** 1164–1174 (2014).

121. Debusschere, N., Segers, P., Dubruel, P., Verhegghe, B. & Beule, M. De. A finite element strategy to investigate the free expansion behaviour of a biodegradable polymeric stent. *J. Biomech.* **48,** 2012–2018 (2015).

122. Eswaran, S. K., Kelley, J. A., Bergstrom, J. S. & Virginia, L. Material Modeling of Polylactide. 1–11 (2011).

123. Langille, B. L., Bendeck, M. P. & Keeley, F. W. Adaptations of carotid arteries of young and mature rabbits to reduced carotid blood flow. *Am. J. Physiol.* **256,** H931–H939 (1989).

124. Karst, D. & Yang, Y. Molecular modeling study of the resistance of PLA to hydrolysis based on the blending of PLLA and PDLA. *Polymer (Guildf).* **47,** 4845–4850 (2006).

125. Mainil-Varlet, P., Curtis, R. & Gogolewski, S. Effect of in vivo and in vitro degradation on molecular and mechanical properties of various low-molecular-weight polylactides. *J. Biomed. Mater. Res.* **36,** 360–380 (1997).

126. Vieira, A. C., Vieira, J. C., Guedes, R. M. & Marques, A. T. Experimental Degradation Characterization of PLA-PCL; PGA-PCL; PDO; and PGA Fibres. in *Materials Science Forum* **636,** 825–832 (2010).

127. Zilberman, M., Nelson, K. D. & Eberhart, R. C. Mechanical properties and in vitro degradation of bioresorbable fibers and expandable fiber-based stents. *J. Biomed. Mater. Res. - Part B Appl. Biomater.* **74,** 792–799 (2005).

128. Garcia-Garcia, H. M. *et al.* Assessing bioresorbable coronary devices Methods and parameters. *JACC Cardiovasc. Imaging* **7,** 1130–1148 (2014).

129. Prati, F. *et al.* Expert review document on methodology, terminology, and clinical applications of optical coherence tomography: Physical principles, methodology of image acquisition, and clinical application for assessment of coronary arteries and atherosclerosis. *Eur. Heart J.* **31,** 401–415 (2010).

130. Lee, S.-Y. & Hong, M.-K. Stent evaluation with optical coherence tomography. *Yonsei Med. J.* **54,** 1075–83 (2013).

131. Katoh, H. *et al.* Delayed Neointimalization on Sirolimus-Eluting Stents. *Circ. J.* **73,** 1033–1037 (2009).

132. Won, H. *et al.* Optical coherence tomography derived cut-off value of uncovered stent struts to predict adverse clinical outcomes after drug-eluting stent implantation. *Int. J. Cardiovasc. Imaging* **29,** 1255–1263 (2013).

133. Capodanno, D. *et al.* Comparison of optical coherence tomography and intravascular ultrasound for the assessment of in-stent tissue coverage after stent implantation. *EuroIntervention J. Eur. Collab. with Work. Gr. Interv. Cardiol. Eur. Soc. Cardiol.* **5,** 538–543 (2009).

134. Suzuki, Y. *et al.* In Vivo Comparison Between Optical Coherence Tomography and Intravascular Ultrasound for Detecting Small Degrees of In-Stent Neointima After Stent Implantation. *JACC Cardiovasc. Interv.* **1,** 168–173 (2008).

135. Kwon, S. W. *et al.* Qualitative assessment of neointimal tissue after drug-eluting stent implantation: comparison between follow-up optical coherence tomography and intravascular ultrasound. *Am. Heart J.* **161,** 367–372 (2011).

136. Yonetsu, T. *et al.* Comparison of incidence and time course of neoatherosclerosis between bare metal stents and drug-eluting stents using optical coherence tomography. *Am. J. Cardiol.* **110,** 933–939 (2012).

137. Ormiston, J. A. *et al.* A bioabsorbable everolimus-eluting coronary stent system for patients with single de-novo coronary artery lesions (ABSORB): a prospective open-label trial. *Lancet* **371,** 899–907 (2008).

138. Caselles, V., Kimmel, R. O. N., Sapiro, G. & Kimmel, R. O. N. Geodesic Active Contours. *Int. J. Comput. Vis.* **22,** 61–79 (1997).

139. Rudin, L. I., Osher, S. & Fatemi, E. Nonlinear total variation based noise removal algorithms. *Phys. D Nonlinear Phenom.* **60,** 259–268 (1992).

140. WOLINSKY, H. Long-Term Effects of Hypertension on the Rat Aortic Wall and Their Relation to Concurrent Aging Changes: MORPHOLOGICAL AND CHEMICAL STUDIES. *Circ. Res.* **30,** 301–309 (1972).

141. Chien, S., Usami, S., Dellenback, R. J. & Gregersen, M. I. Blood viscosity: influence of erythrocyte deformation. *Science (80-.).* **157,** 827–829 (1967).

142. Asakura, T. & Karino, T. Flow patterns and spatial distribution of atherosclerotic lesions in human coronary arteries. *Circ. Res.* **66,** 1045–1066 (1990).

143. Yunus, A. C. & Cimbala, J. M. Fluid mechanics: fundamentals and applications. *Int. Ed. McGraw Hill Publ.* 185–201 (2006).

144. McDonald, D. A. Blood flow in arteries. (1974).

145. Thoma, R. Untersuchunung über die Histogenese und Histomechanik des Gefässystems. (1893).

146. Murray, C. D. The Physiological Principle of Minimum Work: I. The vascular system and the cost of blood volume. *Proc. Natl. Acad. Sci. U. S. A.* **12,** 207–214 (1926).

147. Zamir, M. Shear forces and blood vessel radii in the cardiovascular system. *J. Gen. Physiol.* **69,** 449–61 (1977).

ANNEX: French summary of the thesis work

Modélisation des stents biodégradables et de leur impact sur la paroi artérielle

L'athérosclérose est une pathologie caractérisée par l'accumulation de lipides, de calcifications, de fibrose et de cellules entre la couche interne de l'artère ou intima, et la couche médiane ou media. Dans les stades avancés, la plaque ainsi formée rétrécit le calibre de l'artère et gène l'écoulement du flux sanguin. Les complications de cette maladie sont d'une part chroniques et alors liées à l'ischémie des cellules situées en aval de la sténose. Ainsi, selon la localisation de la plaque d'athérome, des douleurs à type d'angor d'effort – pour des plaques situées au niveau des artères coronaires – ou de claudication à la marche – pour des plaques situées au niveau des artères des membres inférieurs – peuvent être ressenties par le patient. D'autre part, des événements aigus peuvent survenir. En effet, la plaque peut se rompre, obstruer la lumière artérielle et entraîner la mort des cellules irriguées en quelques heures si le vaisseau n'est pas ré ouvert ; c'est ce phénomène qui est responsable des infarctus myocardiques et de certains accidents vasculaires cérébraux notamment. Ainsi, les complications de l'athérosclérose sont la première cause de décès dans le monde d'après l'Organisation Mondiale de la Santé.

Lorsque la sténose de l'artère est serrée et symptomatique, ou si le vaisseau doit être ré-ouvert en urgence, le traitement le plus couramment utilisé est la pose de stents, des structures métalliques en forme de ressorts que l'on peut insérer dans la circulation systémique via une artère périphérique à l'aide d'un cathéter, guider jusqu'à la portion sténosée ou bloquée de l'artère malade, et déployer – typiquement à l'aide du gonflement d'un ballon – afin de ré-ouvrir l'artère et de restaurer le flux sanguin. La première génération de stents, utilisée pour la première fois en 1986, était constituée de métal. Bien que très efficaces pour restaurer le flux sanguins, ces stents étaient associés à des taux importants de resténose – définie comme la récidive du rétrécissement du calibre artériel, qui pouvaient atteindre jusqu'à 30% des procédures. La resténose est due à une prolifération incontrôlée des cellules musculaires lisses de la media en réaction à la blessure causée à l'artère par le déploiement du stent. Pour éviter cela, les stents furent ensuite enduits d'une couche de médicaments anti-prolifératifs. Grâce à cette seconde génération de stents, les taux de resténose chutèrent en dessous de 3%. Cependant, non seulement la prolifération des cellules musculaires lisses est inhibée par ces médicaments, mais la ré-endothélialisation, c'est-à-dire la formation d'une nouvelle intima après sa destruction par le déploiement du stent, est également limitée. Cela conduit à la présence de struts non recouvertes par des cellules endothéliales ; et cela est probablement la cause du nombre accru de thromboses tardives – un évènement rare, mais souvent de très mauvais pronostic lorsqu'il survient – associé à cette seconde génération de stents.

Dans ce contexte, un concept intéressant est celui de stent biorésorbable (BRS). Ce concept est basé sur l'idée qu'un stent n'est nécessaire que jusqu'à la guérison de l'artère – suite à quoi il serait préférable que le stent disparaisse, afin de retrouver un état plus physiologique.

Les BRS sont des devices complexes dont le comportement est jusqu'à présent principalement étudié grâce à des essais expérimentaux longs, difficiles et coûteux. Le développement de modèles décrivant leur comportement à l'état initial mais également au cours de la dégradation pourrait faciliter et améliorer le développement de BRS performants, afin de calibrer leur dégradation pour qu'ils soutiennent l'artère juste le temps nécessaire et qu'après cela ils disparaissent.

Par ailleurs, le déploiement d'un stent altère significativement les contraintes mécaniques exercées sur la paroi artérielle, or celles-ci jouent un rôle important dans l'incidence de complications telle que la resténose et l'hyperplasie néointimale. Dans le cas d'un BRS, les contraintes mécaniques dans le stent comme dans la paroi artérielle évoluent au fur et à mesure que le stent se dégrade. De plus, la dégradation du stent par hydrolyse peut être accélérée par ces contraintes : un couplage supplémentaire qui doit être pris en compte. Dans cette étude, nous nous intéressons à la détermination de l'évolution des contraintes dans le stent et dans l'artère pendant le déploiement puis la dégradation du stent, ainsi qu'à l'influence de ces contraintes sur la dégradation du stent et sur le remodelage de la paroi. Le remodelage de la paroi est également influencé par la dénudation de l'endothélium et par l'inflammation induite par l'implantation d'un BRS. Dans ce but, nous avons développé un modèle 3D par éléments finis du déploiement et de la dégradation d'un BRS en acide polylactique tenant compte du couplage entre l'artère et le stent. Il permet notamment de prédire les zones les plus fragiles du stent et donc les points qui seront probablement les premiers à être démantelés, ainsi que l'évolution de l'épaisseur de la paroi artérielle en réponse à l'implantation d'un BRS.

Etant donné que le modèle repose fortement sur des paramètres qui doivent être déterminés expérimentalement, nous nous sommes également intéressés au développement d'une méthode expérimentale pour suivre la dégradation d'un BRS. Nous avons utilisé la tomographie par cohérence optique (OCT) pour suivre régulièrement la dégradation de stents déployés dans des tubes et immergés dans du sérum physiologique à 37°C pendant deux ans. Nous avons ensuite développé une méthode qui détecte automatiquement les struts des stents sur les images OCT et quantifie leur intensité de niveau de gris. Les résultats suggèrent que cette méthode automatisée d'analyse d'images OCT est un outil prometteur pour évaluer quantitativement l'état de dégradation d'un BRS.

Enfin, nous nous sommes intéressés à la capacité d'une artère stentée à s'adapter à une modification du cisaillement ressenti. Nous avons étudié l'évolution de la lumière artérielle de porc stentés suivis *in vivo* par OCT ainsi que le cisaillement associé. Alors qu'un stent métallique bloque le remodelage artériel, nous avons observé qu'un BRS – probablement grâce au démantèlement du stade final de la dégradation – libère le vaisseau et permet ainsi l'adaptation de son diamètre de manière à diminuer le cisaillement et l'inadéquation avec l'artère non stentée. L'adaptation de la lumière artérielle permise par le démantèlement du stent pourrait être prise en compte dans de futurs modèles numériques.

université PARIS-SACLAY | ÉCOLE DOCTORALE INTERFACES Approches Interdisciplinaires : Fondements, Applications et Innovation

Titre : Modélisation des stents biodégradables et leur impact sur la paroi artérielle

Mots clés : biomécanique, stent, biodégradable, artère

Résumé : Les stents sont aujourd'hui le traitement le plus courant des stades avancés de l'athérosclérose. Le concept de stents bioresorbables (BRS) est basé sur l'idée qu'un stent n'est nécessaire que jusqu'à la guérison de l'artère – suite à quoi il serait préférable que le stent disparaisse, afin de retrouver un état plus physiologique. Le déploiement d'un stent altère significativement les contraintes mécaniques exercées sur la paroi artérielle, or celles-ci jouent un rôle important dans l'incidence de complications telle que la resténose et l'hyperplasie néointimale. Dans le cas d'un BRS, les contraintes mécaniques dans le stent comme dans la paroi artérielle évoluent au fur et à mesure que le stent se dégrade. De plus, la dégradation du stent par hydrolyse peut être accélérée par ces contraintes : un couplage supplémentaire qui doit être pris en compte. Nous nous intéressons à la détermination de l'évolution des contraintes dans le stent et dans l'artère pendant le déploiement puis la dégradation du stent, ainsi qu'à l'influence de ces contraintes sur la dégradation du stent et sur le remodelage de la paroi, qui est également influencé par la dénudation de l'endothélium et par l'inflammation induite par l'implantation d'un BRS. Pour atteindre ces objectifs, nous avons développé un modèle 3D par éléments finis du déploiement et de la dégradation d'un BRS en acide polylactique tenant compte du couplage entre l'artère et le stent. Il permet notamment de prédire les zones de démantèlement du stent et l'évolution de l'épaisseur de la paroi artérielle en réponse à l'implantation d'un BRS. Etant donné que le modèle repose fortement sur des paramètres qui doivent être déterminés expérimentalement, nous nous sommes intéressés au développement d'une méthode expérimentale pour suivre la dégradation d'un BRS. Nous avons utilisé la tomographie par cohérence optique (OCT) pour suivre régulièrement la dégradation de stents déployés dans des tubes et immergés dans du sérum physiologique à 37°C pendant deux ans. Nous avons ensuite développé une méthode qui détecte automatiquement les struts des stents sur les images OCT et quantifie leur intensité de niveau de gris. Les résultats suggèrent que cette méthode automatisée d'analyse d'images OCT est un outil prometteur pour évaluer quantitativement l'état de dégradation d'un BRS. Enfin, nous nous sommes intéressés à la capacité d'une artère stentée à s'adapter à une modification du cisaillement ressenti. Nous avons étudié l'évolution de la lumière artérielle de porc stentés suivis *in vivo* par OCT ainsi que le cisaillement associé. Alors qu'un stent métallique bloque le remodelage artériel, nous avons observé qu'un BRS – probablement grâce au démantèlement du stade final de la dégradation – libère le vaisseau et permet ainsi l'adaptation de son diamètre de manière à diminuer le cisaillement et l'inadéquation avec l'artère non stentée. L'adaptation de la lumière artérielle permise par le démantèlement du stent pourrait être prise en compte dans de futurs modèles numériques.

Title: Modeling biodegradable stents and their effect on the arterial wall

Keywords: biomechanics, stent, biodegradable, artery

Abstract: Today, sent deployment is the most common treatment for symptomatic atherosclerosis. Bioresorbable stents (BRS) are based on the premise that a stent is needed only until arterial wound healing occurs after which it would be desirable for the stent to degrade so that the arterial wall recovers its natural compliance. Deployment of a stent profoundly alters the mechanical environment in the arterial wall, and these alterations play an important role in regulating the incidence of complications such as restenosis and neointimal hyperplasia. In the case of a BRS, the mechanical stresses in both the stent and the arterial wall evolve as the stent degrades. Furthermore, the hydrolysis-driven degradation of the stent can be accelerated by mechanical stresses in the stent, an additional coupling that needs to be taken into account. We are interested in determining the evolution of stresses in both the stent and the arterial wall during the stent deployment and degradation process and in elucidating the effect of these stresses on the stent degradation and on the remodeling process in the wall, which would also be influenced by the loss of endothelial cells and the amount of inflammation induced by the stent deployment and degradation. To this end, we have developed a 3D finite element model of the deployment and degradation of a polylactic acid (PLA) BRS that integrates the coupling between the stent and the artery. This allows one to predict the zones of dismantling of the stent and the evolution of the arterial thickness in response to a BRS stenting procedure. Since the model relies strongly on parameters that need to be determined experimentally, we became interested in developing methods to follow stent degradation. With this aim, we used optical coherence tomography (OCT) to image several BRS that were deployed into tubes and allowed to degrade in a saline solution at 37°C over a period of two years. We subsequently developed a versatile method for automatically detecting stent struts on the OCT images and quantifying the strut gray scale intensity. The results suggest that this automated method of OCT image analysis represents a promising tool to quantitatively assessing BRS degradation states. Lastly, we were interested in establishing the ability of a stented artery to adapt to a modification in its wall shear stress. Studying the *in vivo* evolution of the lumen of stented mini-swine arteries followed by OCT imaging allowed us to demonstrate that whereas a bare metal stent cages the artery, a BRS, presumably due to its degradation-induced dismantling, frees the vessel and enables it to adapt its lumen diameter in order to decrease its absolute level of shear stress and the compliance mismatch with the unstented portion of the artery. This lumen adaptation allowed by the stent dismantling could be taken into account in future computational models.